Optical springs to create macroscopic optical traps and negative inertia for gravitational wave detectors.

Jennifer L. Wright

Submitted in fulfilment of the requirements for the

Degree of Doctor of Philosophy

School of Physics and Astronomy

College of Science and Engineering

University of Glasgow

September 2022

Summary

This thesis investigates the phenomena of negative inertia and optical traps, and endeavours to implement them in an interferometer system that is a prototype of a gravitational wave detector arm cavity and uses similar control techniques and apparatus.

Chapter 1 discusses gravitational waves and how they are produced. It then moves onto the basic design of current gravitational wave detectors and the main noise sources that are required to be taken into account when engineering the detector. Lastly, it concludes by discussing future gravitational wave detector designs and how this work might inform these.

In Chapter 2 the theoretical underpinnings of optical springs are discussed. The chapter moves on to discuss the quantum noise of an interferometer and how optical springs change this. An expression for the optical spring constant is given, and then the thesis discusses how the frequency dependence of this quantity complicates obtaining analytical expressions. A review of optical spring stability in a Fabry-Perot interferometer is then provided. Systems with multiple optical springs that would be interesting to investigate in the current work are discussed, then a justification is given for investigating these effects and optical springs in general, in the light of the current state of the field.

The layout of the experimental apparatus is laid out in Chapter 3. There are two experimental cavities which share a common mirror, the central test mass (CTM), and two input lasers. The setup of the optical systems is discussed first, then the layout of the suspensions, then how the electronic control of the lasers and experimental cavities is achieved.

Chapter 4 lays out the procedure for calibrating the experiment and carrying it out. The determination of the cavity circulating power is discussed mathematically. Then the setup of the cavity simulation, the experimental calibration of the two cavity measurement process, and finally the calibration of spring detuning in the main experimental cavity is described.

Results of the main thesis experiments are discussed in Chapter 5. Measurements using simple optomechanical systems are discussed first, then more complex measurements are described. Finally, evidence for both negative inertia and trapping is discussed.

The conclusion given in Chapter 6 sums up the tasks achieved in the thesis work and the limitations of the results obtained are discussed. Some suggestions for further work are given.

Contents

List of Tables

List of Figures

Acknowledgements

I would like to extend my sincere thanks to my supervisors: Ken Strain, Stefan Hild and Jim Hough for all their help and support in my PhD and during my thesis writing. I would also like to thank Bryan Barr for teaching me all my lab skills and having an encyclopaedic knowledge of interferometry, the setup of everything in the lab, always being willing to explain anything simply, and for being a good office-mate and friend. Thanks also to Sabina Huttner for being a great office-mate and for all her advice over the years.

Thanks to everyone who proof-read my writing, including Alistair Grant, Sheila Rowan, Martin Sinclair, Andrew Spencer, Hunter Gabbard, David Wright and Mairi Wright.

Thanks as well go to all my colleagues in IGR for many valuable coffees, lunches and pub sessions, which got me through many a stressful week.

Thanks to all my family and friends, who enquired after my thesis and tactfully avoided the question 'when will you get a proper job?'. And finally, thanks to Mairi and David Wright who kept a roof over my head and have been supportive throughout my life.

Declaration

Chapter 1 and Chapter 2 contain the author's review of background material.

Chapter 3 contains details of the experimental apparatus, which was setup by Dr. Gordon, Dr. Barr and the author.

Chapter 4 lays out how the experiment is calibrated and the experiments carried out, and also details the simulation of the main results. All work is the author's; aside from data taking which was carried out with the assistance of Bryan Barr and the advice of Prof. Strain, and the simulation which was based on work by Dr. Gordon and modified with the assistance of Dr. Barr and Prof. Strain.

Results of the main thesis experiments in Chapter 5 and the conclusion in Chapter 6 are both the work of the author.

Appendices are the work of the author with guidance by Prof. Hough.

Chapter 1

Introduction

1.1 Gravitational Waves

In 2015 gravitational wave astronomy took a big leap forward as a field with the first discovery of a binary black hole system, the first direct gravitational wave detection. This was achieved with the two detector network of Advanced LIGO detectors in Livingston, Louisiana and Hanford, Washington. The discovery happened before either detector was at their final design sensitivity [8, 9]. Since then, many more detections and science results have been achieved by a network consisting of the the two LIGO detectors and the Advanced Virgo detector in Pisa, Italy [10–12], notably including the first gravitational wave with corresponding electromagnetic observations [13] from a binary neutron star merger.

Gravitational waves can be characterised mathematically using formulas originally derived by Einstein from his general field equations describing general relativity [14, 15]. The waves that we measure at the earth have to be produced by very massive objects in order to be observable and so come from astronomically distant massive objects. This allows us to assume the waves we detect are very distant from their source and allows us to make an approximation that the waves are small linear perturbations in the local gravitational field [16]. Einstein's equation relate the stress-energy tensor $T_{\mu\nu}$, which describes the distribution of energy and mass in a region of space-time with the Einstein tensor $G_{\mu\nu}$ which describes the curvature produced in the region

of space-time by the stress-energy [17]. The set of field equations denoting this is given in this review as

$$G_{\mu\nu} = \frac{8\pi G}{c^4} T_{\mu\nu} \tag{1.1}$$

where G is the gravitational constant and c is the speed of light.

This leads us to the wave equation for the changing gravitational field. This appears as a time dependent force which causes a warping of space-time, which can be thought of as a time-dependent relative length change along the coordinate directions at 90° to the direction the wave is travelling. The waves can therefore be measured by looking for the relative change in length per unit length of space-time locally as the waves pass through a region of space-time [16].

1.2 Sources of Gravitational Waves

Events which cause this warping of space-time are caused by large accelerations of masses in a gravitational field that give rise to non-zero quadrupole moments [17]. This gives the relation

$$Q_{jk} = \int \rho x_j x_k \, \mathrm{d}^3 x \tag{1.2}$$

where Q_{jk} is the second moment of inertia of the system, $\mathrm{d}^3 x$ is the three-dimensional spatial integral, ρ is the density of the mass, and $x_{j,k}$ is the distance in the j or k-th dimension within the mass distribution [18–20]. Since in the simplest case the amplitude of the gravitational waves produced depends on Q_{jk}, it means we can express the amplitude of the waves as the following tensor,

$$h_{jk} = \frac{2}{r} \frac{\mathrm{d}^2 Q_{jk}}{\mathrm{d}t^2} \tag{1.3}$$

where h_{jk} is the strain in along the j and k-th directions, r is the distance to the source, and $\frac{\mathrm{d}^2 Q_{jk}}{\mathrm{d}t^2}$ is the double derivative of the second moment of inertia [16].

As can be seen from equation (1.3), the amplitude of the gravitational wave depends on the double derivative of the quadrupole moment meaning the mass distribution must not be sym-

metrical and must be accelerating to produce a wave [16, 21]. Sources of gravitational waves include non-spherically symmetric orbital systems like two compact objects orbiting in a binary. The frequency of the gravitational waves is affected by the relative and combined mass of the two objects [16].

Gravitational waves are weak compared to the strength of a system's constant gravitational field, but the tidal force caused by the waves is proportional to $d^{-1}\lambda^{-2}$, where d is the source distance and λ is the gravitational wave wavelength; as opposed to the tidal force from the constant gravitational field which is proportional to d^{-3}. This gives a requirement that gravitational waves be measured at a greater distance from their source than the magnitude of their wavelength, $d >> \lambda$. Also, detectors are not very sensitive to gravitational waves so those that are detectable must involve very large changes in mass distribution. This means good gravitational wave sources are those of high mass and high acceleration; astrophysical sources of a large mass density like neutron stars, black holes, or events in the early universe [16]. The inspiral of these objects when they exist in close binaries, gives rise to gravitational wave signals which increase in frequency until the point of coalescence, these are therefore known as 'chirps' of gravitational waves. They are detectable in the middle of the Advanced LIGO and Advanced Virgo detector frequency bands, which stretch from 10 Hz to 10 kHz [16, 21].

1.2.1 Sensing Gravitational Waves

As gravitational waves can be detected by the strain they produce in space-time, it is possible to observe the effect on the two coordinate directions in space-time and see the stretching the wave causes in their comparative lengths over time as it travels through in the orthogonal direction. The equation which governs the relationship between strain h, length in space-time L, and change in this length ΔL,

$$h = \frac{2\Delta L}{L} \tag{1.4}$$

is provided in [21]. To see a relative change in coordinate distance, a way is needed of monitoring two directions in space-time. Since it is necessary to use distances on the order of the

gravitational wavelength and assuming the waves travel at the same speed as light, a method is needed that gives a detector baseline on the order of 7500 km for a lower detection threshold of 10 Hz [22].

1.3 Gravitational Wave Detectors

1.3.1 Introduction to Interferometric Measurement

A gravitational wave detector consists of an advanced version of the measurement device first used by Michelson and Morley in their 1887 experiment [23]. The basic design is shown in Figure 1.1 and consists of two paths (or 'arms') at 90 °. A laser travels down one of these and hits a 50:50 beam-splitter at 45 ° to the incoming beam cross-section. Half the light is transmitted through the beam-splitter down one arm and half is reflected perpendicular to the axis of the incoming beam from the laser and so travels down the perpendicular arm. Both beams then hit highly reflective mirrors normal to the beam cross-section. They reflect off these mirrors then recombine at the beam-splitter and are directed in the other direction perpendicular to the incoming beam from the laser in the last port of the beam-splitter. The two beams beat together on a detector placed in this port and the detector, usually a photo-diode, produces a voltage proportional to the power on this photo-diode. The relative phase of each field when they recombine is dependent on how much relative distance each has travelled. If both beams have travelled the same distance or the difference in travel distance is an integer of the laser wavelength, they will both reach the beam-splitter with a relative phase of 0. On the other hand if the relative change between the two fields is 180 °, the relative length difference between the arms will be an odd number of half-wavelengths of the laser frequency. With the first case the power output at the detector is maximised due to constructive interference between the two fields and with the second case the detector output is minimised due to destructive interference. In a real detector, the detector is kept near, not on, the destructive interference point allowing only a small amount of light to reach the detector [21, 22, 24]. The light in the main interferometer laser mode that reaches the output is used as a reference to measure the phase change of the signal caused by the stretching and squeezing of the interferometer arms by gravitational waves [21, 22, 24]. This system is known

as DC readout [21, 24] .

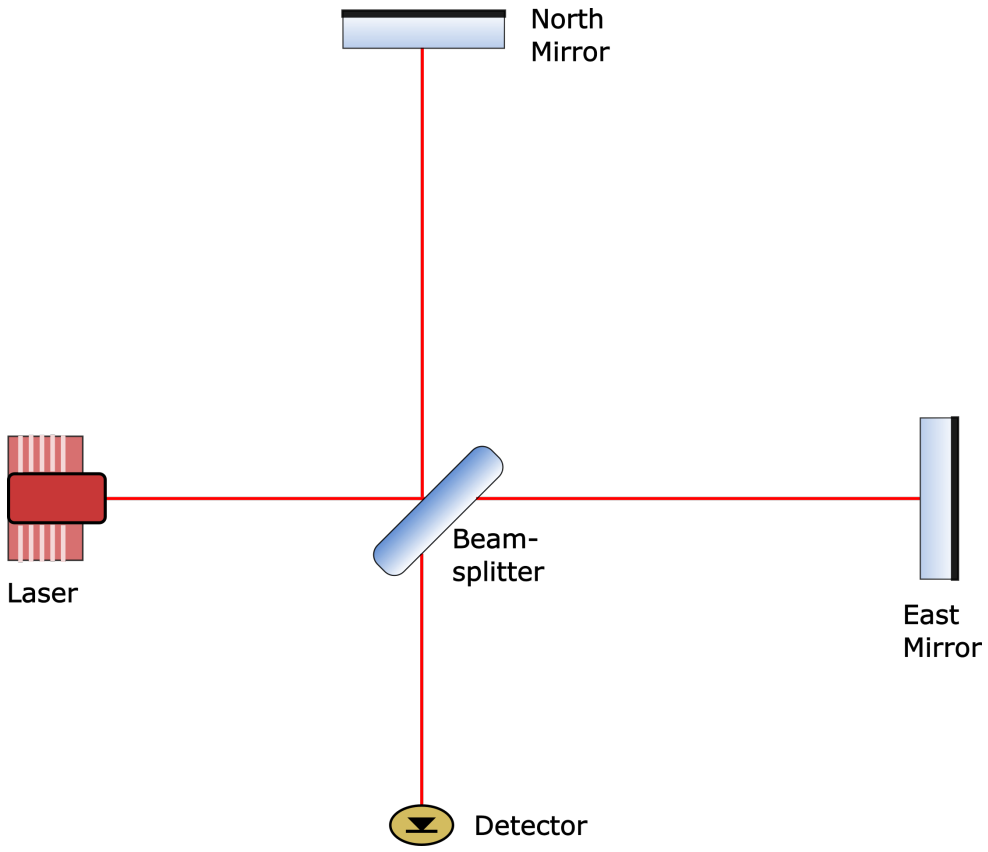

Figure 1.1: Simple Michelson Interferometer of the general design used by Michelson and Morley except with a modern monochromatic laser as a light source.

1.3.2 Sensing in Gravitational Wave Detectors

As was mentioned in Section 1.2.1, long detector arm-lengths are required in order to observe down to the lower bound of the current detectors' frequency range. However building interferometric detectors on the order of thousands of km is expensive and involves additional technical challenges [25]. Thus, other techniques have been used to increase the real length of the detector as seen by the gravitational wave signal, from the current Advanced LIGO detector length, which is 4 km [9].

Arm Cavities If the light travel time in the interferometer is increased, a greater phase shift is imposed on the light by the gravitational wave passing, and this has the same effect as increasing the arm length. This is achieved by creating a resonant system called a 'Fabry-Perot' cavity in

both arms of the detector, see Figure 1.2 for a simple diagram of a Fabry-Perot cavity [21, 26]. The input field to the arm cavity a_0 is partially reflected from the first cavity mirror, and the majority of the power is transmitted into the cavity and proceeds to bounce between the two mirrors. The total circulating field is a_c, which builds up on each round trip of the cavity as the circulating field is added to by further transmission through the mirror M1, up to a maximum which depends on the transmissivity of both mirrors. The degree to which the power falls off as the incoming light field frequency moves away from the fundamental mode is characterised by the bandwidth of the cavity γ. This is the frequency distance between the centre of the cavity fundamental mode and the frequency of a_0 at which the power circulating in the cavity drops to half of its maximum power. a_r is the sum of the field reflected from the cavity and the small proportion of light which leaks back through M1 on each round trip. a_t is the sum of all the fields lost through transmission through the second mirror, M2, in each round trip of the cavity. To implement this setup in the detector, a highly reflective mirror is placed right after the beam splitter in each arm of the Michelson interferometer, with the highly reflective side facing the end mirrors. If the arm lengths are kept to a length that is an integer number of half-wavelengths of the main laser, then power builds up to a steady state in both 'arm cavities'. The signal caused by the gravitational wave is increased in amplitude by the number of round trips it undergoes in the arm cavity so using arm cavities is equivalent to increasing the detector arm length [26]. This also allows for a much greater power to be used in the main sensing part of the interferometer than the laser can provide and this has implications for noise induced by the light field itself, discussed in a later section [21, 22, 26].

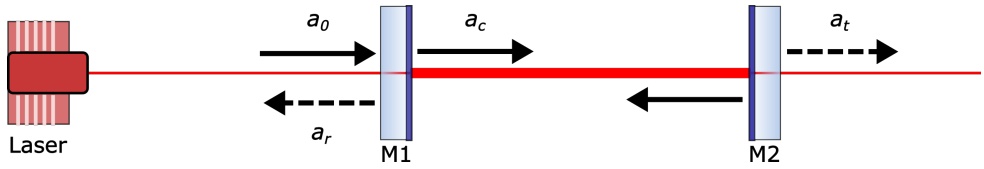

Figure 1.2: Simple resonant cavity of the general design used as an arm cavity in Advanced LIGO to increase the phase change caused by a gravitational wave, where M1 is the input mirror and M2 is the end mirror, a_0 is the input field, a_r is the reflected field from the cavity, a_c is the circulating cavity field and a_t is the field transmitted through the cavity.

Signal Enhancement An additional technique which acts solely on the gravitational signal is also used in conjunction with arm cavities. This is known as signal recycling and involves placing a mirror between the output detector and the beam splitter which forms a resonant cavity with the rest of the interferometer. This sets how many times the gravitational wave signal cycles through the interferometer, by carefully choosing the resonant bandwidth of this 'signal-recycling cavity' [21, 26, 27]. The specific setup of the recycling cavity on the output used in Advanced LIGO is known as 'resonant sideband extraction' [9, 26]. It is discussed further in Section 2.7.1.

Power Enhancement To ensure the efficiency of the interferometer, a mirror is also added between the laser and the beamsplitter to form a cavity with the interferometer to recycle the input laser mode, a technique known as 'power recycling'. This works because most of the laser light is reflected back along the path to the laser as the detector output is kept near a dark fringe so the interferometer acts like a mirror with respect to the light from the main laser [9, 21].

1.3.3 Noise

Noise in a gravitational wave detector is any signal that contaminates the output strain of the detector or can be mistaken in frequency behaviour for a signal due to a gravitational wave [22]. Due to the large range of sources that could produce this type of signal, the detector needs to be sensitive over a wide audio-frequency band range and this means that even though the detector is aimed at celestial sources it also picks up terrestrial sources in the same frequency range which will potentially be louder or of a similar amplitude to gravitational sources [21, 22].

Mechanical Noise Coupling Due to the fact that the interferometer mirrors need to interact as free masses with the gravitational wave, the test masses are suspended as pendulums which allows them to be treated as free masses above the resonance frequency of the pendulum [22]. However below and at this resonance frequency the masses are not in an inertial frame with respect to the waves and so will induce noise in the detector, or to think of it another way, the masses will move with whatever mass the pendulum is attached to, making any motion in the environment transfer onto the mass and cause the detector strain signal to be affected. For this

reason detectors use multi-stage suspensions that contain passive isolation stages to reduce the amplitude of noise from the environment by the time it reaches the mirror [21,22]. To target noise caused by seismic activity specifically, the suspensions are not attached straight to the ground but are mounted on at least two stages of isolation instrumentation designed to isolate from seismic noise and other ground motion [9, 22, 28].

Thermal Noise Coupling Brownian noise of the interferometer mirrors, suspensions and mirror coatings produces noise in the interferometer strain signal. This is due to thermal energy in these components, which causes several different effects in the detector [9, 29]. One of these is thermal energy in the mechanical modes of the test mass mirrors, known as substrate Brownian noise, which deforms the mirror surface and is a main noise source at the lower frequency end of the range in one of the Advanced LIGO detectors from 40 Hz to 100 Hz [30]. Another noise source is thermal energy in mechanical modes of the coatings which consist of stacks of two different materials, which again would change the shape of the mirror surface and is known as coating Brownian noise. The coatings also provide two noise sources which change the mirror properties in a different way: thermo-refractive noise which means expansion or contraction of coating layers changes the overall refractive index of the coating and thermo-elastic which means expansion or contraction of coating layers changes the position of the mirror surface. The last thermal noise source is suspension thermal noise which is excitation of the modes of the suspension pendulums themselves [9, 21, 29].

Newtonian Noise Newtonian noise occurs in the surrounds of the detector due to changes in the mass distribution in the surrounding environments. This produces a changing gravitational pull on the test masses and is also known as gravity gradient noise [9, 21]. It will limit the sensitivity of the Advanced LIGO detectors in the future between 10 and 20 Hz [30].

Quantum Noise Quantum noise is caused by the intrinsic uncertainty in photon number and momentum in the detector [21, 31]. This can be thought of as the noise induced in the phase of optical fields in the interferometer and their amplitude [21].

The quantum noise was found in [27] to come from vacuum fluctuations reaching the beam splitter via the output port of the interferometer. Some of these photons add in phase in one arm and out of phase in the other, thereby providing a noise in the differential signal at the detector output. The arm cavity mirrors move in response to momentum imparted by the photons and this changing asymmetry between the length of each arm due to the vacuum photons changes the amplitude measured at the output and is the radiation pressure noise. Vacuum fluctuations are also what causes the shot noise at the detector as they add in or out of phase with the output signal from the interferometer [21, 27, 31]. Both of these quantum sources provide a limit to the sensitivity that can be reached using only classical optical techniques, known as the standard quantum limit [21], which will be described in more detail in Chapter 2. The Advanced LIGO detectors' are currently dominated by this noise above 1 kHz [30].

1.3.4 Fabry-Perot Cavities

The arm cavities described previously in Section 1.3.2 and shown in Figure 1.2, work much like simpler versions of the Michelson interferometers. There is a specific length, L, corresponding to a whole number of half-wave lengths, $\frac{\lambda}{2}$, of the laser light in the cavity which will allow build up of light power by constructive interference between light entering the cavity by transmission, a_0, and light which has reflected off the inside surface of the second cavity mirror then the input mirror, a_n. The equations which describe a Fabry-Perot cavity are given in [26]. Equation (1.5)

$$n\lambda = 2L \tag{1.5}$$

shows the wavelength condition for one photon to travel one trip up and down the cavity. In Equation (1.6),

$$n\mathrm{FSR} = \frac{nc}{2L} = f_0 \tag{1.6}$$

f_0, the resonant frequency of the laser is equal to an integer number of free spectral ranges, FSR, of the cavity; where FSR is the inverse of the time taken for one photon to perform a trip up and down the cavity. The time each photon spends in the cavity is a distribution and is set by a

frequency γ, which is the half-width at half-maximum of the circulating power in the cavity as the resonant frequency of the cavity is altered by slowly changing the cavity length. The build-up of power in the cavity can be characterised by the finesse, F, shown in Equation (1.7)

$$F = \frac{\pi}{2\arcsin\left(\frac{1-r_1r_2}{2\sqrt{r_1r_2}}\right)} \tag{1.7}$$

and in Equation (1.8)

$$2\gamma = \frac{\mathrm{FSR}}{F}. \tag{1.8}$$

This is determined by the reflectivity coefficients of the input mirror, r_1 and the end mirror, r_2 and is also the ratio of the FSR and the width of the circulating power resonance at half-maximum, 2γ. These Fabry-Perot interferometers are useful in the arm cavities of detectors as their finesses can be chosen to enhance signals from gravitational waves at a range of frequencies where these are expected and thus make the best use of the light entering the interferometer from the beamsplitter. The power build-up in these cavities means that each photon is in the detector longer, increasing the time it could interact with a passing gravitational wave, this increases the signal measured over a detector with no arm cavities. The high power caused by the build-up in the arms also reduces the effect of shot noise on the output detector of the interferometer, although a limit is placed on the power circulating in the arm cavities by radiation pressure noise which increases as the arm power in the cavities increases [21].

1.3.5 Controlling Length

A technique is needed to hold the Fabry-Perot cavities on resonance, despite vibrations of the mirror surfaces due to noise. This technique is known as Pound-Drever-Hall locking and was first proposed for this purpose in [32]. Firstly, a frequency reference is created by adding radio frequency sidebands through modulation of the light phase. These sidebands are chosen to have a frequency far away from the carrier (main laser) frequency and therefore are not resonant in the cavity when it is tuned near the carrier frequency. This means, on and near resonance, the sidebands are completely reflected by the input mirror but the carrier enters the cavity and res-

onates with the intra-cavity field already there. If we look at the beat detected on the reflected photodiode, this is the sum of the field coupling back through the input mirror and that reflected directly off the front of the input mirror [33]. Part of this beat is the term which varies with the modulation frequency, Ω_1, which can be selected using a process called demodulation [26]. This output now varies in proportion to the distance from resonance, further it is asymmetric around the centre of resonance, as shown in Figure 1.3 [31, 33]. This signal is the amplitude of the

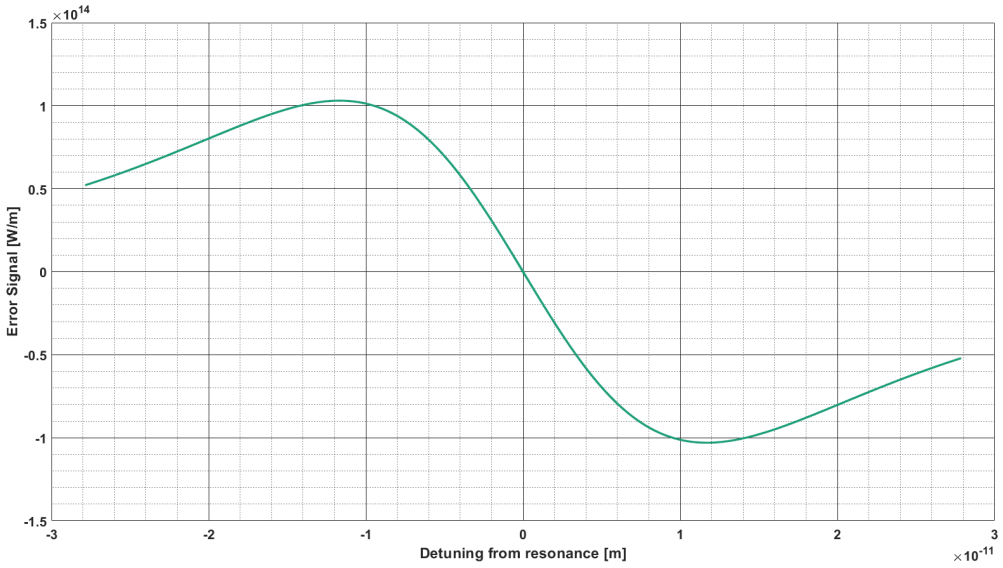

Figure 1.3: Calculation of Error Signal with parameters similar to that used for the experiments presented in this thesis. The experimental error signal is proportional to the amplitude shown, which is the rate of the change of the cavity circulating power with the distance the cavity length is from the resonance point.

imaginary part of the beat between the sidebands and the light from within the cavity. When the cavity is on resonance the carrier field-sideband beats are 180° out of phase and so cancel out. When the carrier frequency is slightly above the cavity resonance frequency, the lower sideband beat is closer to the cavity resonance than the upper sideband beat and vice versa when the carrier frequency is slightly lower than the cavity resonance. The total reflected field is 180° out of phase from one side of the resonance to the other, which is why the signal goes up below the resonance and up above the resonance in frequency [34].

1.3.6 Increasing Sensitivity

The design sensitivity of the current gravitational wave detector network is constrained by several noise sources. Over a large majority of the frequency range where measurements of sources are expected, the sensitivity is or will be soon limited by the quantum noise. How this limit, called the 'Standard Quantum Limit' arises is discussed in more detail in Chapter 2. This work looks at one of these noise sources, radiation pressure noise, specifically one technique used to improve detector sensitivity below this limit.

1.4 GW Detector Development

As they stand just now the LIGO detectors fundamental noise limits in its operating band from 100 Hz to 10 kHz are quantum noise and coating thermal noise. Efforts have been under way for a number of years at various laboratories in order to improve beyond this limit. There are several ways of measuring below the standard quantum noise limit in a gravitational wave detector. In Advanced LIGO the method is to use optical squeezing, which is used to reduce the quantum noise due to shot noise and quantum radiation pressure noise [35]. A different technique that could be used, is to change the shape of the quantum noise by altering the interaction of the optical fields with the detector in some way, using a technique called optical springs, which will be expanded upon in Chapter 2 [31].

1.4.1 Future Planned Detectors

The Advanced LIGO and Advanced Virgo detectors respectively will undergo upgrades known as 'A+' and 'Advanced Virgo+' in the near future. Both of these require hardly any new technologies to be researched or major building changes [35–37]. Both detectors will use frequency-dependent forms of squeezing to improve their quantum noise performance.The next generation of gravitational wave detectors (or third generation detectors) is in the starting stages of design. The two main proposed third generation detectors are Cosmic Explorer in the US, and Einstein Telescope in Europe.

The Einstein Telescope is designed to be a xylophone configuration; two triangular interferometer arrangements will sit in the same facility but will be optimised for different frequencies. Each corner of the triangle consists of two Michelson interferometers, six in all.The arms of each interferometer are at 60° angle, instead of the 90° angle in the usual Michelson configuration. The low frequency one in each corner will use cryogenics to achieve its high sensitivity through low thermal noise mirrors; the high frequency one will use high laser power to increase its sensitivity in a way that would not be possible with a cryogenic system [38, 39].

Cosmic Explorer will use higher powers and longer arm lengths to achieve sensitivity improvement [25, 40]. Due to the long time-scales involved and open nature of the designs, there is still a lot of development needed in terms of detector technologies for both these detectors and so it is useful to keep this in mind when developing engineering ideas for future detectors and research a broad range of techniques and possible problems.

Both telescopes involve higher power resonant cavities than the current generation of detectors and so effort needs to be invested in investigating problems that will arise on controlling high radiation pressure effects in detectors.

1.4.2 Prototypes

Before a technology can be implemented in a final detector design, all aspects of the science and technology involved in the detector have to be looked at. This process usually starts with a theoretical treatment of the science, and then this is put in context of the typical values that might be involved if the technology was scaled up to detector scale. After these initial theoretical calculations a small-scale experiment will be designed to prove the general principles of the technology. This experiment will usually test the technology in isolation from the other subsystems it will need to be integrated with in the final detector. After being experimentally proven to work, the technology will then be tested in a more complex experimental setting that acts like a simplified version of the detector or detector subsystems that the new technology needs to interact with.

This intermediate experiment is known as a prototype, and does not necessarily have to be a full Michelson interferometer. It usually consists of a system of suspended mirrors in vacuum to investigate the new technique's interaction with typical detector control systems and a range of noise sources. There are many prototypes around the world looking at different aspects of future detectors. At Glasgow there is a 10 m Fabry-Perot interferometer of the type used in detector arm cavities, which is used to verify control techniques in interferometers that can then be scaled up to the full detector [3].

1.5 Thesis Motivation

The motivation for using this system to investigate optical springs was to look at implementations that could be used in a future gravitational wave detector such as the use of optical traps to make an optical bar detector [41], or the use of a spring and anti-spring in the signal recycling cavity as in [42]. There was also a need to experimentally investigate the use of negative inertia to make interferometer mirrors more responsive [4, 5, 43], which has not been experimentally tested so far. It should be noted that the current upgrades being implemented for ground-based gravitational wave detectors do not include any of these techniques, as squeezed light injection is being pursued instead [35, 44]. However, it is still useful to learn more about optical spring control in gravitational wave detectors both to inform future detector designs and to improve control of the optical spring effects that already exist in the current generation of detectors and could cause control problems in the future [45].

Chapter 2

Optomechanics

2.1 Quantum Noise Considerations

As mentioned in Chapter 1, quantum noise is now a limiting factor in gravitational wave detectors at higher frequencies [35, 37], and so it is useful to investigate a variety of methods for reducing the effect of this in these detectors.

2.1.1 Standard Quantum Limit

Due to the fact that shot noise and radiation pressure noise scale differently with frequency, it is possible at any frequency to minimise the combination of these two noise sources. The shot noise is not frequency dependent but decreases with higher laser power; the radiation pressure noise decreases with frequency but also increases at higher power [2, 21, 46]. This combination of the two noise sources results in a fundamental limit to the sensitivity of a conventional Fabry-Perot interferometer or a Michelson interferometer such as that discussed in Section 1.3 [2, 21]. As this limit is due entirely to the quantum nature of the light in the interferometer, it is known as the 'Standard Quantum Limit' [21].

2.1.2 Calculation of the Standard Quantum Limit

The standard quantum limit, for the case of a Fabry-Perot interferometer, can be calculated by looking at the spectral density of the two noise sources integrated over the experiment band-

width under consideration, and using them to construct a version of the Heisenberg uncertainty, $\Delta x \Delta p \geq \frac{\hbar}{2}$ [31]. From the radiation pressure noise the back-action noise spectral density,

$$S_{ba} = N \frac{4\hbar^2 G^2}{\kappa} \left(1 + 4 \frac{\omega_{opt}^2}{\kappa^2} \right)^{-1} \tag{2.1}$$

is obtained. Where S_{ba} is the noise spectral density in the force back on the mirrors due to back-action, κ is the full-width at half-maximum of the cavity resonance frequency, G is the differential of the resonance frequency of the cavity with respect to cavity detuning, N is the average number of photons in the cavity, ω_{opt} is the photon frequency, and $\hbar$ is Planck's constant divided by 2π [2]. This noise is caused by the cavity photons giving the mirror random momentum jitter by hitting it. From the shot noise comes the shot noise spectral density,

$$S^{sn} = \frac{\kappa}{16 G^2 N} \left(1 + 4 \frac{\omega_{opt}^2}{\kappa^2} \right). \tag{2.2}$$

which is due to the uncertainty in the number of photons. These are given in the general case for a gravitational wave detector and can be expressed as an uncertainty relation [2, 31],

$$S_{ba} \cdot S^{sn} \geq \frac{\hbar^2}{4}. \tag{2.3}$$

This makes the lowest total fundamental noise,

$$S_x^{SQL} = 2 \left| \chi \right| \hbar \tag{2.4}$$

which depends just on the susceptibility, $\chi = \frac{x}{F}$, of the system and is taken from [7], where S_x^{SQL} is the standard quantum limited sensitivity of the mirror motion in the x direction, and F is the external applied force [2]. This is a combination of the motion of the oscillator due to both types of quantum noise, shot and back-action noise [2, 7].

2.2 Optical Springs

In resonant cavities the light field exerts radiation pressure on the mirrors as a classical force and also as the quantum noise effect mentioned in Section 1.3. Radiation pressure can be utilised to increase the signal produced by a gravitational wave in a gravitational wave detector by creating an effect called an optical spring in the cavity. It can also affect the quantum radiation pressure part of the minimum quantum noise of an interferometric system, reducing it within a specific frequency band.

2.2.1 Coupling of the Mirror Motion and Cavity Mode

The last chapter dealt with normal operation of resonant cavities; to achieve improvement in quantum noise of gravitational wave detectors it is necessary to operate away from the centre of resonance where the cavity is sensitive to small changes in the resonant condition. The equation for circulating power P_c in an optical cavity of the type shown in Figure 1.2 is:

$$P_c = \frac{T_1 P_{in}}{1 + R_1 R_2 - 2 r_1 r_2 \cos(2kL)}. \tag{2.5}$$

This equation is taken from [26], where power transmission coefficient, T_1, is the fraction of the power hitting the back of the input mirror (M1) of the cavity that passes through it into the cavity, the power reflectivity coefficient, R_2, is the fraction of the power that reflects off the intra-cavity surface of the second mirror (M2) which travels back towards the input mirror, R_1 is the fraction of power T_1 reflected from the intra-cavity surface of M1 towards the second mirror, L is the length of the cavity as measured between the two internally facing mirror surfaces and k is the wavenumber of the light circulating in the cavity. The constants r_1 and r_2 are the amplitude reflectivity coefficients for M1 and M2 such that $R_1 = r_1^2$ and $R_2 = r_2^2$. The circulating power in a cavity of this type, with respect to the frequency with which the laser is offset from the cavity resonance, is plotted in Figure 2.1.

The derivative of the circulating power is constant with respect to frequency around the cen-

tre of the curve, that is, the normal operating point of a resonant arm cavity with respect to cavity length. This means that any noise in the circulating field giving deviations in cavity length or laser frequency will be suppressed by the cavity gain and so will not be transferred from the mirrors to the light field or vice versa.

If the control point is moved to the side of the circulating power curve, a point is reached

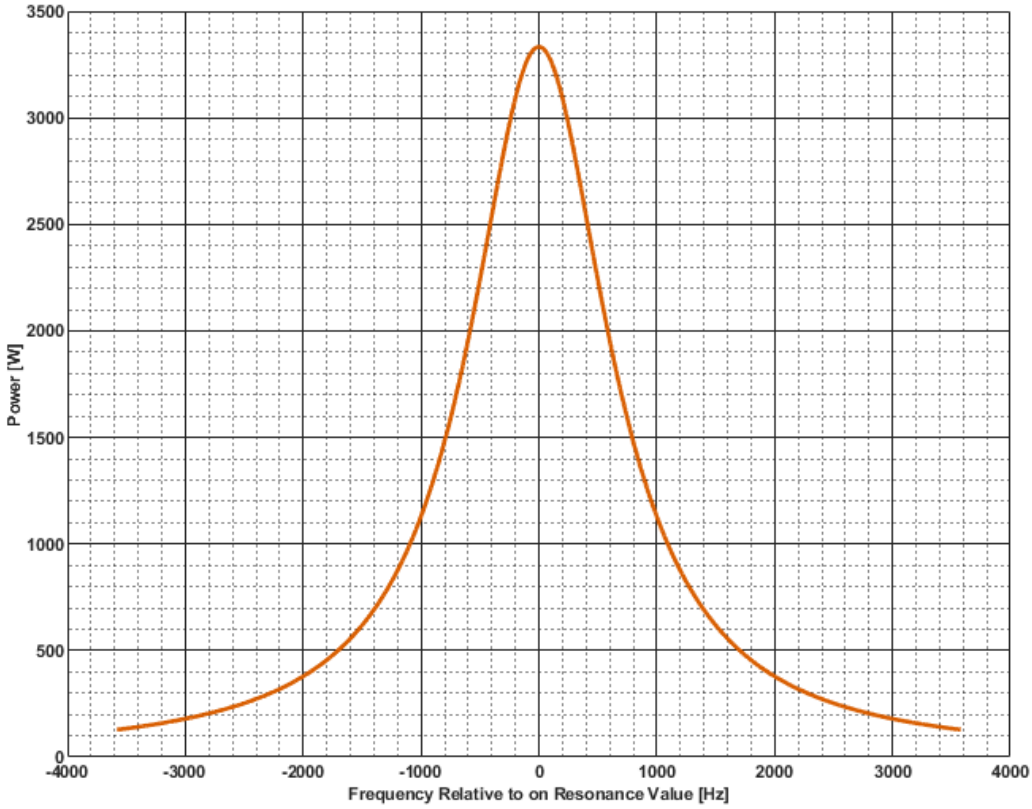

Figure 2.1: Image of variation in circulating power in resonant cavity with frequency offset from cavity resonance, using similar parameters to those of the Glasgow 10 m Fabry-Perot cavity used for the spring experiments in this thesis. Calculated using Equation (2.5).

where the derivative of the circulating power with respect to frequency or length approaches a linear slope and is at a maximum. This can be done by adding an offset to the cavity length or laser frequency to change the resonance condition of the cavity, a technique called ‘detuning’. In this region any small deviations in frequency of the laser or cavity length will couple directly to small deviations in the circulating power in the cavity. This has several implications for the

dynamics of the cavity mirrors.

2.3 Creating Optical Springs

The coupling between small changes in the cavity resonance condition leads to direct changes in the circulating power, thus the converse is also true. Therefore the field circulating in the 'detuned' cavity will cause the mirrors of the cavity to move. This field exerts a force due to radiation pressure on the mirrors and so changes in the length of the cavity or frequency of the laser will directly modulate the dynamical behaviour of the cavity mirrors in a way that would not occur in a cavity on resonance.

The coupling between cavity light field fluctuations and cavity length is known as an optical spring because it couples a length change to a force. Following this analogy the coupling factor that determines the strength of the spring is called the optical spring constant and it scales with the detuning from the length at which the light builds up maximally in the cavity.

The spring constant is

$$K_{\mathrm{OS}}\left(\Omega << \delta\right) = \frac{8kP_c r_2^3 r_1 \sin\left(\frac{4\pi\delta L}{c}\right)}{c\left(1 + R_1 R_2 - 2r_1 r_2 \cos\left(\frac{4\pi\delta L}{c}\right)\right)}, \tag{2.6}$$

where k is the wavenumber of the laser, L is the cavity length and c is the speed of light. It has a constant part dependent on the maximum circulating power in the cavity, P_c, the reflectivity r_1, of the input cavity mirror and the reflectivity of the output mirror r_2. There is also a part δ that varies with the frequency offset between the laser and the cavity resonance frequency in Hz [1, 2, 26] This equation assumes that the frequency at which the system is being driven, Ω, is much lower than the detuning applied so the spring constant does not change appreciably as the mirror swings back and forth [1]. The driving or 'probe' frequency would alter the spring constant if the mirror motion was fast enough that the field inside did not have time to respond and this would mean the cavity field response is appreciably delayed in phase from the mirror

motion [2].

In order to operate the optical system off the centre of the resonance of the resonant cavity where the derivative of power with respect to cavity length is non-zero, the control system must have a static offset applied. The size of this offset in relation to the half-width at half-maximum, γ, of the cavity determines how strong the opto-mechanical coupling is. The coupling is strongest when the power has the steepest slope on the side of the resonance curve where the linear term in the derivative is at its maximum [3].

2.3.1 Quantum Noise Reduction with Springs

As has been already discussed, the optical spring allows small variations in position or light level to couple to each other. This also holds true for the noise sources that make up the quantum limited noise of the experimental system. In the analysis above, the shot and back-action noise are independent. However, where the derivative of radiation pressure with position is non-zero, any fluctuations in cavity power will be transferred directly to the mirrors. This includes the small photon fluctuations that give rise to the quantum noise in the mirrors and means that the spring correlates the noise in the laser field to the 'back-action' or radiation pressure noise of the mirrors. Any correlated noise sources result in a reduction on the contribution of those noises to the overall noise of the system. This means that S_{ba} or S_{sn} can be reduced by the spring, but in order to conserve the energy in the system the overall integrated spectral noise density will increase at frequencies away from the spring resonance where the reduction is strongest. The new expression for the SQL in the presence of correlations between the back-action noise and the shot noise shows this reduction,

$$S_{ba} \cdot S^{sn} - \left|S_{corr}\right|^2 \geq \hbar^2 + 2\hbar \left|\Im S_{corr}\right| \tag{2.7}$$

and is given in [7]. The term S_{corr} is the correlated noise spectral density between the radiation pressure noise and the shot noise. For a cavity with one spring this gives $S_{corr} \neq 0$, because of

the presence of the spring. This results in a modified SQL of

$$s^{SQL}_{\mathrm{F,spring}} = 2\hbar \left|\Omega^2 - \omega^2_{opt}\right| \tag{2.8}$$

given in [3, 7], where ω^2_{opt} is the new shifted resonance of the cavity while detuned and Ω is the measurement frequency. This comes from the original SQL for the case with no detuning,

$$s^{SQL}_{\mathrm{F,resonant}} = 2\hbar \left|\Omega^2 - \omega^2_{m}\right|. \tag{2.9}$$

If it is assumed that the mechanical resonances of the mirror pendulums are much lower than our measurement frequencies and the frequencies at which the optical spring is resonant, this can be simplified to $2\hbar\Omega^2$. Thus, when the mirrors move close to the optical spring resonance frequency in the detuned cavity, the SQL will be reduced from the on-resonance value by $2\hbar\omega^2_{opt}$ [4, 5, 7].

The modification of quantum noise near the optical spring resonance frequency can be used in gravitational wave detectors to increase their sensitivity to a particular frequency of source by tuning the resonance frequency of the signal recycling cavity mirrors using an optical spring [21,26].

For the measurement sensitivity to reach the SQL, the classical noise sources must be lower than the level of the quantum noise at this frequency for quantum effects to be observable. This also holds for the optical spring modification of the quantum noise, but the classical spring effect will still be observable above the other noise sources even if the quantum noise reduction is not, as is the case in the interferometer that is the subject of this thesis.

2.4 Optical Spring Constant

To determine the dynamics of an optical spring, its effect on the suspended masses of the cavity can be looked at. As mentioned, the spring modification of the force depends on the detuning of the cavity; but also for a mirror probed by a force at frequencies Ω, on the order of the detuning and the cavity linewidth, the dynamics of the spring depend on the frequency of the probing force.

In fact, in the specific case considered in this thesis, because the cavity resonance is composed of a build-up of light waves, the cavity resonant field takes time to change in response to the mirror motion. This results in a part of the spring constant that is out of phase with the real rigidity and is proportional to the speed of the mirrors in the time domain and thus the frequency of the mirrors in the frequency domain. This is represented by making the equation for the full frequency-dependent optical spring a complex rigidity. As this term is proportional to velocity it acts to damp or anti-damp the motion of the mirror, depending on the phase difference between the real and imaginary parts of the spring constant [2, 3].

2.4.1 Equation of Motion

For a pendulum of mass, m and extension from its origin directly below the point of suspension, x, the sum of the forces on it can be analysed to give an equation equal to the driving force $F_{\mathrm{d}}(\Omega)$,

$$F_{\mathrm{d}}(\Omega) = -m\Omega^2 x(\Omega) + K(\Omega)\, x(\Omega) \tag{2.10}$$

representing its motion in the x direction. The last term represents the optical spring effect in the cavity of length, L [2,4,5]. The first part of this equation is caused by the mechanical parameters of the suspended mass and the second by the optical field (of frequency ω_0) interacting with this mass.

2.4.2 Susceptibility

The simplest way of describing an optical spring mathematically is in a similar form to a conventional mechanical spring where the spring constant is radiation pressure force on the mirrors F divided by extension of the spring from equilibrium x. This is complicated by the photons having a distribution of different frequencies affected by the storage time of a photon in the cavity and the cavity length, due to the Doppler shift of the cavity mirrors altering the frequency of the photons as they resonate in the cavity. This frequency spreading of the photons is what gives rise to the frequency dependent nature of the optical spring effect. It also means that the spring constant will be complex due to the fact that the cavity length or laser frequency changes

will lead the cavity field radiation pressure changes by an amount which depends on the extent to which the fundamental resonance frequency is Doppler-shifted by the cavity, that is the frequency 'width' of the circulating photon distribution γ as referred to previously in Section 2.3. From 2.10 the susceptibility of the mass can be obtained by dividing the equation of motion by the force on the mass. The susceptibility is defined as

$$\chi(\Omega) = \frac{x(\Omega)}{F_{\mathrm{d}}(\Omega)} \tag{2.11}$$

in [2,4,5] and defines how a mass affected by a spring moves when excited by an external force, which makes the expression for the susceptibility,

$$\chi(\Omega) = \frac{1}{-m\Omega^2 + K(\Omega)} \tag{2.12}$$

in the case that the damping and rigidity terms of the pendulum can be neglected [5].

2.4.3 Frequency Dependent Springs

The optical spring coupling varies with two things; the detuning of the system from its resonance position, which sets the derivative of circulating power with cavity length/laser frequency, and the power built up when it is on resonance, which sets the overall height of this resonance and thus the relative strength of the radiation pressure effects. For a system which is tuned up in frequency from the original cavity resonance frequency, that is the cavity is made shorter, there will be a positive derivative of circulating power with cavity length on this side of the resonance, and thus radiation pressure pushing the mirrors outwards will increase if the cavity length increases at this point, causing the mirrors to swing away from equilibrium under influence of the radiation pressure force. This means the system has negative rigidity or an anti-restoring force [2,6].

For a system which is tuned down in frequency from the original cavity resonance frequency, that is the cavity is made longer, there will be a negative derivative of circulating power with cavity length on this side of the resonance, and thus radiation pressure pushing the mirrors outwards

will decrease if the cavity length increases, causing the mirrors to swing back towards equilibrium under influence of the gravitational force until the radiation pressure force is high enough to balance this force. This means the system has positive rigidity or a restoring force [2, 6, 7].

2.4.4 Damping

Another effect that happens in tandem is that this restoring/anti-restoring force reduces at higher frequencies. This is due to the rate of decay of power from the cavity, characterised by the linewidth, γ. Due to the fact that light is stored in the cavity for a certain time, this means that the cavity field response happens some time after any small variations in mirror position, and this gives a force which acts with a phase delay back on the mirrors, which is dependent on the velocity of the original change in position. Some of this force is in phase with the original motion and gives rise to the rigidity part of the spring and some is out of phase and thus acts as a damping term. This damping term is a velocity dependent force as its magnitude depends on the original time delay between the mirror motion and the cavity response. It will be out of step with the original motion and so will act in the opposite direction to the static force from the spring rigidity and thus act as an imaginary term in the spring constant [2, 6, 7].

Another way to think of the damping effect in the frequency dependent spring constant is in terms of the work done by the radiation pressure over one mirror oscillation. As $F \cdot x = \Delta E = W$, if the system is locked on the spring side of the circulating power curve as the mirror moves into the cavity the force on the mirror increases and the cavity length decreases. However, due to the time delay between the motion and the radiation pressure force the force-displacement will sketch out a curve in force-displacement over time that forms an ellipse tilted towards the centre of resonance and directed round the ellipse in the clockwise direction. The work done is the area of this ellipse enclosed by the path of the oscillator in force-displacement as it oscillates once along the radiation pressure vs. distance curve by a small amount [2, 7, 47–50]. This can be thought of as the radiation pressure force giving energy to the mirror and so this leads to anti-damping [2, 7].

Conversely, when locked on the anti-spring side of the circulating power curve as the mirror

moves into the cavity the force on the mirror decreases and the cavity length decreases. There is still a time delay between the motion and the radiation pressure force so the force-displacement will sketch out a curve in force-displacement over time that forms an ellipse tilted towards the centre of resonance and directed round the ellipse in the anti-clockwise direction. When the work done in both areas is integrated a positive work for the spring and negative work (similar to conventional mechanical friction) for the anti-spring is obtained, leading to damping of the mirror motion [48, 49].

The damping terms gets weaker when the probe frequency reaches the same order as the cavity linewidth because the work done by the damping or anti-damping term decreases as the area enclosed in one oscillation decreases. The damping strength can be described as the imaginary part of the optical spring constant (with units of N/m). As can be seen from Figure 2.2 the damping strength changes as the mirror motion increases in frequency, eventually reducing to a very small value that tends to a constant in frequency space. This also holds for the rigidity term, except the spring rigidity also changes sign, as well as slope, at frequencies above the cavity linewidth 750 Hz, as seen in Figure 2.3 where the rigidity is the real part of the optical spring constant in N/m. This would imply that neither the damping nor the rigidity are linear in frequency and so a more general expression,

$$K(\Omega) = \frac{8kP_c r_2^3 r_1 e^{\frac{-2i\Omega L}{c}} \sin\left(\frac{4\pi\delta L}{c}\right)}{c\left(1 - 2r_1 r_2 e^{\frac{-2i\Omega L}{c}} \cos\left(\frac{4\pi\delta L}{c}\right) + r_1^2 r_2^2 e^{\frac{-4i\Omega L}{c}}\right)} \tag{2.13}$$

is used to describe the spring, taken from [1, 2, 26]. The variables correspond to those used in Equation (2.6). In this equation there are terms which vary with frequency, which give rise to the frequency dependent rigidity and damping, and a term which is independent of frequency which gives us the rigidity of the spring at 0 Hz. There is also a term varying with frequency squared which gives rise to a term analogous to the restoring force of a mechanical spring which depends on its mass, and is plotted in Figure 2.4. It can be seen from Figure 2.4 that the inertia-like term also changes sign and slope with frequency.

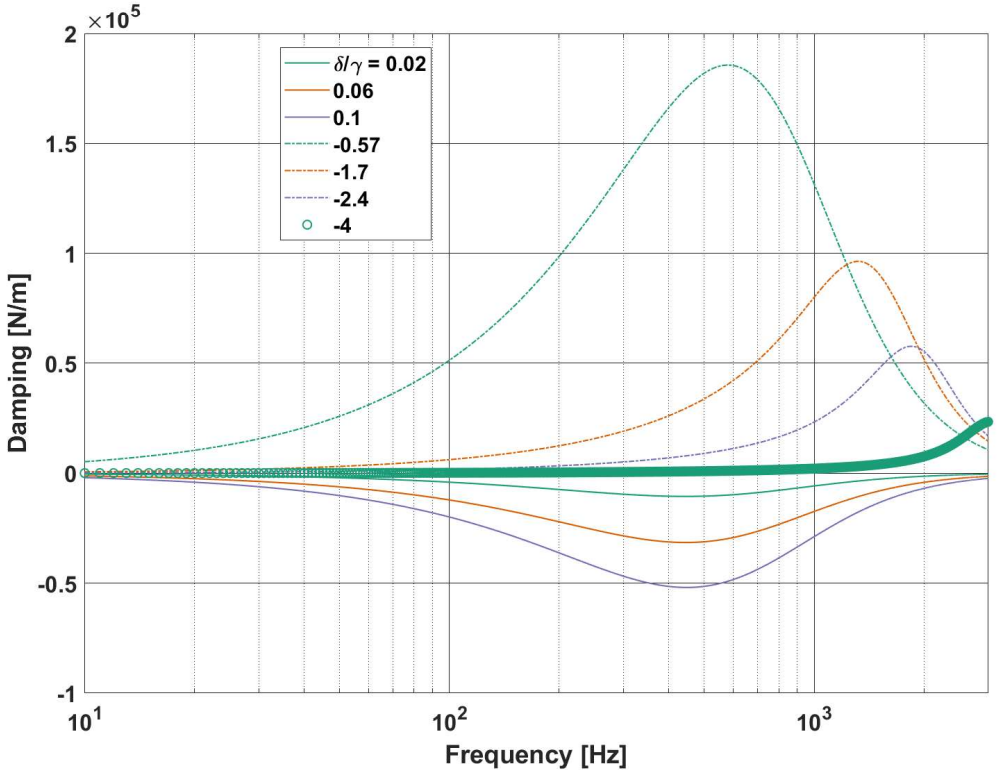

Figure 2.2: Damping strength of frequency-dependent spring varying with the mechanical frequency of either cavity mirror. Different plots correspond to different static detunings added or subtracted from the resonant cavity length. This quantity is the imaginary part of $K(\Omega)$ expressed in Equation (2.13) using the basic parameters from the experimental setup. Equations were obtained from work in [1–6].

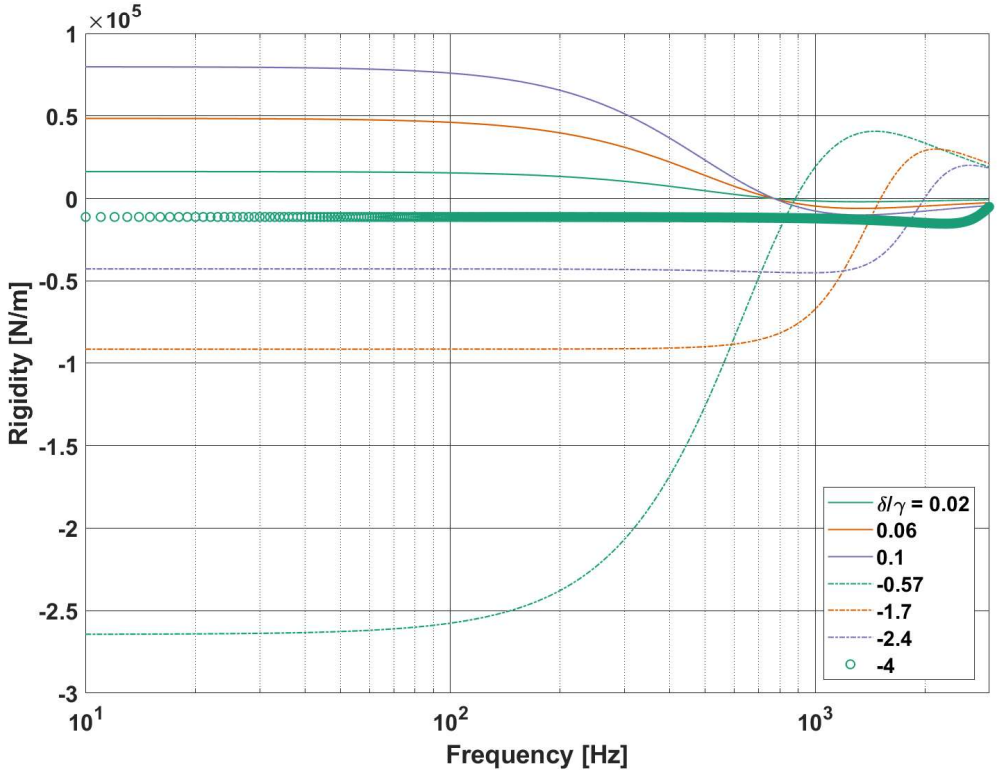

Figure 2.3: Rigidity of frequency-dependent spring varying with the mechanical frequency of either cavity mirror. Different plots correspond to different static detunings added or subtracted from the resonant cavity length. This quantity is the real part of $K(\Omega)$ expressed in Equation (2.13) using the basic parameters from the experimental setup. Equations were obtained from work in [1–6].

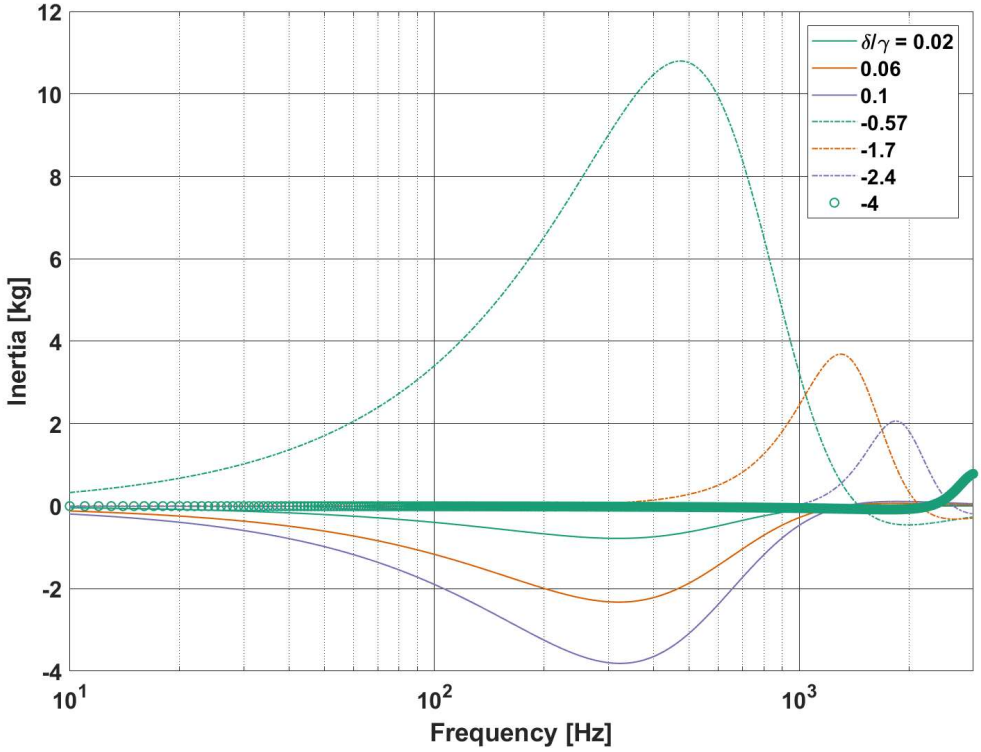

Figure 2.4: Inertia of frequency-dependent spring varying with the mechanical frequency of either cavity mirror. Different plots correspond to different static detunings added or subtracted from the resonant cavity length. The inertia is found by taking the derivative of the optical spring constant, $K(\Omega)$, with respect to frequency squared, Ω^2 expressed in Equation (2.13) using the basic parameters from the experimental setup. Equations were obtained from work in [1–6].

To obtain Figures 2.3, 2.2 and 2.4, the field equations for the light in a detuned cavity were solved numerically to calculate $-\frac{dF_{rad}}{dx}$ for each detuning; then the frequency dependent equation was used to determine how each part of the spring constant varies with the frequency of the mirrors, at various cavity detuning values.

2.5 Stability of Optical Springs

2.5.1 Optical Springs as Feedback Loops

If the response function in Figure 2.5, of a single spring and anti-spring at the same detuning magnitude but with opposite signs is plotted, the magnitude and phase can be seen to vary with frequency. In both cases the spring resonance corresponds to a phase lag of motion relative to the force applied. This means that the rigidity at resonance in springs and anti-springs is 90° ahead of that at DC, and occurs around 800 Hz. This is dynamically unlike a mechanical spring where the motion and force are in phase below the resonance leading to positive rigidity of the system, and the motion of the spring mass lags the applied force by 90° phase above the spring resonance, leading to damping. Knowing this helps to decide what is needed to control the system. This graph is a good way of getting a sense of how the spring and anti-spring behave in the system and checking that the magnitude and phase of the rigidity scales identically with frequency but with opposite sign for springs and anti-springs.

2.5.2 The Effect of Detuning on Stability

Similar to a simple negative feedback loop in electronics, the stability of an optical spring system can be evaluated by looking at its open loop gain transfer function in the complex plane and applying the Nyquist criterion. This states that a Nyquist plot of a transfer function GH can reveal poles of the corresponding closed loop transfer function $\frac{G}{1+GH}$. This is because the system will be unstable if the poles have a positive real part, as this results in an output signal which does not converge to the control point in the time domain. The Nyquist criterion is applied to the full open loop transfer function of a system: if the plot circles the (-1,0) point on the real axis

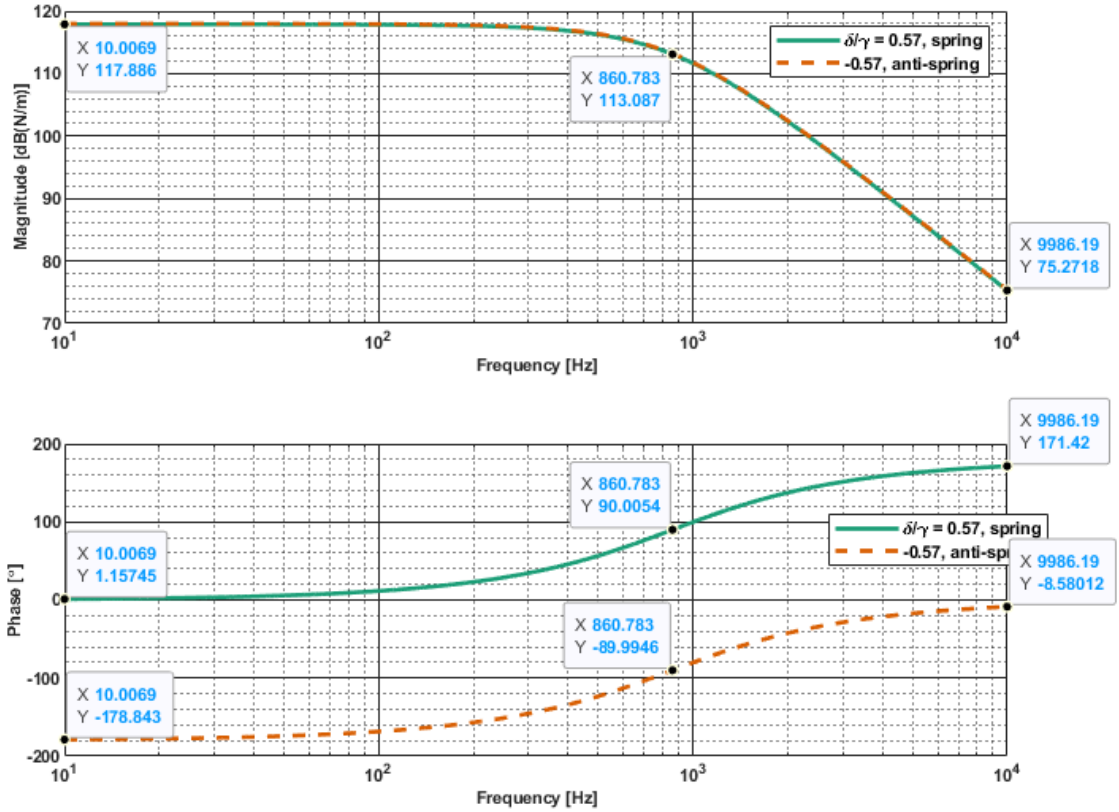

Figure 2.5: Image of K for spring and anti-spring both detuned to a magnitude of 0.57 linewidths. The rigidity characterises the response of the system to an external force. As can be seen from the green trace, mirror motion lags the spring force meaning the system has a positive rigidity and as can be seen the phase lead increases with frequency, coming closer to instability leading to an anti-damping effect. The converse happens for the anti-spring (orange-dashed line) which is 180° out of phase with the spring across the whole frequency range. It starts off with a negative rigidity due to the spring force lagging the motion, but the phase decreases with frequency and the system becomes closer to stability at higher frequency.

of the Nyquist plot in the clockwise direction, there is one more zero than pole in the open loop transfer function which has a positive real part and so makes the resulting $\frac{G}{1+GH}$ unstable [51]. For example in an optical spring there are two poles at $-i\Omega = -\gamma \pm i\delta$, which contribute two poles to the overall closed loop transfer function with a negative real part, resulting in an unstable system unless something is added to stabilise the poles [31]. This can be done with the precise design of a control system [51].

2.5.3 Modification of Mirror Pendulums

It makes more intuitive sense to think of the optical spring connected to a mechanical pendulum and acting to modify its dynamics. This can be characterised in the susceptibility of a cavity with a spring mentioned in (2.12). For a simple Fabry-Perot cavity the m will be the reduced mass of the cavity mirrors [3]. It is possible to then re-analyse the stability of a system by looking at the susceptibility of the combined system, χ_{spring}, measured in m/N and plotted in Figure 2.6. The combined susceptibility is expressed simply for this analysis using (2.12) where the first term is the susceptibility of a free-mass with the reduced mass of the actual experimental cavity is used for illustrative purposes, and the second term is the full frequency-dependent optical spring.

2.5.4 Control of Instabilities

Since the anti-spring is unstable at DC, a control law is needed with a lot of gain at low frequency and DC to balance the anti-restoring force on it. This can be acheived using a filter with flat gain at low frequency that then decreases in gain with a slope of $\frac{1}{f}$ after some cut-off frequency, after which the anti-spring damping provides most of the restoring force at high frequency. This type of filter is known as an integrator. Conversely, since the spring is stable at DC, a filter is needed with a lot of gain at high frequency to balance the anti-damping force on it. Thus a filter can be used with low gain at low frequency that increases in gain with a slope of f before some cut-off frequency, after which the gain can be flat in frequency and high to counter the anti-restoring force at high frequency. This type of filter is known as differentiator. However, the servo system needs to be more complicated than the one described, shown in Figure 2.7. In a real experiment

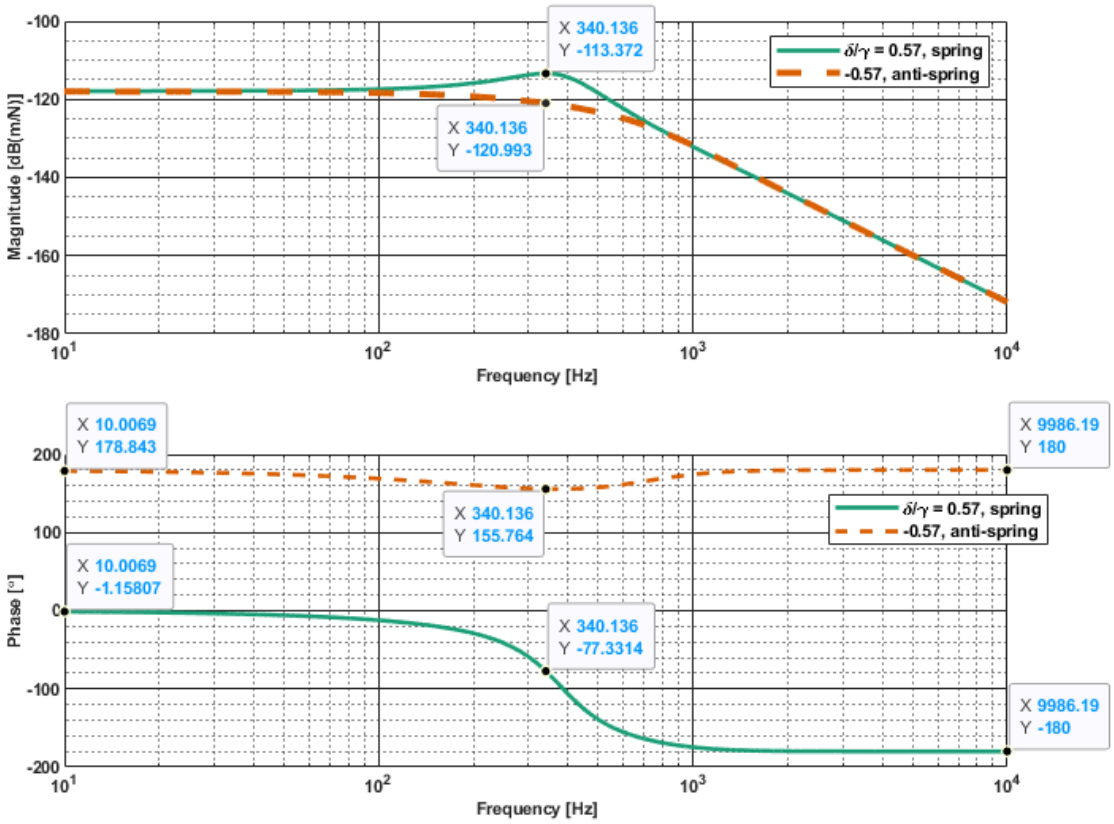

Figure 2.6: Susceptibility of an optical spring (green solid line) coupled to a mirror pendulum varying with frequency of force applied to mirror. A resonance is visible in the magnitude, this has been shifted down with respect to the spring resonance and up in frequency with respect to the natural fundamental resonance of the pendulum (at 0.69 Hz [3]). The orange dashed line shows the same plot of suceptibility but with an anti-spring coupled to the mirror pendulum instead. The resonance can be seen in the spring because the spring anti-damping makes the damped pendulum resonance narrower, and not in the anti-spring case as the anti-spring damping works to damp out the pendulum resonance [7].

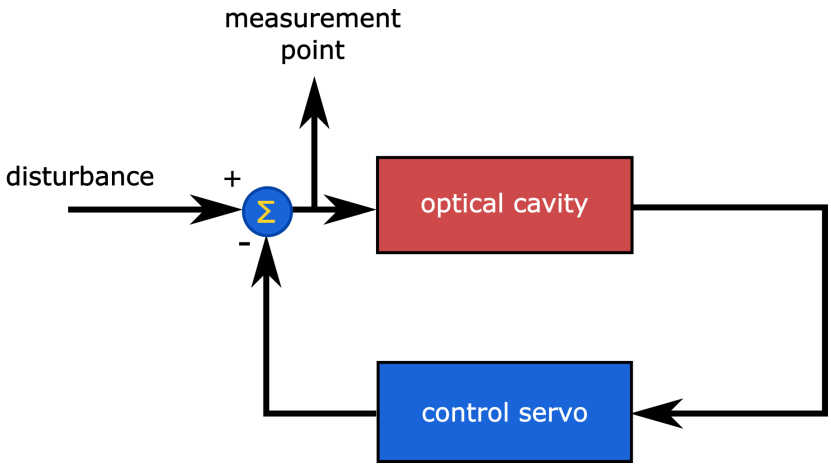

Figure 2.7: Feedback system of spring and its control by an external electronic servo.

there are other components that have a frequency dependent effect on the gain and phase of the system, and so need to be accounted for in control system design. More details of the control system used in the real experiment are given in the next chapter.

2.5.5 Combining Different Springs

In the case of two coupled springs, the susceptibility of the system can be described as,

$$\chi = \frac{1}{-m\Omega^2 + K_1 + K_2} \tag{2.14}$$

where K_1 is the frequency dependent spring constant of the first spring, K_2 is the spring constant for the second, and m is the mass of a cavity mirror coupled to the springs. Unfortunately, unlike the approach in [5], this cannot be described as a linear sum for springs where the detuning is in the same region as the linewidth and the frequency of the external force, so a numerical approach is relied upon to calculate the spring constants for the frequencies of interest. The spring constants can be added together as they contribute independently to the force acting on the mirror [1, 5]. Since there is a common cavity for the two springs, they have the same γ.

2.6 Experimenting with Multiple Optical Springs

Two separate experiments were carried out involving creating multiple springs in this same apparatus to find possible examples of negative inertia and optical trapping.

2.6.1 Optical Traps

Since the total variation in restoring force acting on a mirror is the linear combination of the optical spring constants of the optomechanical systems affecting it; it is possible to combine springs in an experiment to create a system with different dynamics from any one spring or anti-spring. If two springs/anti-springs are combined the resultant system will behave with susceptibility,

$$\chi_T = \frac{1}{-m\Omega^2 - \Re\left(K_T\right) - \Im\left(K_T\right)} \tag{2.15}$$

[1,3,4] where the two springs constants and thus the dynamics of the spring and the anti-spring sum together. If the powers and detunings are chosen correctly the total damping term $\mathfrak{I}\left(K_T\right)$ will have a negative sign, acting to reduce the displacement of the mirror on timescales of the order of the inverse damping constant and a restoring force $\mathfrak{R}\left(K_T\right)$ which acts in opposition to the direction of motion of the cavity mirrors. Thus the motion of the system will tend to stability over time and behave like a conventional damped mechanical spring. For a system that was only limited by the standard quantum limit over most of its range this would result in an optomechanical system acting as a quantum mechanical oscillator in the degree of freedom affected by the spring combination. This can be called an optical 'trap' as the motion of the mass will be reduced below its normal $\frac{kT}{2}$ energy per longitudinal degree of freedom due to Brownian motion [52].

However if the noise of the system is above the quantum noise limit the system will not behave as a 'cooled' quantum mechanical oscillator but will have increased gain below the unity gain of the combined spring system and this system will be stable without the need for an external control system if carefully tuned, it can hold the mirror stable and keep the cavity locked. Since electronic servos impose sensing and actuation noise on a negative feedback system such as this, the classical optical 'trap' still allows the noise of the system to be decreased, just not below the standard quantum limit.

2.6.2 Negative inertia

Since it is possible to combine two springs to stabilise a suspended mirror optomechanically, it follows that it should be possible to modify the spring/anti-spring combination to achieve other effects. Specifically, if instead of a highly detuned spring and a much smaller detuned anti-spring, a highly detuned anti-spring and a less detuned spring are created, a system can be produced with increased motion that has the same form as a free mass spring. The desired behaviour comes from the behaviour of the total optical spring constant which acts to cancel some or all of the inertia

of the system, increasing the susceptibility, (2.12), giving the new increased susceptibility,

$$\chi(-i\Omega) = \frac{1}{-m\Omega^2 - m_{opt}\Omega^2} \tag{2.16}$$

to incoming signals that would be picked up by the apparatus. That is, if this was incorporated into a gravitational wave detector it would increase its response to gravitational waves in the bandwidth where the inertia has been decreased [4, 5]. Looking back at the equation for the inverse susceptibility, (2.14), it is necessary to search for the part of the measured susceptibility that is proportional to Ω^2 and thus represents the total inertia $\chi^{-1}_{inertia}$, and ideally engineer this to cancel out the inertia of the free mass completely. If the coefficient of the term that varies as $-\Omega^2$ is tuned to be very small, this results in some or total cancellation of the inertia provided by the free mass, m, as in

$$-1 < \frac{m_{opt}}{m} < 0 \tag{2.17}$$

where m_{opt} is the coefficient of the optical inertia. There are two more conditions that must be met, because there are two other terms in Equation (2.15) than the one representing the inertia: the rigidity (real part) of the double spring that is frequency independent in the numerator and the damping (imaginary) term that varies as $-i\Omega$. It is possible to tune the strength of both the spring and anti-spring to cancel out the rigidity parts of the spring constant. However, unlike the analysis presented in [4, 5] it is impossible in our system to cancel out the damping parts of the expression [4, 5].

With respect to the friction, it is possible to cancel some of it, but it will be impossible to do this completely unless it is ensured the spring and the anti-spring have different linewidths, which is not the case for a conventional Fabry-Perot cavity where the mirrors are of equal reflectivity for both frequencies being used to create the springs. So for the purposes of the experiments in this thesis it is assumed that the system will still have some anti-damping over some or a large part of the experimental frequency range. In that case the idea is to compensate for any left-over anti-damping the system creates with a servo that works to damp the system and make the whole thing stable [4, 5].

Another caveat to this is that (2.17) is only valid when the frequency of the measurement of the spring, Ω is small in relation to γ and δ_1, δ_2. This allows the sum of K_1 and K_2 to be linearised so that $K_t = \mathfrak{R}\left(K_1\right) + \mathfrak{R}\left(K_2\right) + \mathfrak{I}\left(K_1\right) + \mathfrak{I}\left(K_2\right)$. When this is not the case, that is at higher measurement frequencies close to or above the detuning or cavity linewidth, it is not valid to ignore the terms that vary with higher powers of frequency, as has been done in [4,5] as these will contribute more strongly to the size of the total susceptibility of the mass. So in practice, if this is the case, the simplest way to find negative inertia in this complicated system is to derive a measurement of the total susceptibility of the system and look for a region which behaves like an inertia, that is, it varies with $-\Omega^2$. The susceptibility of the free mass at this point $\frac{1}{-m\Omega^2}$ must be less than that of the total inertia, χ, for the system to have negative inertia. However, a reduction in inertia of the suspended mirror in the negative inertia can be obtained [4,5].

2.7 Optical Springs in Real Cavities

2.7.1 Optical springs in detectors

The signal recycling cavity used in most modern large-scale gravitational wave detectors is used in the resonant side-band extraction configuration. This involves tuning the length of the signal recycling cavity to make it resonant or near resonance for a broad range of signal sidebands so that these frequencies are extracted from the arm cavities before leaking out of the signal recycling mirror to the detector [9,53]. This cavity mirror can also be detuned from resonance, with the effect of enhancing the response of the detector at the corresponding detuning frequency, and creating an optical spring like that in a detuned Fabry-Perot cavity as described earlier. This increases the detector sensitivity to a specific source or range of sources at these frequencies [9,22,26,53]. Since control of the broadband detector is already made complicated by the various degrees of freedom that need to be controlled, introduction of an optical spring means that it is important to investigate aspects of optical spring dynamics and their control in prototype detectors, as this resonant mode of signal extraction is already used in Advanced LIGO [30].

2.7.2 Increasing Sensitivity Below SQL

Optical springs can be used to increase the sensitivity of gravitational wave detectors through shaping the noise limited sensitivity of the detector in a band where the quantum radiation pressure noise is the dominant detector noise. They provide a dip in the standard quantum limit near the spring resonance but a rise in the SQL away from this frequency as denoted by equation (2.8). As mentioned in [6] introduction of an optical spring into the detector causes instability due to the anti-damping it gives, and suppresses the gravitational wave response in the low frequency region where the optical spring has rigidly coupled the mirrors of the arm cavities to the signal recycling mirror. These two effects need to be controlled and controlling them electronically can add in noise from the extra electronic servo, due to the detection of photons that needs to take place to produce a control signal, resulting in shot noise in that signal. The authors thus propose using an anti-spring in tandem to either cancel the anti-damping of the spring and partially cancel the rigidity or to stabilise the system by providing lots of damping, in effect creating an optical trap. In addition the optical spring resonances can be chosen such that the range over which the SQL is decreased can be widened, meaning that this could be used in future tuned advanced detectors to make them sensitive to a wider range of sources [6].

2.7.3 Increasing Detector Response Broadband

Negative inertia configurations can also be used in future large scale detectors in order to increase the susceptibility of the cavity mirrors over a wide frequency band. This improves their quantum noise limited sensitivity to gravitational waves and analysis has been carried out of the initial gains in sensitivity possible using this in Advanced LIGO [4, 5].

2.7.4 Previous Optical Springs in Glasgow 10 m

Some work has already been done on control of optical springs in high power, detector-like cavities by John MacArthur [54] and investigating coupling of dynamic effects between springs and anti-springs by Neil Gordon, [3]. Some of this most recent work resulted in investigation of the trapping effect on one of the mirrors of the 10 m system, but did not go all the way towards

completely classically trapping the mirror, without the aid of a control servo at all frequencies [55]. This means there is still room to investigate a full 'all-optical' trap for one of the mirrors in the Glasgow prototype in the manner of that done by Corbitt and colleagues in [56] and by Kelley and colleagues in [57]; where the spring is held over some broad frequency range by optomechanical feedback forces alone. No experiments have yet been carried on negative inertia in the field of gravitational research, so this is worth investigating as a technique which could be used to improve the detector response to a signal in future detectors.

Chapter 3

Experimental Layout

The spring measurements described in this thesis use two 10 m Fabry-Perot cavities. One cavity is used to create the springs and anti-springs, and is of a very high finesse, to allow strong optomechanical systems to be investigated. This is known as the left-hand cavity. The suspension supporting the end mirror of this cavity, also supports the end mirror of another cavity. This cavity, the right-hand cavity, is much lower in finesse and therefore it has a much lower circulating power. As this cavity is mechanically connected to the left-hand cavity, via the central mirror suspension, it can be used as a meter for the dynamics of the left-hand cavity. This is possible as both cavities' lengths are controlled by separate length control servos which feed back to the input mirrors of the cavities, so motion of the shared mirror will result in both input mirrors being pushed by the control feedback to compensate this length change. The opto-mechanics will cause the central mirror (CTM) to appear heavier or lighter depending on the detunings used in the spring and anti-spring, the effect of which can then be seen in the right-hand cavity.

A simple layout of the experiment is shown in Figure 3.1. 10 MHz sidebands are added to the main laser in order to control the left-hand and right-hand cavities so they follow its central frequency when both of these cavities are on resonance. The frequency reference cavity shown in the diagram is used as a frequency reference for the main laser above the cross-over at 19 Hz, and below this frequency the main laser sidebands are used as a reference to control the length of the cavity. Plainly, below 19 Hz the frequency reference cavity follows the laser in frequency and

above 19 Hz the laser follows the frequency reference cavity. The secondary laser is phase-locked to a tunable frequency distance (set by the local oscillator) from the main laser and so uses it as a frequency reference. Both lasers, at their different frequencies, are used to create separate detuned fields in the high finesse cavity. This chapter details the optical setup of the experiment and the measurement of the fundamental cavity parameters such as input power, mode-matching, and frequency noise. The basic layout of the mirror suspensions is then discussed, before an explanation of the control of the lasers and the cavities used for the main experiments. The experimental cavities used in this experimental work are high power Fabry-Perot cavities, which are part of a 10 m prototype interferometer used for testing gravitational wave detector technologies.

3.1 Optical Setup

Light is prepared for input to the experiment on a table shown in Figure 3.2.

3.1.1 Lasers and Input Optics

The first component after the lasers are quarter-wave plates, which when optimised for maximum throughput, ensure circularly polarised light into the half-wave plates which when optimised in turn rotates the polarisation vectors till the maximum power in each beam is in the s-polarisation, rather than p-polarisation, component [58]. After the waveplates are the Faraday isolators. These work to stop back reflections from optics further down the beam towards the experimental cavities, as if these get back to the laser they can interact with the mode circulating in the laser cavity and add noise to the beam it outputs. On entering the isolator the beam polarisation should be lined up with the primary axis of a polarising beamsplitter on the input, after this it travels through a component called a Faraday rotator [59]. There is a constant magnetic field in this material that rotates the polarisation of the input field a constant amount. The amount of rotation is dependent on the material used, and the relative direction of the magnetic field with respect to the direction of beam propagation [60]. The rotator material and field is optimised to ensure that the beam is rotated by 45° [60], then at the output of the Faraday it goes through another polarising beamsplitter aligned with the outgoing polarisation. The component of any back re-

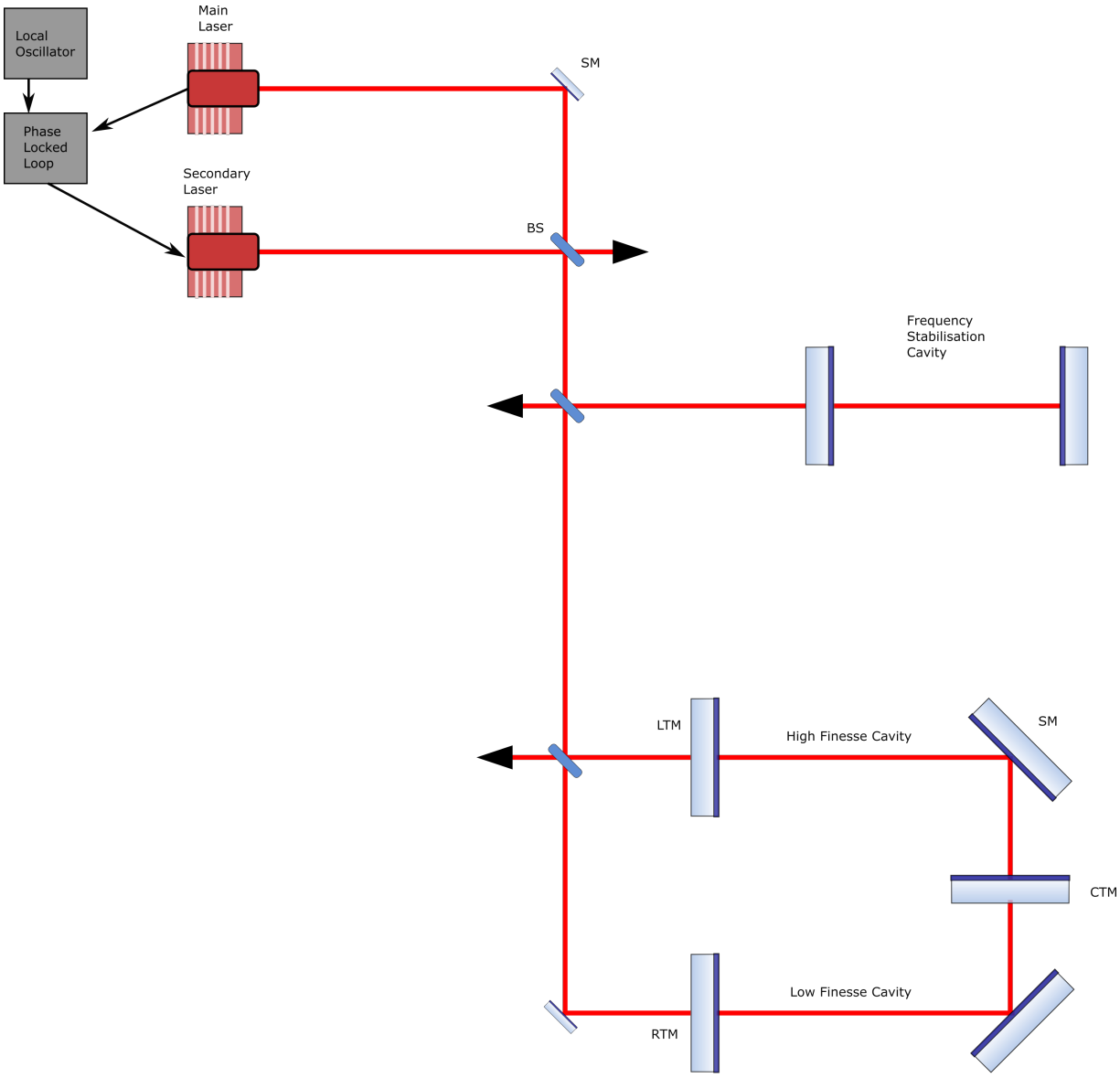

Figure 3.1: Simple layout of the experiment, showing the main laser and the secondary laser which was added to the setup. The frequency stabilisation cavity is also shown, as are the beam-splitters (BS) and the steering mirrors (SM). Finally the two experimental cavities are shown: the high finesse cavity or left-hand cavity consisting of the left-hand test mass (LTM) and central test mass (CTM) and the low finesse cavity or right-hand cavity consisting of the right-hand test mass (RTM) and CTM. The black triangles represent beam dumps.

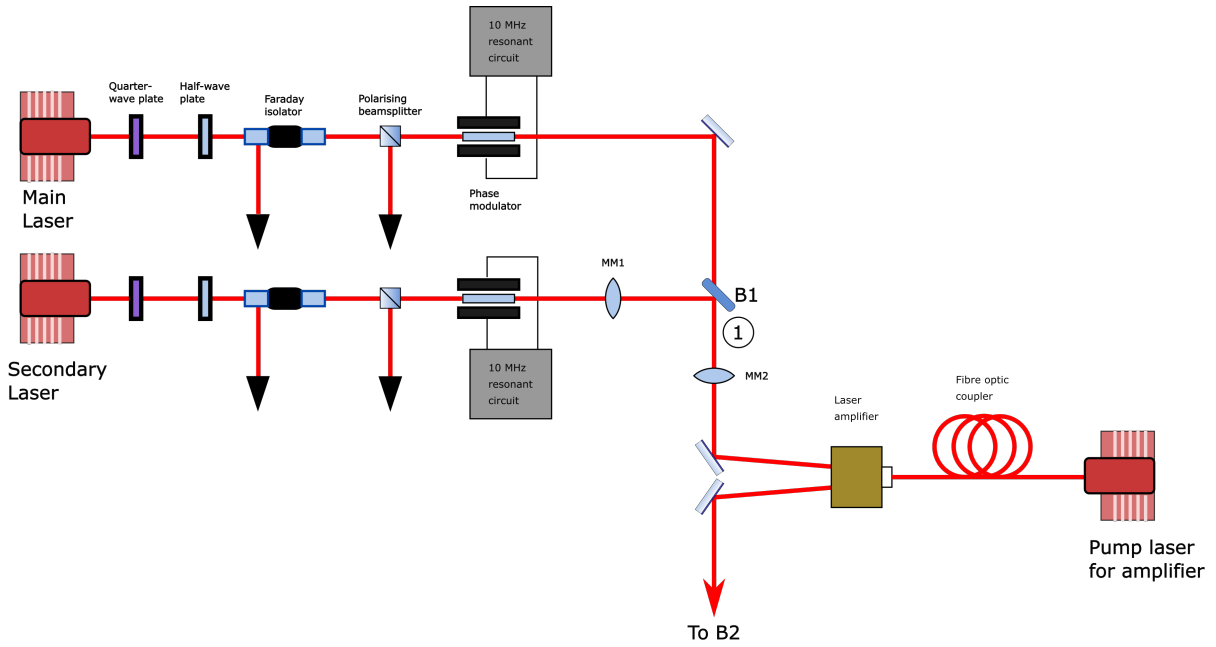

Figure 3.2: Simplified layout of optical table used to prepare the two laser frequencies used in the experiment. B1 is a 50:50 beamsplitter. Point 1 denotes the region in which measurements were carried out of the beam profile of the main and secondary laser frequency at different distances between the lens, MM1, and the laser amplifier.

flections aligned to this second beamsplitter will then be transferred back into the rotator and the orthogonal components will be rejected out to the side of the beamsplitter. The component travelling back through the rotator picks up a further 45° rotation and so will be rejected out to the side of the initial polarising beamsplitter on the laser side of the rotator. A further polarising beamsplitter is set up after the Faraday isolator to get rid of the p-polarisation part of the beam gained by travelling through the rotator. The beam hitting the crystals in the phase modulators will therefore be s-polarised [59].

Each crystal's fast axis is then along the same axis as the polarisation of the corresponding beam. The indexes of refraction are dependent on the voltage applied across the modulator crystals. A modulated field can then be used to create phase modulation of the input beams, and since the voltage is supplied through a resonant circuit, the modulation supplied to each modulator is at this frequency [61]. After modulation the secondary laser beam is passed through a lens MM1 and then combined with the main laser beam. Some light is lost at B1 where the beams are combined but this happens before the light is amplified up at the laser amplifier which compensates

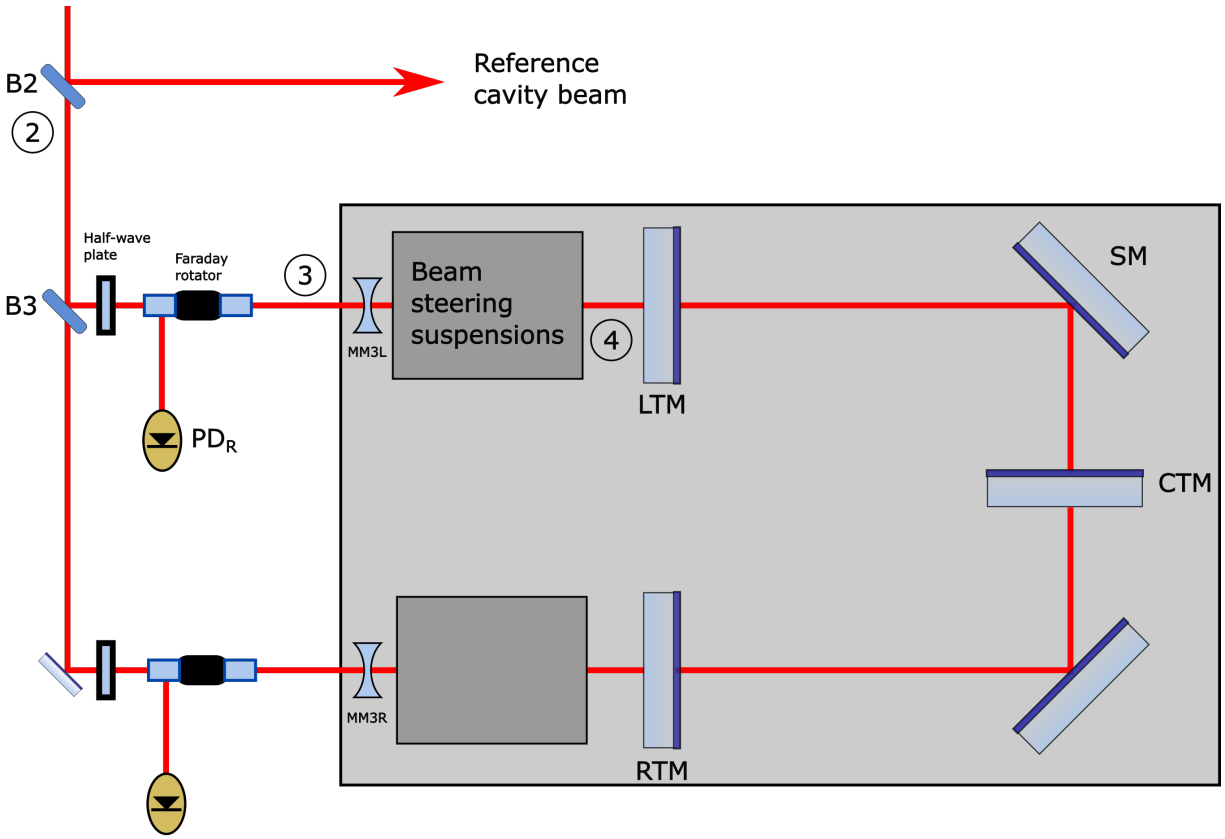

Figure 3.3: Simplified layout of cavities in vacuum system and how they connect to the input optics used to prepare the two laser frequencies used in the experiment. The half-wave plates are used to orient the beam polarisation vectors with the Faraday isolators. The Faraday isolators are used to reflect the beam coming back from the LTM or RTM to their respective photodiodes which is then used to produce an error signal for the cavity lengths. MM3L and MM3R are mode-matching lenses in vacuum before the two experimental cavities, but are not suspended unlike the other optics in vacuum. B2 is a 50:50 beamsplitter and B3 is a 90:10 beamsplitter.

for the loss. The combined beam is passed through the lens MM2, then passed through the laser amplifier. After the amplifier the frequency reference beam is split off at the 50:50 beamsplitter, B2, and the remaining light is split into two beams after this point at B3. This beamsplitter is 90:10 to ensure more power goes into the left-hand cavity which will be used to create the springs used in the experiment. All three beams hit two sets of mirrors on a periscope situated on the edge of the optical bench which directs each beam into the vacuum system, represented as the grey rectangle in Figure 3.3. The frequency reference beam light is reflected into the frequency reference cavity as shown by the arrow, and the rest transmits further down the beam tube hitting lenses MM3L and MM3R, which are isolated from ground motion by passive seismic isolation but not suspended. These lenses were chosen to give the correct beam waist in the experimental Fabry-Perot cavities [3].

3.1.2 Mode-matching

For the experiments it is necessary to use two different carrier frequencies, in respect of which, a second source laser was used. In adding an additional carrier to the system, measurements were carried out of the beam profile of the main and secondary laser frequency at different distances between the lens MM2, and the laser amplifier. This happened at point 1 in Figure 3.2, with each laser on in turn in order to determine the beam waist, w_0, of each laser beam separately. Additional lenses were then added, denoted by MM1 in order to mode-match the secondary laser beam to the main beam, as the main laser was mode-matched during the set-up of the previous optical spring experiments in the lab, when MM2, MM3L and MM3R were installed [3]. These last two lenses are shown in relation to the vacuum system in Figure 3.3. An upper limit could be put on the mode-matching of the primary laser by examination of a time domain sweep of the cavity error signal. Comparison of the relative sizes of the fundamental mode fringe with that due to the second order mode fringe suggests that only 0.91% of the fundamental mode power is lost due to mode-mismatch. Further, the ratio between the first order mode fringe and the fundamental suggests only 0.4% of the fundamental mode power is lost to cavity mis-alignment. This second ratio is not expected to change much between measurement days as the cavity visibility was checked before measurements and re-aligned if necessary.

3.1.3 Frequency Reference Cavity

In preparing the experiment, it was recognised that a limiting factor in previous optical spring measurements had been the large level of frequency noise, and the large size of noise injections needed to get a good gain measurement of the system, meant that some noise was added to the system, masking the spring effects being measured [3]. The current experiment combined previous techniques used in previous optical spring work in the same lab, for frequency stabilisation of the main laser [3, 54]. For this, an external reference for frequency was necessary. In the same vacuum tank in which light is injected from the optical table into the vacuum system, there is a 10 cm Fabry-Perot cavity that is utilised for this purpose, for further details of the setup of this see [62]. The basic optical layout of the system is shown in Figure 3.4. The error signal

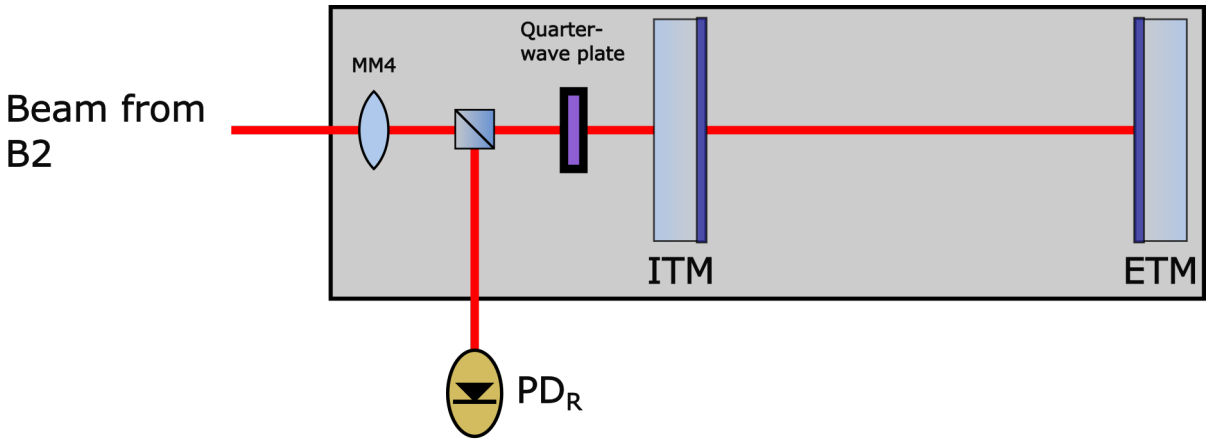

Figure 3.4: Image of the basic optical setup of the frequency reference cavity used for the experiment. Light supplied to this cavity is split off on the optical bench at B2 and is injected into the system from the same periscope as the two main experimental beams. There are several suspended optics used to steer it into the 10 cm cavity. A simplified layout, neglecting beam steering is shown here. One of these optics is a lens, denoted MM4 in the diagram, and used to mode-match the beam into the cavity. There is then a polarising beamsplitter and quarter waveplate, which ensure that light travelling towards the cavity passes straight through the beamsplitter, and light reflected from the cavity is reflected by the beamsplitter out through another viewport and onto a photodiode.

used to keep the laser following the cavity frequency is obtained from the reflected power from the cavity as read out on the photodiode shown. The use of this signal for control of the laser frequency is discussed more fully in Section 3.3.2. Although the optics used for this laser stabilisation cavity are multi-stage suspension systems, their structure is not relevant to the results of this experiment and so will not be discussed in this work, but is detailed in [62]. What is of

relevance is the structure of the multi-stage suspension systems used for the main cavities and so a brief description of the different types used will be given in the following section.

3.2 Suspensions

A similar suspension design was used for all the mirrors needed to direct the left-hand cavity and right-hand cavity beams and to create the 10 m Fabry-Perot cavities. The only difference was the weight of the folding mirrors was required to be three times larger to ensure the reduced mass is mainly dependent on the input and end mirrors, and thus the radiation pressure dynamics of the system is not altered by these folding mirrors. As the suspensions have slight differences in alignment or manufacture of components, each has slightly different resonant modes that can be driven by electronic noise from experimental measurements. More details are given on the suspensions and their actuators in the following sections.

3.2.1 Cavity Mirrors

The three main experiment mirror suspensions were all designed and built as part of previous optical spring work experiments [3] and a simplified design is shown in Figure 3.5. The two input mirrors for the main cavities in the system, the LTM and RTM are both 2.54 cm in diameter and weigh 100 g including the optic holder they sit in. The mirrors both have a radius of curvature of 15 m. The CTM has the same radius and mass but a flat front surface. It consists of two mirrors back to back on the same suspension so each cavity has the highly reflective side of each mirror as its end mirror, with an intentional wedge between the front and back surfaces to avoid light coupling between the two cavities [3]. The suspension design consists of two main stages; the first is the passive isolation stacks under the breadboard and the second is the mirror suspension which sits on the breadboard. The first stage consists of three stages of 'passive' isolation made of two layers of rubber between metal plates under the breadboard, and one layer of rubber between the top and sides of the suspension support structure which sits on the breadboard. The mirror then hangs from this support structure in a double pendulum configuration, which reduces the amplitude of noise transmitted between the breadboard and the mirror by a factor of $\frac{1}{f^4}$ above

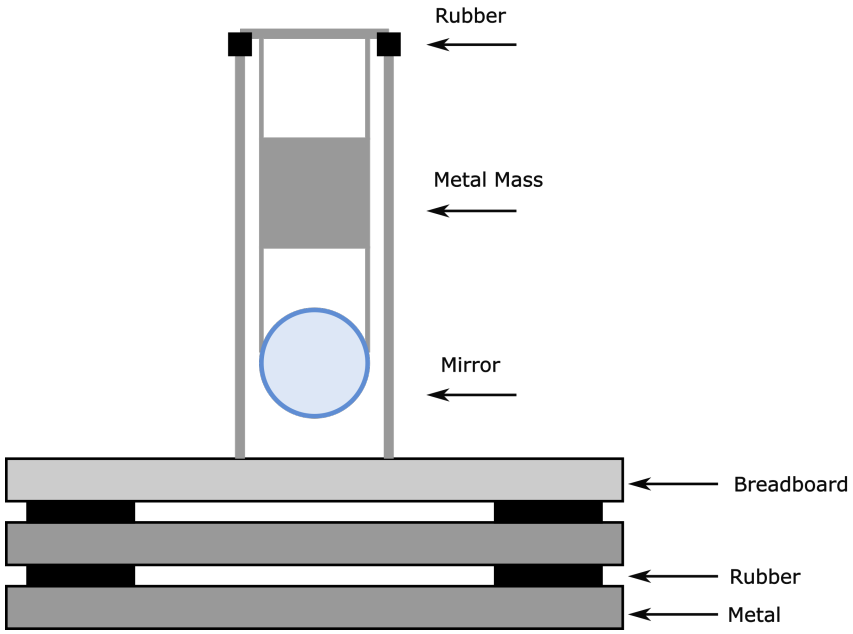

Figure 3.5: Simplified front view of a generic mirror suspension structure made for the two main experimental cavities. There are two stages of rubber passive isolation which a breadboard rests on, then another layer of rubber between the suspension support structure that attaches to the breadboard and the top part of it that the suspension wires attach to. Hanging off the top four suspension wires is the top metal mass which is where the eddy current damper magnets are attached. There are copper cups on the suspension support structure behind this metal mass, which the magnets move in, to provide the damping force. The mirror then hangs off this metal mass from a second set of metal wires. Each breadboard can fit three of these suspensions, further details of the actuation of the specific suspensions are detailed in Section 3.2.2.

the resonant frequency of the suspension, around 0.7 Hz. This occurs as each suspension stage provides $\frac{1}{f^2}$ attenuation of ground motion above the fundamental frequency. The top level of this suspension use 'eddy-current dampers' which involve magnets on the back of the mass moving in copper cups attached to the metal support structure, creating a magnetic force which damps the motion of the pendulum resonances [3, 63].

3.2.2 Actuation of Mirrors

To allow adjustment of the pitch and yaw of each suspension mirror, there is a coil of wire around each damper 'cup'. A current applied to these coils is then used to control the angle of the double pendulum with respect to the metal support structure. A second set of 'coil-magnet actuators' is used on the bottom stage to control the longitudinal position of the mirror. The actuation of these coils was designed to be 44 mN/A for each coil-magnet actuator pair, where there are four actuators per mass [3], see Figure 3.6. This strength depends on the distance between the coils,

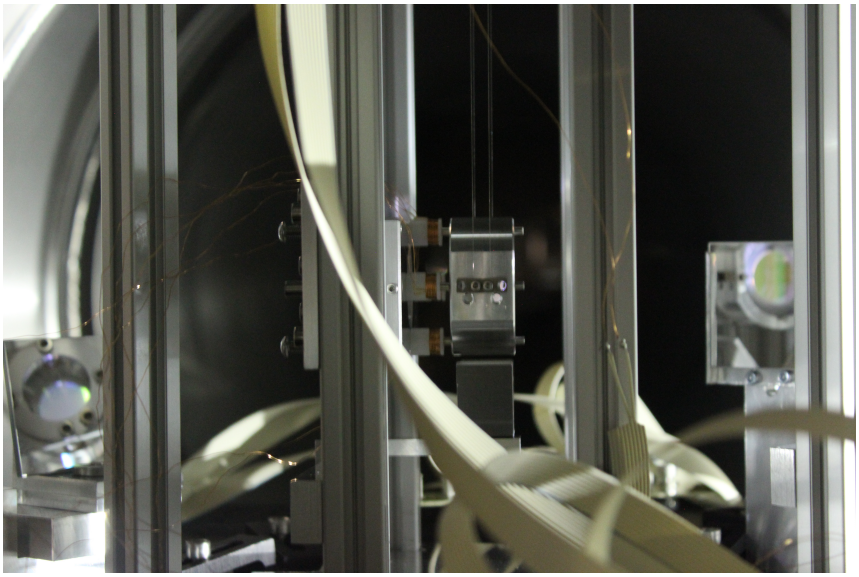

Figure 3.6: Photo of CTM mass, view is side on showing coil magnet actuators. Photo is courtesy of Dr. Briggs.

mounted on a support structure, and the magnets, stuck to the back of the mirror, and so it varies between different suspensions as it depends on small differences in each suspension structure, unavoidable during setup.

3.3 Control Systems

Control systems for the various subsystems in the experiment were designed taking into account the noise requirements of the measurements, and the various structural resonances of the suspensions and seismic isolation that required active damping. The three optical cavities in the experiment all used the same basic method of length sensing in their control loops.

3.3.1 Pound-Drever Hall Feedback

The technique used to control the cavity length is called Pound-Drever-Hall feedback, as mentioned previously in Section 1.3.5. The cavity is held on the centre of resonance, that is when the circulating power is maximum and the reflected signal is at a minimum. The reflected signal from the cavity is put into a mixer in order to beat it with a local oscillator frequency reference, this is a 10 MHz signal for all three cavities. The output from the mixer is then filtered to remove beats 20 MHz and above. The resulting signal is proportional to the derivative of the cavity circulating power, and thus indicates the tuning of the cavity with respect to its resonance with the zero point being halfway up the error signal.

3.3.2 Laser Stabilisation

The laser frequency stabilisation, as mentioned above, uses a resonant cavity as a frequency reference. The laser follows the frequency of the cavity using a feedback signal derived from the Pound-Drever-Hall error signal for this cavity. Shaped feedback derived from this error signal is then applied to a piezo-electric transducer (PZT), which expands and contracts in response to a voltage and is used to modulate the laser crystal shape. The action of the PZT alters the laser resonant frequency to match that of the cavity. The cavity can be knocked out of lock by low frequency noise in range of the main suspension modes, so the cavity is held steady at very low frequencies by feedback to the mirror actuation coils on one of the cavity mirrors. The control system of the laser is represented in Figure 3.7 as a block diagram. The length actuation of the laser stabilisation cavity mirror occurs in H_M, where the output signal from the analogue servo electronics is filtered digitally then sent to an analogue coil driver circuit which supplies a current

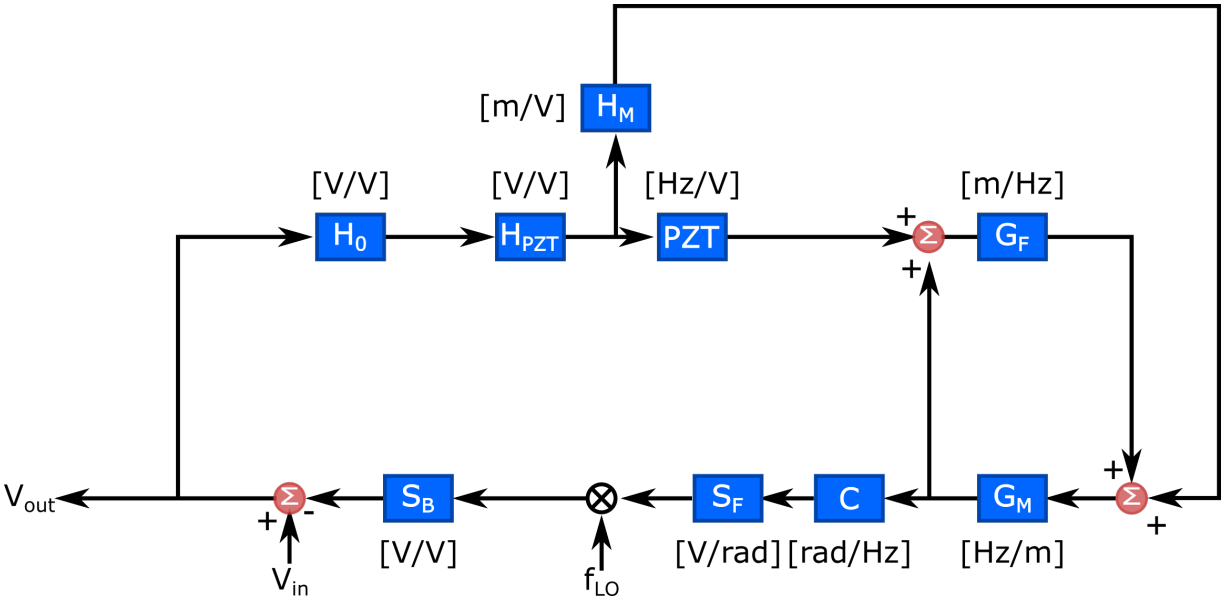

Figure 3.7: Diagram of the layout of the main laser frequency control system. H_M is the feedback block for the length actuation of the laser stabilisation cavity mirror, consisting of feedback shaping filters, coil driver circuit, coil-magnet actuator and mirror suspension. This feedback to the cavity length is designed to work below 19 Hz. H_0 is the first part of the laser feedback circuit which does the common filter shaping. H_{PZT} is the shaping applied to the PZT feedback signal. PZT is the response of the laser PZT as a signal is applied and of the laser frequency as the crystal is squeezed by the PZT. G_F is the response of the laser stabilisation cavity length as the frequency of the laser changes. G_M is the response of the frequency of the laser stabilisation cavity as the cavity length is changed. S_F is the sensing response function of the high frequency photodiode as the frequency of the cavity output changes. S_B is the filtering on demodulated signal signal out of the mixer, in order to remove higher frequency beats and obtain the loop error signal for the laser frequency stabilisation. f_{LO} is the local oscillator frequency, V_{in} is the injection to the frequency control loop used for characterisation of the noise suppression, and V_{out} is the output measurement for the loop.

to a coil-magnet actuator on the back of one the laser stabilisation cavity mirrors, which drives the mirror suspension. This feedback to the cavity length is designed to work below 19 Hz and is combined with G_F, the cavity motion from the laser changing frequency, at the summing point in the bottom right corner of the diagram. The cavity frequency changes in response to this motion with G_M, and this frequency change is sensed by the phase change in the reflected signal from the cavity, C, which is measured on the high frequency photodiode, S_F. This signal is mixed with the local oscillator, f_{LO}, and the demodulated signal is filtered by S_B to remove higher order beats and leave a signal denoting the phase difference between the laser and the local oscillator. The feedback signal is then fed into the analogue electronics blocks, H_0 and H_{PZT}, before being applied across the PZT that squeezes the main laser crystal and changes its frequency. This frequency change is combined with the frequency change from the cavity length feedback at the top summing point in the diagram, and the length change it produces in the cavity, G_F dominates over the length change caused by the cavity length feedback at higher frequencies.

This means that there is no suppression in low frequency noise of the laser, but the cross-over between feedback to the cavity and feedback to the laser is designed to be at 19 Hz, below the measurement range of the experiment, and therefore below the range in which low frequency noise is necessary. The filter design for the feedback to the cavity length is shown in Figure 3.8. By 80 Hz, the start of the experimental measurement range, the length feedback gain is 0.043 and therefore the feedback to the laser, will have increased by a factor of $\frac{1}{G_M H_M} = 23$ relative to the gain of the laser stabilisation loop at the cross-over point.

An open loop transfer function of the laser stabilisation loop is shown in Figure 3.9. The unsuppressed laser noise from the laser manufacturer is $100\,\frac{\mathrm{Hz}}{\sqrt{\mathrm{Hz}}}$ at 100 Hz and falls to $10\,\frac{\mathrm{Hz}}{\sqrt{\mathrm{Hz}}}$ at 1 kHz [64]. The green line in Figure 3.9 represents a measurement of the open loop noise carried out by injecting a signal into the error point with a signal analyser. Due to higher noise below 1 kHz, the measurement below this point was not of sufficient resolution, and so the shaping of the loop shown in orange, is that derived from an injection through the electronics of the laser servo on its own. The laser PZT, high frequency photodiode and laser stabilisation cavity, will

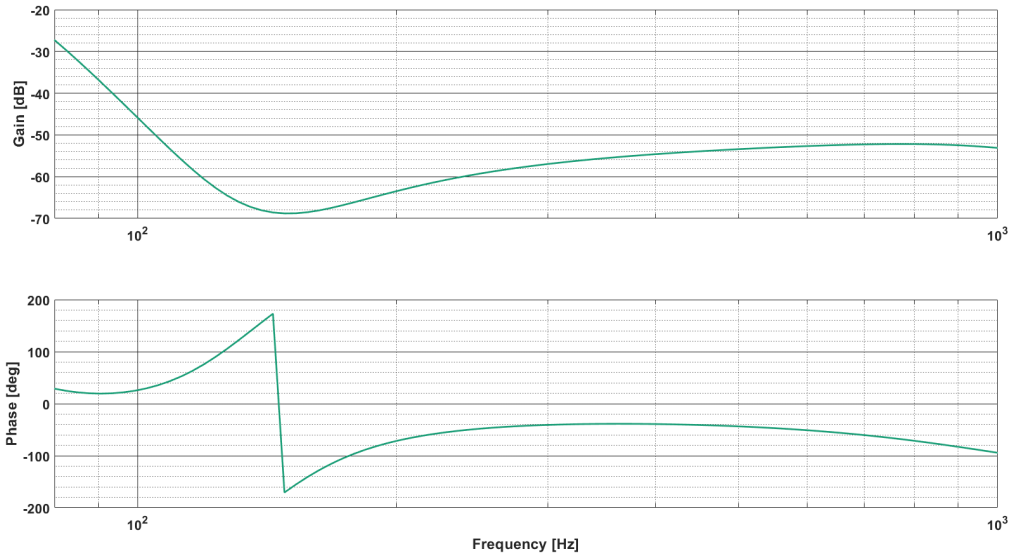

Figure 3.8: Design of low frequency filter for feedback to the laser stabilisation cavity, shown as a magnitude and phase plot across the frequency range of the measurements that will be carried out on the main experimental cavities.

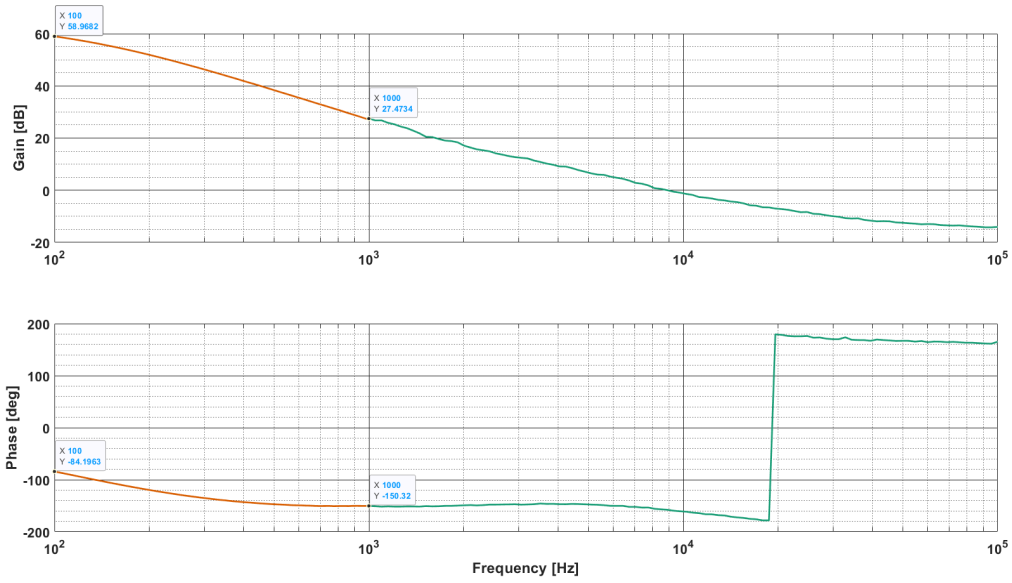

Figure 3.9: Open loop transfer function of laser stabilisation system, with gain altered to reflect the 9 kHz unity gain point measured during the spring calibration measurements. The shaping and phase behaviour of the orange line is taken from a measurement of the control electronics, whereas the shaping and phase of the green line is taken from a whole loop measurement of the frequency stabilisation loop above 1 kHz.

have corner frequencies well above 1 kHz and therefore will provide no frequency shaping below 1 kHz [62,65]. The gain through the electronics was scaled in magnitude and phase to be contiguous with the measurement at 1 kHz. Then the full transfer function from 100 Hz to 100 kHz was scaled up in gain to give a unity gain point of 9 kHz, which was its nominal value throughout the main optical spring measurements. Thus the laser noise will have been suppressed to 0.11 $\frac{\text{Hz}}{\sqrt{\text{Hz}}}$ at 100 Hz and 0.42 $\frac{\text{Hz}}{\sqrt{\text{Hz}}}$ at 1 kHz. This allows the measurement noise injections to be seen well above the noise floor. It is also necessary to check the shot noise of the frequency stabilisation cavity as this could affect the frequency noise seen in both main cavities. It is taken from the calculation in [62] and is equivalent to $5\times10^{-19}\,\text{m}/\sqrt{\text{Hz}}$ between 80 Hz and 1 kHz. Thus the shot noise of the frequency stabilisation cavity will not limit the total noise of either cavity.

3.3.3 Phase Locking of Secondary Laser

In order to create two distinct optomechanical systems in the left-hand cavity, it is important to make sure the secondary laser is at a different frequency from the main laser that is also not a multiple of the free spectra range with respect to the main laser. If this is not the case the two fields will add constructively and so will not be independently controllable with respect to the cavity frequency. Both lasers must also have a fixed frequency, otherwise the frequencies of the lasers can drift into and out of resonance with respect to each other as the temperature changes in the laboratory. The main laser has a fixed frequency by locking it to the frequency stabilisation cavity. To control the frequency of the second laser we can use the stabilised main laser as a reference, and use feedback to the laser crystal PZT and crystal temperature of the second laser to lock it at a set frequency relative to the main laser [64]. For initial locking of the control loop and for measurements where the secondary laser detuning was not necessary, the local oscillator was set to 94 MHz. For detuned measurements, a local oscillator near to 90 MHz was used, which is close to six free spectral ranges of the cavity. A simple layout of the loop is shown in Figure 3.10. The system must be locked manually when the beat between between the laser drifts close to the intended LO frequency, this is because there are peaks at other frequencies in the spectrum that the main laser secondary beat could lock to. The relative position in frequency space of the main laser-secondary laser beat and the local oscillator peak

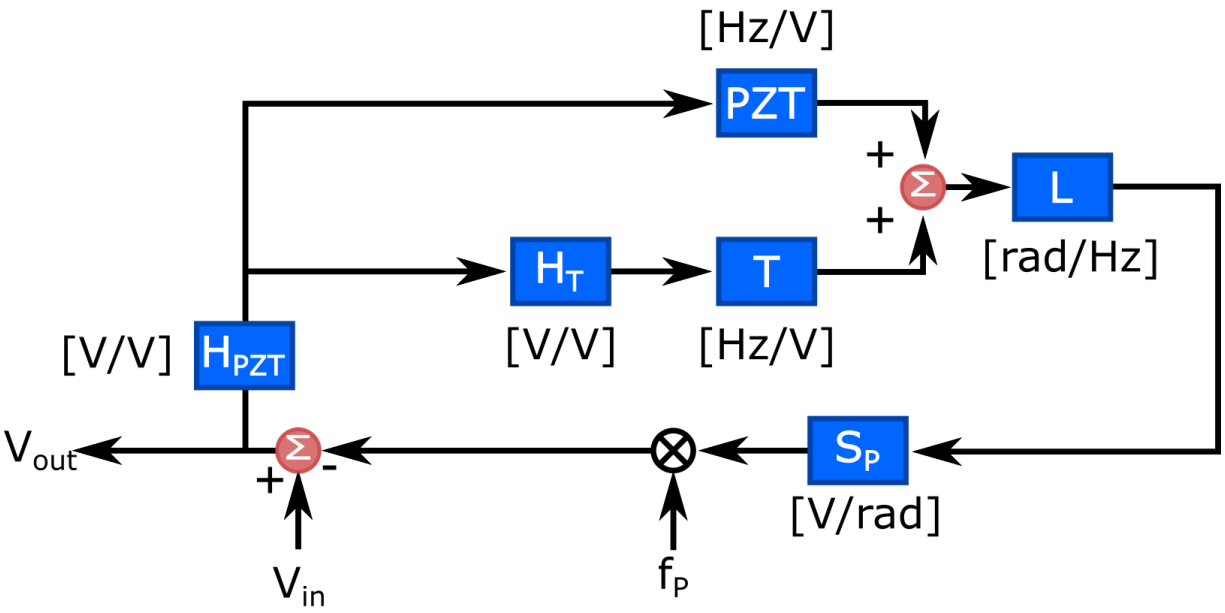

Figure 3.10: Diagram of the layout of the secondary laser frequency control system. H_{PZT} is the main feedback shaping, the output of which is applied to the PZT. PZT is the response of the laser frequency as the crystal is squeezed by the PZT. H_T is the shaping applied to the feedback signal to feedback to the laser temperature at low frequency. T is the response of the laser frequency as a signal is applied to the temperature control of the laser. L is the phase response of the laser as the frequency is changed. S_P is the sensing response function of the high frequency photodiode as the phase of the incident light changes. f_p is the local oscillator frequency that sets the relative frequency of the two lasers, V_{in} is the injection to the frequency control loop used for characterisation of the noise suppression, and V_{out} is the output signal from the loop.

is monitored using a pick-off of the error signal before it goes into the mixer. The locking signal needs to have the correct sign to lock to the main laser-secondary laser beat, and so must start out on the correct side of the beat so the feedback drives it towards the LO in frequency. If the laser temperature feedback is switched on at the wrong point, it will apply a large static offset to the laser frequency. The laser will then be driven further away from the locking point. It is therefore necessary to iteratively tune an offset on the feedback to the temperature of the secondary laser, in order to ensure the beat approaches the LO peak from the correct direction and that the two are close in frequency before either form of feedback is switched on. The control system was designed iteratively and a final transfer function of the PZT feedback control filters is shown below in Figure 3.11. At lower frequencies, temperature feedback is used to keep the secondary laser locked to the first. The bandwidth of this feedback is 1 Hz [65], and so does not affect the noise performance in the range our measurements are concerned with, which is above 80 Hz. A measurement of the full transfer function of the system is shown in Figure 3.12. The gain around 1 kHz, the intended unity gain point of the main cavities, is over 60 dB, which is higher than the gain of the laser stabilisation servo. It can be inferred that the gain of the phase-locked loop (or PLL) will increase to over 70 dB at 100 Hz, as the gain of the PZT feedback electronics in Figure 3.11 is more than 13 dB higher at 100 Hz than 1 kHz. As the phase-locked laser control loop has higher gain than the main laser control loop in the frequency range from 100 Hz to 1 kHz, the conclusion that can be drawn is that the noise of the main laser will therefore dominate the secondary laser noise performance over this range.

3.3.4 Control of 10 m Cavities

The beam from the main laser is modulated using a 10 MHz source which is used to lock both 10 m experimental cavities using the method described in Section 1.3.5. The control signal is derived by filtering the Pound-Drever-Hall error signal through customised digital filters. This system allows easy switching of filters during the experiment, controllable through customisable control screens made in a program called medm [66]. These control screens produce scripts that direct data input and output to and from the experiment. An example of one of the filter control screens is shown in Figure 3.13. The system also contains anti-aliasing filters on the input before

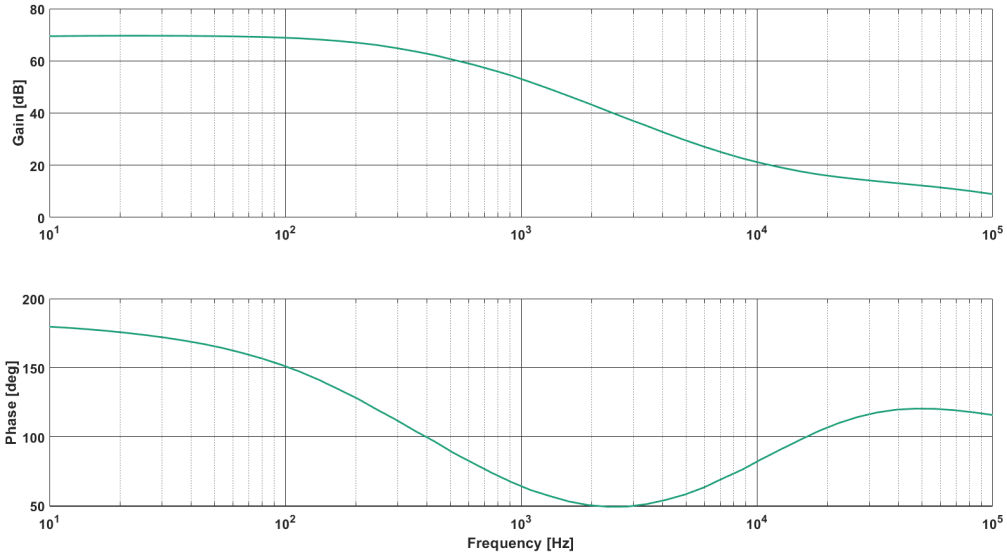

Figure 3.11: The gain of the PLL electronics in block H_{PZT} is shown. They consist of a transitional low pass filter between 200 Hz and 8 kHz, a single pole filter at 700 Hz and another at 70 kHz. These were designed to control the PZT feedback to the second laser, a control signal from the output of these electronics is also sent into the digital control system and filtered in order to provide temperature control to the laser diode at frequencies of 1 Hz and below.

the analogue to digital conversion, and anti-imaging filters after the digital to analogue conversion on the output [3, 67]. Both these filters ensure no frequency artefacts appear in the control signal from either of the conversion processes [3, 68].

The cavity locking scheme was adapted from that designed in [3]. User set limits are utilised to turn the feedback on and off when the cavity reflected power reaches a certain level. This is known as 'triggering' through the remainder of this chapter, see Figure 3.14. Triggering is necessary as the length feedback has a high gain, and so will accelerate the mirror far from the resonance point if the locking is on constantly while the lock is obtained. A simplified layout of the control loop is shown in Figure 3.15. The block H_R actually consists of two stages of filtering. The first of these, shown in Figure 3.16 in blue is switched on as soon as the feedback triggers. Stage two changes the servo gain as in the red graph also in Figure 3.16, and is ramped slowly in after a specific time delay to damp the motion of the mirrors while the cavity is locked. This process is necessary because even at lower finesse there is still considerable radiation pressure on the mirrors. When locked with both filter stages, the cavity has the open loop transfer function

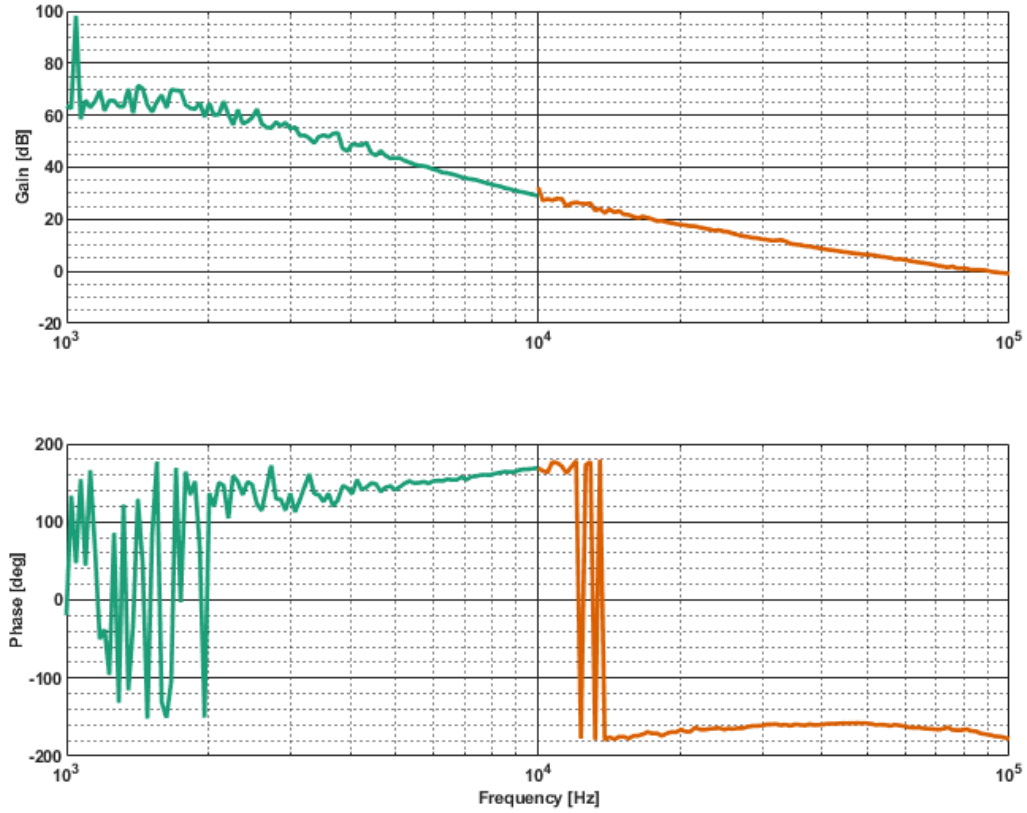

Figure 3.12: Measurement of the open loop transfer function of the phase-locked laser control servo. The low frequency and high frequency parts are shown in different colours as these were separate measurements due to the range limitations of the measurement device. The unity gain point is at 89.03 MHz and it can be seen that the gain around 1 kHz, the intended unity gain point of the main cavities, is over 50 dB.

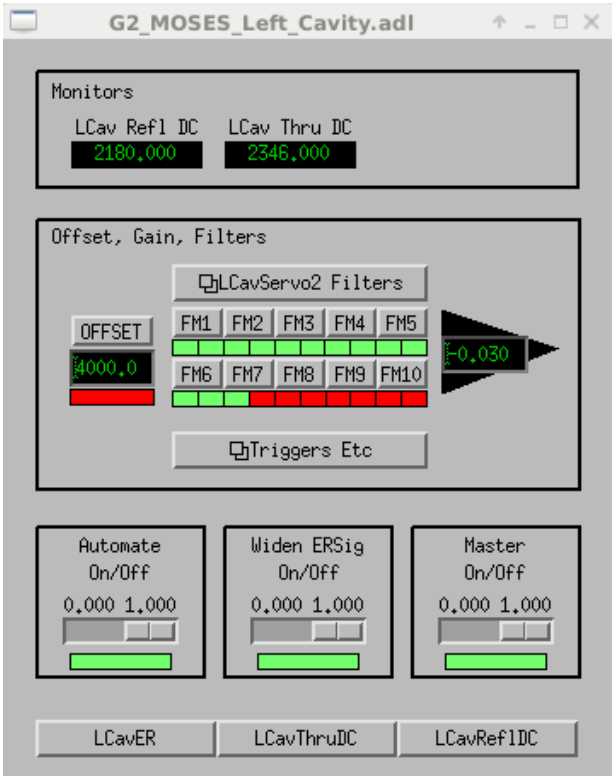

Figure 3.13: Control screen showing readouts of the input and output values for the main left-hand cavity control filter block, as well as entry boxes for gain and offset values that can be set by the user, and filter blocks that are preset and then controlled automatically by the user model when the locking system is switched on at the master switch.

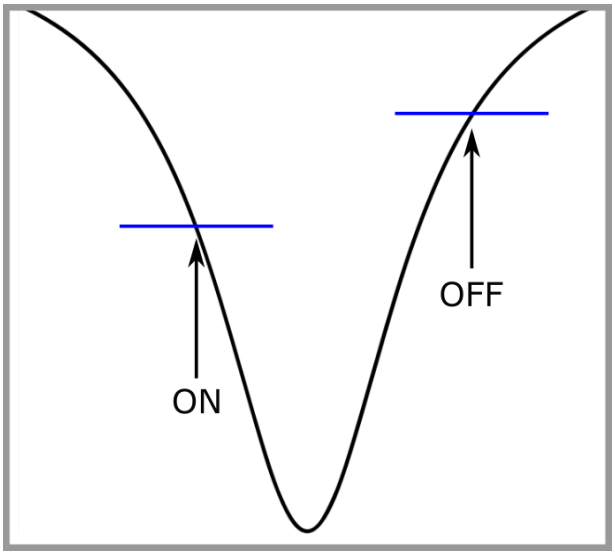

Figure 3.14: Diagram showing the shape of the cavity fringe on the transmitted light signal measured from the cavity. The x-axis is frequency and the y is voltage. The locking comes on when the cavity transmitted signal passes through the point indicated at ON and switches off when the cavity passes through the point labelled OFF.

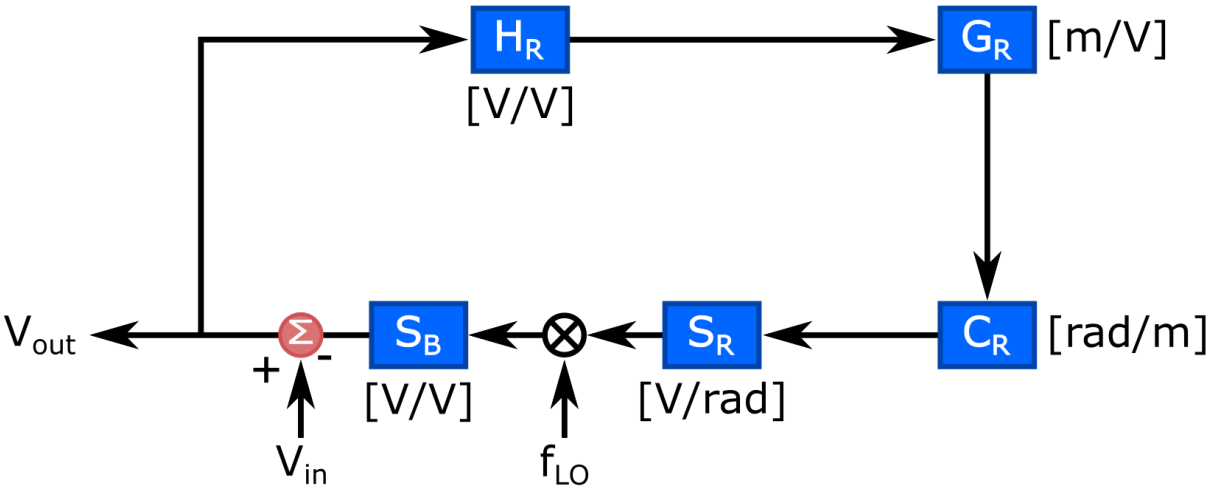

Figure 3.15: Diagram of the layout of the sensing (right-hand) cavity length control system. H_R is the feedback shaping block for the length actuation of the right-hand cavity input mirror, the RTM. This consists of feedback shaping filters as described in Figure 3.16. Included in the control system are also filters used for ADC and DAC. G_R is the response function from the input to the circuit which drives the motion of the RTM, to the motion of the mirror itself in the longitudinal direction. C_R is the phase response of the right-hand cavity as the cavity length is changed. S_R is the sensing response function of the high frequency photodiode as the phase of the cavity output changes. S_B is the filtering on the demodulated signal signal out of the mixer, in order to remove higher frequency beats and obtain the loop error signal for the laser frequency stabilisation. f_{LO} is the local oscillator frequency, V_{in} is the injection to the sensing cavity control loop used for characterisation of the cavity, and V_{out} is the output measurement for the loop characterisation.

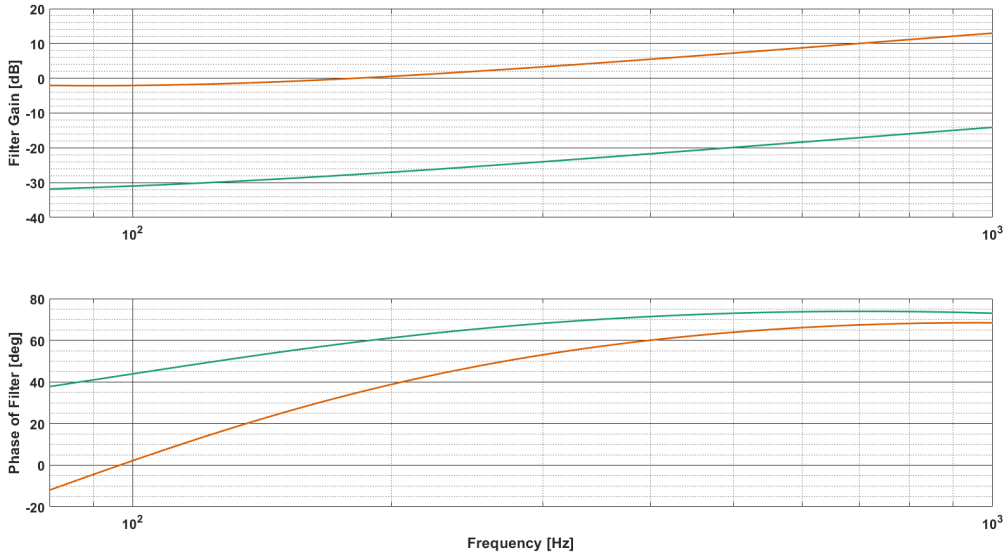

Figure 3.16: This figure shows the response function of the digital servo stages for locking the right-hand cavity. Stage 1 shown in blue is used to slow down the mirror and lock it. The red graph shows the combined response of stages 1 and 2. Stage 2 provides more gain at low frequencies to suppress low frequency motion of the mirror, in addition to providing more gain over the measurement frequency range. The open loop gain for this cavity can be calculated by multiplying these control filters and the suspension transfer function.

shown in Figure 3.17.

The cavity control contains several narrow-band filters used in the cavity locking. These are not shown, and do not alter the filter behaviour in the measurement range from 80 Hz to 1 kHz. The first group of these are all below 60 Hz and are used to provide resonant gain in a narrowband around the air conditioning and mechanical suspension resonances. These resonances would otherwise not be damped sufficiently to allow the mirror to be held in place by the control system. There is one above the unity gain point of the cavity, centred at 3 kHz, which is designed to give extra phase lead at the unity gain point, expected to be at 1 kHz. There is also a notch filter in the control system at 7050 Hz to remove a mode of the optic holder on the LTM suspension. Finally, after the digital feedback signal leaves the digital system where an analogue filter multiplies the feedback signal by $\times 10$ and adds an additional single pole filter at 10 kHz. After this, the feedback signal is sent to a circuit which drives a current through the mirror actuators. This was put in after initial locking of the right-hand cavity to boost its control signal, compensating for the

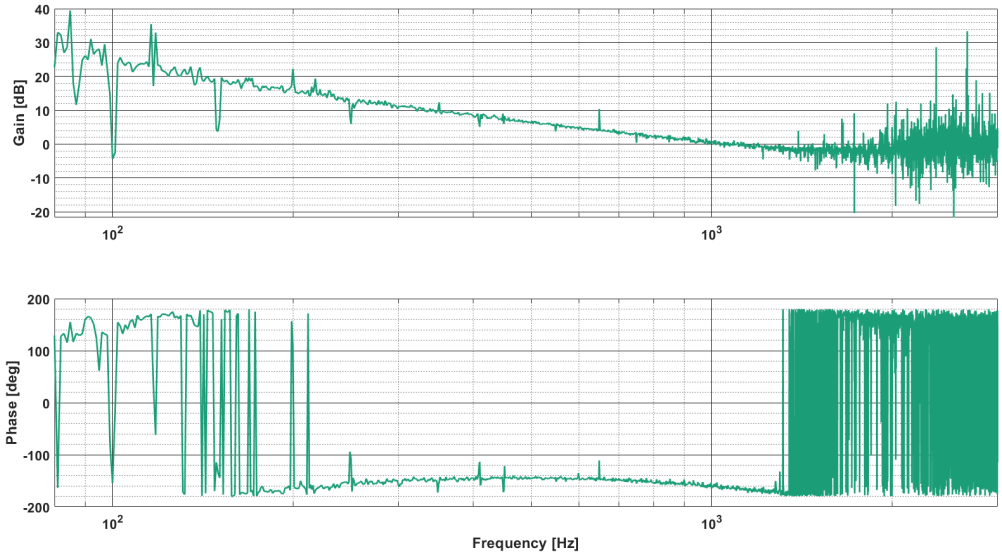

Figure 3.17: Measurement of the open loop transfer function of the right-hand cavity used for sensing the dynamics of the spring cavity. Unity gain is at 1 kHz.

difference in error signal amplitude in the two cavities caused by the much higher input power to the left-hand cavity.

Both cavities have a control system like the one given above, apart from differences which will be described below. The right-hand of the two 10 m cavities is used to carry out the 'local readout' of the optical springs, for more detail on this experimental method, see Section 4.2.6. To avoid the chance of any significant optomechanical springs in this cavity, the finesse and therefore circulating power is set to a low value. Since the original design of the cavity was to be high finesse $\mathcal{F} =$ 10000 [3] for s-polarised input light, the polarisation of the incoming light was set to be p-polarisation, for which the cavity folding mirrors have a lower transmission. This gives $\mathcal{F} = 780$ for the sensing cavity. As the left-hand cavity is a much higher finesse, its noise performance needs to be better than the right-hand cavity and this requires a slightly more complex control scheme.

3.3.5 Control of Spring Cavity

The high finesse cavity rings when passing through resonance and this imparts an impulse to the mirror, making it hard to catch lock using the conventional Pound-Drever-Hall error signal

before the mirror travels right through the part of the signal that can be used for locking. Thus a technique was developed in [3], to extend the distance from resonance at which the control system can lock the mass. To do this, the linear range of the error signal, at the centre of the upper graph shown in Figure 3.18, must be extended so it covers a broader range in cavity tuning. The PDH error signal from the cavity is divided by a signal derived from the measured amplitude of the cavity transmitted power, to get this so called 'widened' signal. This produces an error signal of the form in the lower graph in Figure 3.18, a formula for which is shown in appendix A as Equation (A.54).

Since the slope of this error signal controls the V/Hz value used to derive the feedback signal

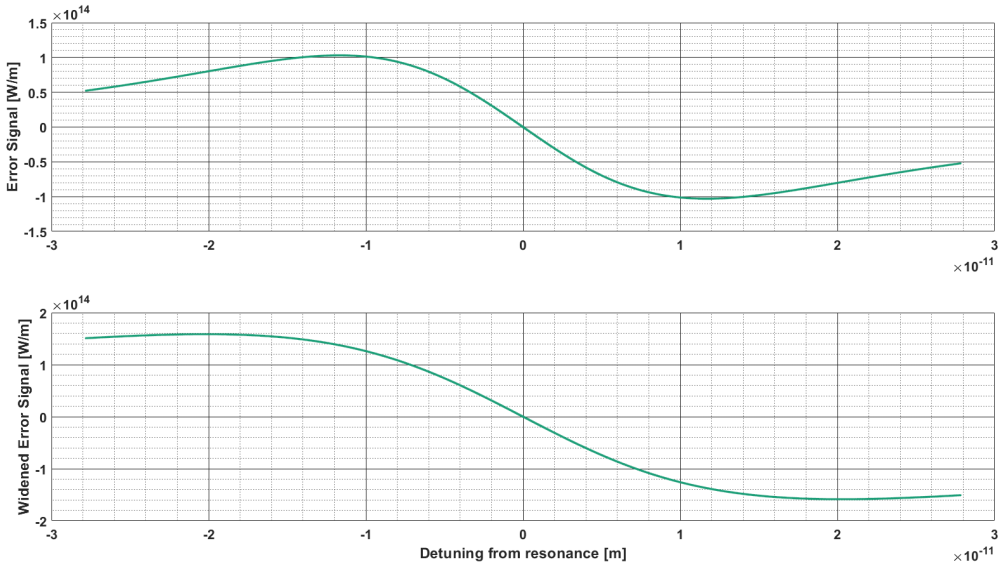

Figure 3.18: The top image shows a calculated signal proportional to the normal Pound-Drever-Hall signal for the 10 m cavity, that is, the differential of the cavity circulating power with respect to detuning of the cavity from the resonance position. The bottom image is proportional to the widened error signal, where the error signal from the top image was divided by a model for the normalised transmitted power over the same detuning range.

for the cavity, changing the slope, as the widening technique does, will change the magnitude of the gain needed in the servo during locking. As the divisor signal varies in time and frequency, this change can alter the frequency response of the open loop transfer function of the system. Crucially, this will not significantly affect the transfer function when the system is around the resonance point as the transmitted power is flat in frequency, however the transfer function will

be altered in a frequency dependent way, when the system is tuned off resonance. For any measurements carried out while using this widening technique, the normalised transmitted power will need to be taken into account when analysing the open loop gain of the system. This is discussed further in the appendix A. Widening was not used for most of the main set of measurements taken, but was used in one of the measurements presented in Figure 5.11. Note that this widening technique can also be used to lock the right-hand cavity, but was not needed as the cavity was not detuned for our measurements and its lower finesse made it easier to lock. Slight tuning of the overall servo gain magnitude by the operator was used to allow the system to stay locked.

There are additional changes needed in the left-hand cavity loop; these are shown in Figure 3.19. There are three rather than two stages of digital filters. The triggering of the feedback is done in the same way as for the right-hand cavity, then after a time delay stage two filters switch on, then after another time delay the stage three filters turn on.

Like the right-hand cavity, the left-hand cavity contains several narrow-band filters used in the cavity locking. These are not shown in Figure 3.19, but are functionally the same as those discussed above for the right-hand cavity. Again these do not alter the filter behaviour in the measurement range from 80 Hz to 1 kHz.

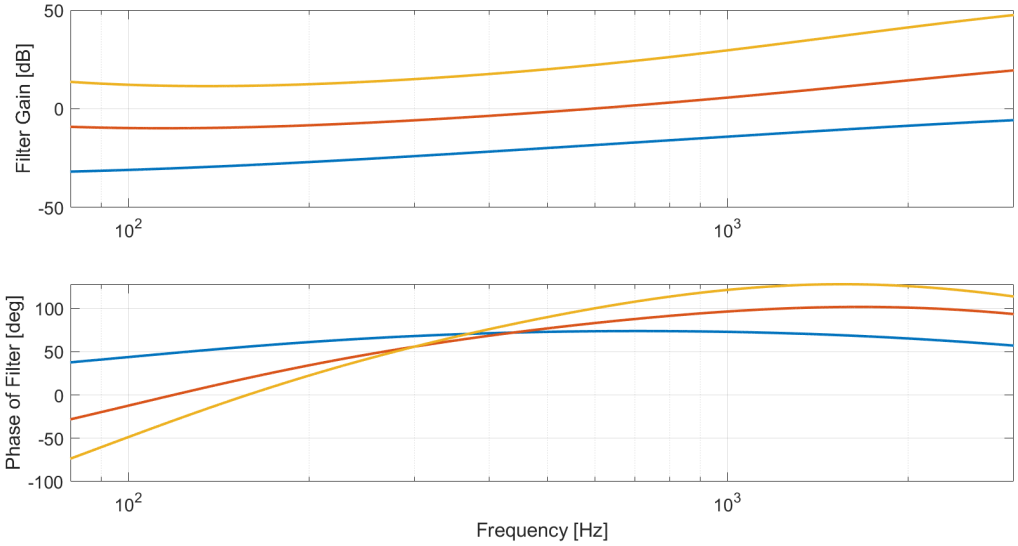

Figure 3.19: Bode plot showing the three stages of wideband servo filters used in the locking servo of the left-hand cavity. The filter at the first stage is shown in green and is the same as that in the right-hand cavity. An extra intermediate stage is added, the orange curve shows the first stage plus three integrators that are added to suppress low frequency motion. The final state of the filtering is shown in purple and includes two more integrators for higher gain at low frequency below the measurement range, and another differentiator to add in gain near the high end of the measurement range around 1 kHz.

Chapter 4

Experimental Methodology

4.1 Cavity Calibration

As was discussed in Chapter 3, the experiment utilises the left-hand cavity to set up the optomechanics and the right-hand cavity to read out the motion of the CTM under the influence of this optomechanical setup. For the purpose of analysing this so-called 'Local Readout' experiment, it is first necessary to get a precise calibration of the spring strengths created in the left-hand cavity. Several simple springs will be created in the left-hand cavity, and the dynamics will be measured by applying a noise injection to the error point of the left-hand cavity length control system, and looking at the induced noise right after the injection point. The resulting transfer function will be verified by comparison to a numerical simulation of the left-hand cavity and its control system.

It is therefore essential to know the precise circulating power level in the two cavities. This is to verify the strength of the spring detunings measured; it is evident from the dependence of the spring constant on circulating power in the cavity from Chapter 2 that power in the cavity strongly affects the spring dynamics. To work out the circulating power level in the left-hand cavity; input power, cavity finesse, the relative size of the modulation sidebands and the cavity visibility need to be measured.

4.1.1 Input Power Levels

The input power to the left-hand cavity was calculated to be $P_4 = 0.767 \pm 0.093$ W, where

$$P_4 = f_3 P_2 f_4 \frac{P_a^r}{\left(P_a^r + P_b^r\right)}. \tag{4.1}$$

The total beam power was measured, at point 2 as marked on Figure 4.1, with a power meter and is denoted P_2. f_3 is the fraction of light at point 3 compared to point 2 as it passes through the beamsplitter, B3, and the half-waveplate. B3 directs 90% of the light to the left-hand cavity. The waveplate is turned to reject half of the input power to the left-hand cavity. There is also some fraction of light lost between the bench and the input mirror to the Fabry-Perot cavity, so only a fraction, f_4 reaches the input mirror LTM. Further, it is necessary to only select the power in the main laser, as it is this frequency that the cavity locks to. The relative DC power levels are measured on the reflected photodiode PD_R, where P_a^r is the power in Laser A when Laser B is blocked, and P_b^r is the same for Laser B. The reflected power in each wavelength P_a^r and P_b^r was measured on the photodiode, PD_R, at point 3 in Figure 4.1 by blocking the output of one laser and reading the DC voltage amplitude off the photodiode when the cavity was not passing through resonance.

To calculate the error on P_4, σ_{P_4}, the equation for an error on a function of multiple measurements,

$$\begin{aligned}\sigma_f^2 = &\left(\sigma_x \frac{\mathrm{d}}{\mathrm{d}x}\Big(f(x, y, z, \ldots, n)\Big)\right)^2 + \left(\sigma_y \frac{\mathrm{d}}{\mathrm{d}y}\Big(f(x, y, z, \ldots, n)\Big)\right)^2 \\ &+ \left(\sigma_z \frac{\mathrm{d}}{\mathrm{d}z}\Big(f(x, y, z, \ldots, n)\Big)\right)^2 + \ldots + \left(\sigma_n \frac{\mathrm{d}}{\mathrm{d}n}\Big(f(x, y, z, \ldots, n)\Big)\right)^2\end{aligned} \tag{4.2}$$

from [69] was used. Where $f(x, y, z, \ldots, n)$ is any function of variables $x, y, z, \ldots, n$. $\sigma_{x,y,z,\ldots,n}$ is the estimated error on the measurement of the respective variables, and σ_f^2 is the variance of f. The estimated error on f is σ_f. For each power or voltage measurement used, the smallest division registered by either the power metre or oscilloscope was used as the error.

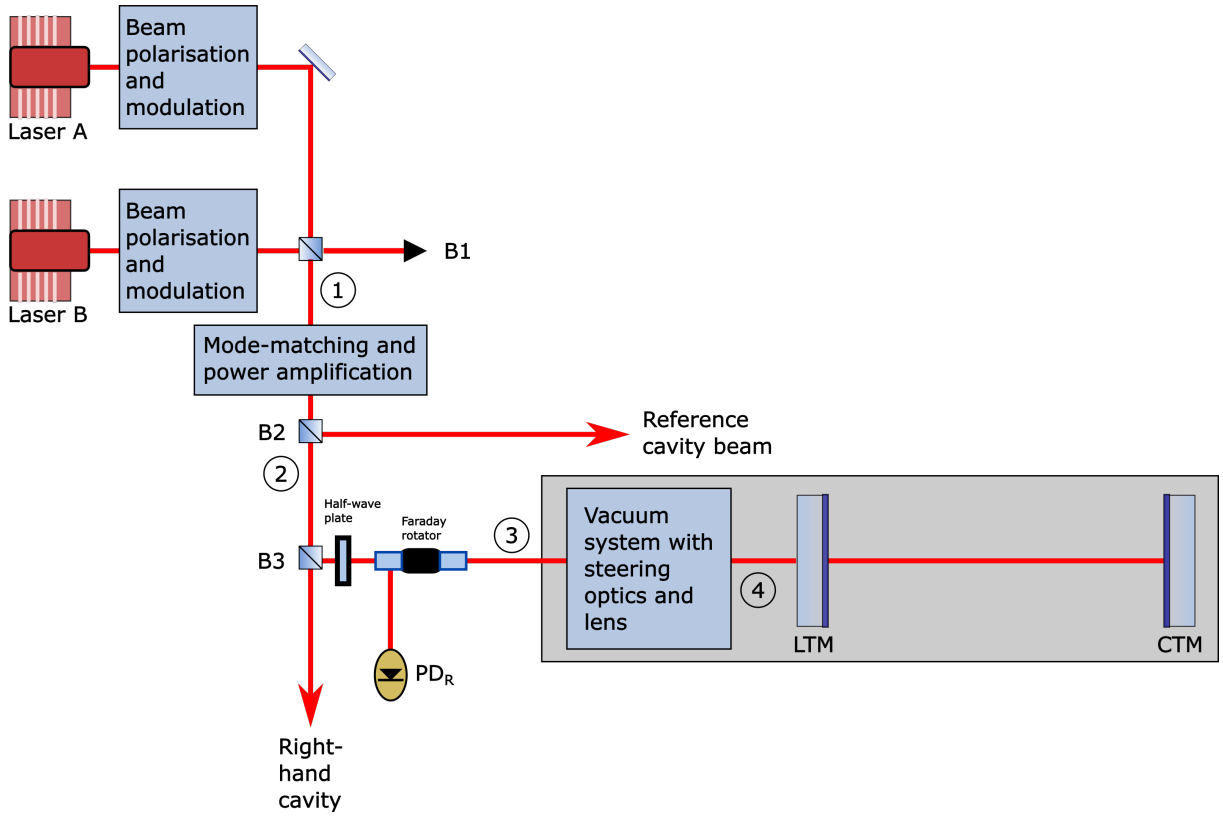

Figure 4.1: Schematic of left-hand cavity experimental setup. Point 1 is before the light from both beams goes through the laser amplifier. At this point the total power is approximately the sum of the output of both lasers. As the amplifier is non-linear, it is easier to measure the total power after this amplifier for the derivation of the total resultant power going into the experimental cavity. The characterisation of the amplifier effect on total power was carried out and is described previously in Chapter 3. The total beam power was measured at points 2, 3 and 4 with a power meter. Beamsplitters are labelled as B1, B2 and B3 and are non-polarising. The half-wave plate is used with the Faraday rotator to select the power level into the left-hand cavity. The relative DC power level of the two carriers was measured on PD_R by blocking the output of Laser A and Laser B in turn.

4.1.2 Finesse Measurement

Low Finesse Measurement The finesse, $\mathcal{F}$, of the right-hand cavity has been adjusted by using p-polarised light for the input to this part of the system, by means of a half-waveplate on the input. This works because the highly relective mirrors are coated to work best with s-polarised light and the HR and AR coatings are less efficient with p-polarised light. This results in higher cavity losses and thus a lower finesse. To measure the finesse we look at the DC voltage from the photodiode which measures the light transmitted through the right-hand cavity while the cavity is free to swing through fringes. We record this on a digital oscilloscope and obtain the plot in Figure 4.2. The free spectral range is estimated from measuring the time delay between the

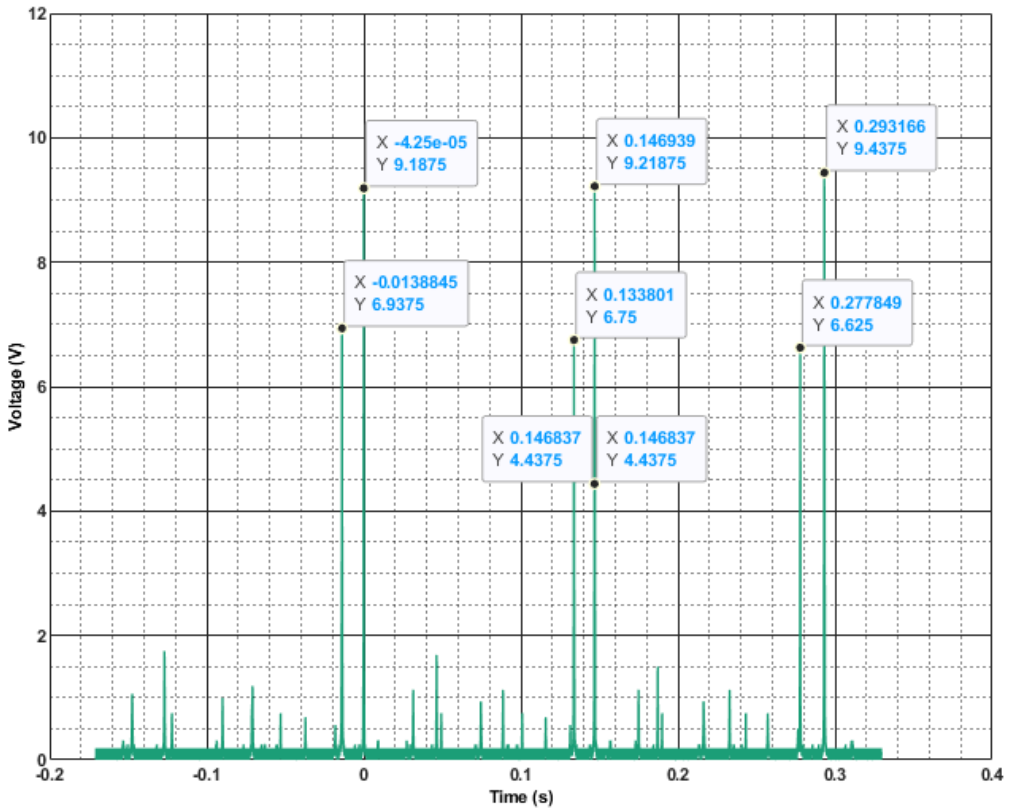

Figure 4.2: Graph of power as right-hand cavity swings through fringes. The figure shows the DC voltage on the transmitted photodiode for the right-hand cavity as the cavity is scanned through resonances. An expanded view of the central peak in this image is shown in Figure 4.3.

central peak and the next fundamental mode down in frequency, that is the labelled peak at a time delay of 4.25×10^{-5} s. The markers are used to measure the full width at half-maximum of the

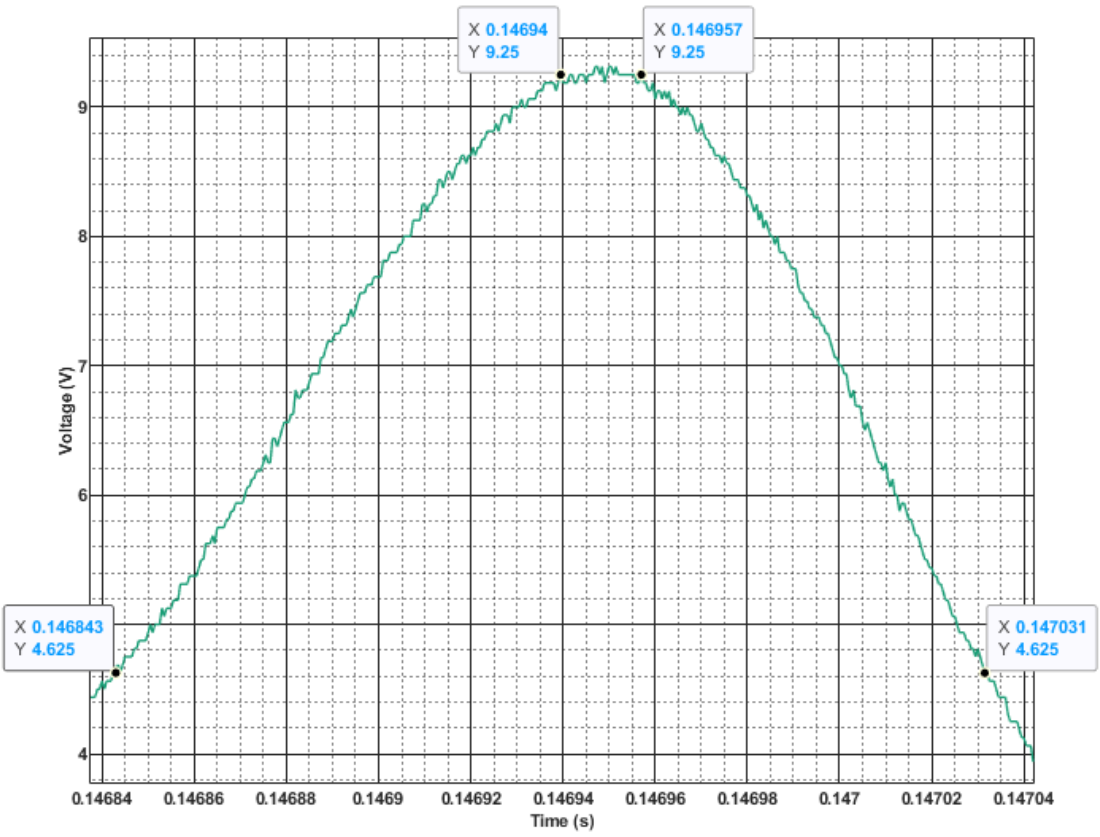

Figure 4.3: Zoomed in on central peak of Figure 4.2

fundamental mode resonance in the time domain, from around the central peak, shown zoomed in in Figure 4.3. As $\mathcal{F} = \frac{FSR}{2\gamma}$ in the frequency domain, the time delay between neighbouring modes divided by the full width of the fundamental mode gives us the finesse. The error in the measurement was estimated from the maximum size of the noise in voltage on the baseline of the graph, $\sigma_V = 0.1$ V, and the error in the x-position of the peaks $\sigma_t = 0.1$ ms, noticeable once the graph is zoomed in. The finesse for this cavity is denoted $\mathcal{F}_R$, where the error, $\sigma_{\mathcal{F}_R}$, is calculated as

$$\sigma^2_{\mathcal{F}_R} = \frac{\sigma_V^2 + \sigma_t^2}{t^2\gamma}\left(\mathcal{F}^2 + \frac{1}{4}\right), \tag{4.3}$$

$\mathcal{F}_R$ is therefore measured to be 779.838 ± 0.007.

High Finesse Measurement For the left-hand cavity, the finesse is so high that the motion of the mirrors modulates the peaks and troughs in the reflected power noticeably as the cavity swings through successive resonances. The force from the build-up of power in the cavity at the centre of resonance is very high and the narrow linewidth means the light in the cavity builds up and then decays more slowly than the speed at which the mirrors swing through resonance. This modulation of the fringe height depends on the linewidth and thus if we know the sharpness of this decay, and the cavity free spectral range, we can get a precise measurement of the cavity finesse.

To measure the free spectral range of the two cavities very accurately, they were each locked in turn to the main carrier frequency and the secondary carrier swept from $\omega_b = \omega_a + 2\pi \times 94$ MHz to $\omega_b = \omega_a + 2\pi n \Delta\nu$. As this happens the transmitted DC power is monitored on an oscilloscope and when the second laser is an integer number of free spectral ranges of the cavity, the power level on the trace will increase. This effect is very sharp in frequency and so it is vital to tune the secondary carrier local oscillator slowly around the expected frequency to find the exact point at which this laser resonates in the cavity with the main laser.

Using our measured free spectral range and a MATLAB function, which infers the finesse from ringing of the fringe as it goes through resonance, by fitting the decay of the sinusoid shown in

Figure 4.4 to determine the cavity bandwidth, a finesse of 9559 ± 88 is obtained [70]. The value taken as the finesse is the maximum value measured after taking ten measurements and the error

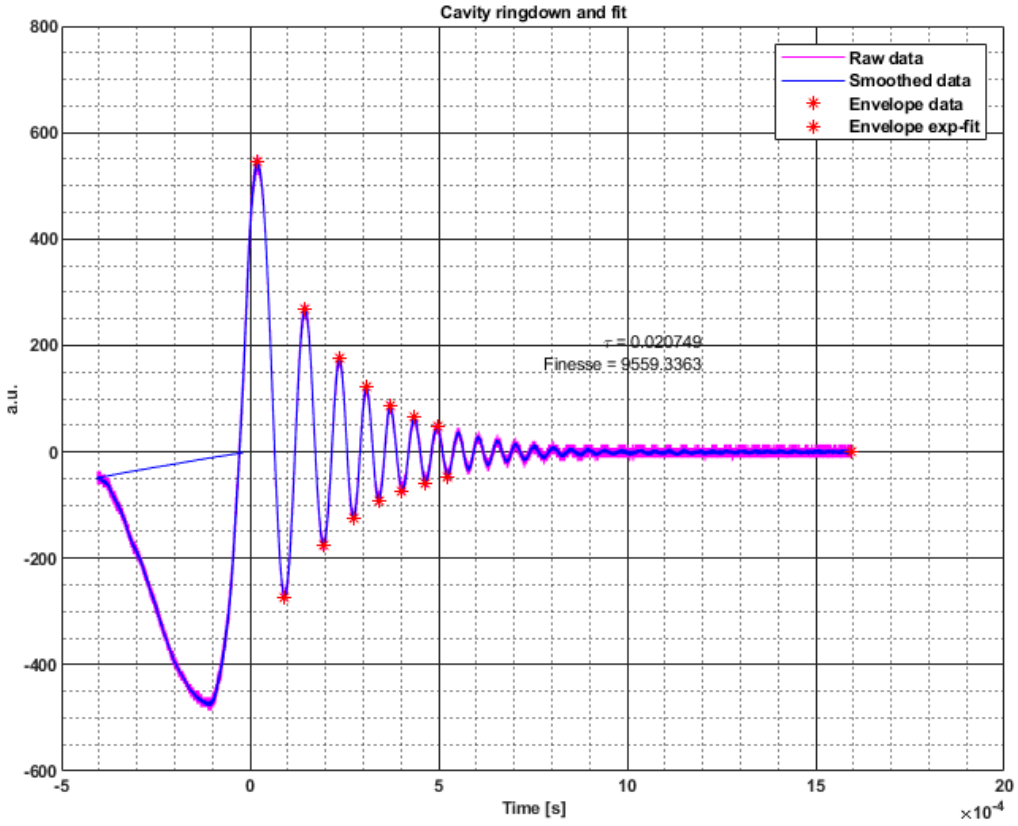

Figure 4.4: Image showing ringdown of fringe in reflected DC power as it passes through resonance. Data is in red and smoothed data used for fitting is in blue. A model fitted to the smoothed data is used to estimate the exponential decay of the oscillation, which gives the time constant of the decay and thus can be used to calculate the linewidth of the cavity.

was assumed to be half the difference between the highest finesse measured and the next down in magnitude. This is because the measured finesses will tend to be lower, but not higher, than the true finesse. The cavity half-bandwidth, γ, can be calculated from the measured finesse and free-spectral range to be $767.0\,\text{Hz} \pm 7.1\,\text{Hz}$.

4.1.3 Sideband to Carrier Ratio

It also is necessary to measure the proportion of light lost to modulation by looking at the relative heights of the sidebands on each laser compared to the carrier. In fact, the exact modulation depth of each laser is needed as an input to the numerical simulation of the experiment. The expression

for a modulated carrier is taken from Equation (A.35) in appendix A where there is a detailed analysis:

$$a_{\text{in}} \approx a_0 \left[\underbrace{J_0(\beta)}_{\text{carrier}} + \underbrace{2iJ_1(\beta)\sin(\Omega t)}_{\text{sidebands}} \right] \exp(i\omega t), \tag{4.4}$$

where β is the modulation depth.

First the relative heights of beats between all the frequency components of our signal as measured on the high frequency readout of PD_R are recorded. We measure the height of each peak in the frequency domain in micro-Volts using a high frequency spectrum analyser. Mathematically the expression for the beat between the two lasers, each with a different sideband frequency $\Omega_{a,b}$ and modulation depth, $\beta_{a,b}$ is constructed from $a_{r,a}^{\text{mod}}$, the reflected field of the main carrier and sidebands from the cavity, and $a_{r,b}^{\text{mod}}$, the reflected field of the secondary laser and sidebands from the cavity,

$$I_r = \left[a_{r,a}^{\text{mod}} + a_{r,b}^{\text{mod}} \right] \left[\left(a_{r,a}^{\text{mod}} \right)^* + \left(a_{r,b}^{\text{mod}} \right)^* \right] \tag{4.5}$$

and following the process to get I_r^{max} the reflected power from the cavity off resonance, as discussed in the appendix A for obtaining Equation (A.40). In this case the variables d_a and d_b as defined in the appendix are

$$d_a = a_{01} J_0(\beta_a) \frac{r_1 - r_2}{1 - r_1 r_2} \tag{4.6}$$

and

$$d_b = a_{02} J_0(\beta_b), \tag{4.7}$$

where a_{01} is the amplitude of the input field in the main laser before modulation and a_{02} is the amplitude of the phase locked laser, r_1 is the reflectivity coefficient of the LTM and r_2 is the reflectivity coefficient of the CTM. The variables q_a and q_b as defined in the appendix are

$$q_a = 2J_1 a_{01}(\beta_a) \sin(\Omega_a t) \tag{4.8}$$

$$q_b = 2J_1 a_{02}(\beta_b) \sin(\Omega_b t). \tag{4.9}$$

Beats between each sideband and the opposite carrier are found surrounding this main peak, separated by $\frac{\Omega_a}{2\pi} \pm 10\,\text{MHz}$ and $\frac{\Omega_b}{2\pi} \pm 10.524\,\text{MHz}$, the two modulation frequencies used for PDH length sensing of the cavities with respect to the main and secondary lasers. The cavity reflectivity is unity off resonance, as is assumed in appendix A, and on resonance the amplitude reflected from the cavity is expressed as,

$$I_r^{\max} = d_a^2+d_b^2+q_a^2+q_b^2-2d_aq_b\sin\left(\omega_{\text{LO}}t\right)+2d_bq_a\sin\left(\omega_{\text{LO}}t\right)+2d_ad_b\cos\left(\omega_{\text{LO}}t\right)+2q_aq_b\cos\left(\omega_{\text{LO}}t\right). \tag{4.10}$$

In this case there are two carrier frequencies which beat at the set phase-locking local oscillator frequency, ω_{LO}. The relative amplitude of each carrier and its sidebands give the modulation depths β_a and β_b of the sidebands. These can be obtained from the beat amplitudes of sidebands with carriers. As the measurement of these is done on a spectrum analyser and the peak amplitude is measured, take the maximum values of the sinusoids as 1. There are two sideband beats and so the average of the upper and lower sideband, that is the beat at $\Omega_{a,b}$ and the beat at $-\Omega_{a,b}$, is taken. The measurement error in this measurement is taken to be the smallest significant digit recorded for the amplitude, which is $1\times10^{-5}\,\text{V}$ for the sideband beats, and $1\times10^{-4}\,\text{V}$ for the carrier beat. The errors are propagated in quadrature as equation (4.2). The ratio between the carrier and the sidebands is j_a for the main carrier and its sidebands, and j_b for the secondary carrier and its sidebands

$$\begin{aligned} j_a &= \frac{J_1\left(\beta_a\right)}{J_0\left(\beta_a\right)} = 0.341\pm0.011 \\ j_b &= \frac{J_1\left(\beta_b\right)}{J_0\left(\beta_b\right)} = 0.185\pm0.007. \end{aligned} \tag{4.11}$$

The error estimates on these calculations are

$$v_{j_a} = \frac{1}{2\left(C_aC_b\right)^2}\left[\left(\sigma_{CS}\right)^2+\frac{1}{8}\left(\frac{\sigma_{CC}\left(S_{-a}C_b+S_aC_b\right)}{C_aC_b}\right)^2\right] \tag{4.12}$$

for the main laser, where C_aC_b is the amplitude of the beat between the two carrier frequencies, $S_{-a}C_b$ is the amplitude of the beat between the main lower sideband and the secondary carrier,

and S_aC_b is the same but with the upper instead of lower main sideband. σ_{CC} and σ_{CS} are the estimated error on the measurements of the beat between the two carriers and the beat between one carrier and the other laser's sidebands, respectively. The modulation frequency is Ω_a for the main laser. For the secondary laser with the modulation frequency Ω_b, the error on j_b is,

$$v_{j_b} = \frac{1}{2\left(C_aC_b\right)^2}\left[\left(\sigma_{CS}\right)^2 + \frac{1}{8}\left(\frac{\sigma_{CC}\left(S_{-b}C_a + S_bC_a\right)}{C_aC_b}\right)^2\right]. \tag{4.13}$$

Similarly, $S_{-b}C_a$ is the amplitude of beat between the secondary lower sideband and the main carrier, and S_bC_a is the same but with the upper instead of lower secondary sideband. It is possible to numerically calculate this ratio for a range of possible values of β and match this to the measured ratio. For the main carrier the modulation depth was found to be 0.645 ± 0.015 and for the secondary carrier the modulation depth was found to be 0.363 ± 0.010. The estimated error in β_a and β_b is

$$v_{\beta_a} = v_n + \frac{\beta_a v_{j_a}}{j_a} \tag{4.14}$$

and

$$v_{\beta_b} = v_n + \frac{\beta_b v_{j_b}}{j_b} \tag{4.15}$$

where v_n is the square of the numerical spacing of the β values used to calculate a range of numbers for m_a to compare with the measured value.

4.1.4 Visibility

The proportion of light which couples into the cavity on resonance must also be measured. From the analysis in appendix A the equation (A.30) defines the visibility, V, in terms of the reflected power on resonance, $I_r^{\min}$ and the reflected power off resonance, $I_r^{\max}$. The final expression for V in (A.44) assumes all the power is resonant in the cavity at the same frequency apart from that fraction in the sidebands. If, as is actually the case, there is a second carrier off resonance, the power reflected on resonance changes from that shown in Equation (A.41), with an extra term representing the power in the second carrier.

The measured visibility, V_m, is 0.3983 ± 0.0030. This is calculated from the measurement

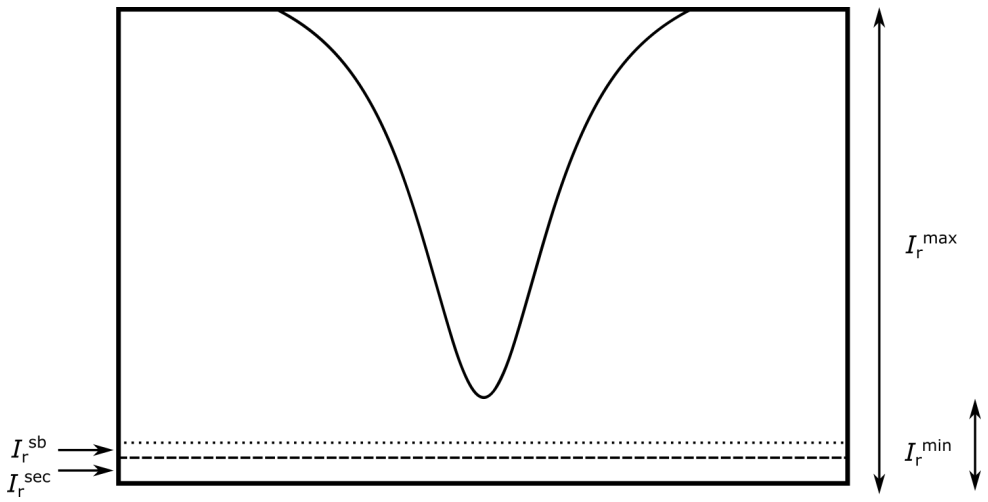

Figure 4.5: Reflected power from a Fabry-Perot cavity while changing the frequency of the laser around resonance, that is the point at which the light intensity reaches a minimum, $I_r^{\min}$. Away from resonance the reflected light is $I_r^{\max}$. $I_r^{\sec}$ is the power in the secondary laser frequency and I_r^{sb} is the power in the sidebands of the main laser.

using $V = 1 - \frac{I_r^{\min}}{I_r^{\max}}$. The error on the visibility was calculated by assuming the error on each reading was the smallest division measured, 10 mV, and using Equation (4.2) to propagate the errors to the visibility.

However it is neccessary to correct for the effect of the second carrier and the sidebands, shown in Figure 4.5. V_m can also be described in terms of the power reflected in the main carrier while on resonance with the cavity, I_r^{res}, the power reflected in the second carrier when it is not on resonance, $I_r^{\sec}$, and the power in the main carrier sidebands which is also completely reflected from the cavity when the main carrier is on resonance, I_r^{sb},

$$V_m = 1 - \frac{\left(I_r^{\mathrm{res}} + I_r^{\sec} + I_r^{\mathrm{sb}}\right)}{I_r^{\max}}. \tag{4.16}$$

Thus the corrected visibility becomes, V_c,

$$V_c = V_m + \frac{P_b^r}{\left(P_a^r + P_b^r\right)} + \left[\left(1 - J_0^2\left(\beta_a\right)\right)\frac{P_a^r}{P_a^r + P_b^r}\right] \tag{4.17}$$

which gives $V_c = 0.9255 \pm 0.0189$, with the error determined based on the previous stated errors on P_b^r, P_a^r, V_m and β_a propagated again as in Equation (4.2).

4.1.5 Calculation of Mirror Parameters

From the measured visibility and finesse it is in fact possible to determine the exact mirror transmissions and losses needed in the simulation for the desired I^e. The visibility can be given for T_L, the input power transmission coefficient of the left-hand cavity input mirror; assuming the rest of the total cavity loss is T_C

$$V_c = \frac{4xT_L^2}{T_L^2(1+x)^2} \tag{4.18}$$

assuming $T_C = xT_L$. When this is solved for T_L, this gives the expression,

$$x = -1 + \frac{2}{V_c} \pm \left(\frac{2}{V_c}\sqrt{(1-V_c)}\right) \tag{4.19}$$

where it is calculated that $x = 1.7508 \pm 0.1310$, if it is assumed T_C is the largest loss term in the cavity. Such an assumption is reasonable, as T_C contains the loss of the cavity folding mirrors, intra-cavity loss and the transmission of the CTM. To work out the value of T_L the simple expression for $\mathcal{F}$ can be used, as the losses for both mirrors are very small, as in (A.46), giving the expression,

$$\mathcal{F}_L = \frac{2\pi}{T_L(1+x)}, \tag{4.20}$$

which gives us $T_L = 239 \pm 12$ ppm and $T_C = 418 \pm 37$ ppm for the measured $\mathcal{F}_L$ and the previously determined value of x.

4.1.6 Power Circulating in Cavity

From the measured Finesse and visibility, it is possible to work out what the power enhancement factor in the cavity should be, that is the ratio between the circulating and input powers. The

expression for power enhancement is given in appendix A, as I^e (A.23).

$$I^e = \frac{4T_1}{\left(T_1 + T_2\right)^2}. \tag{4.21}$$

This gives a power enhancement in the cavity of 2210 ± 251 and a circulating power of 1700 ± 282 W. This can be used to check the simulation set-up, to check that power changes at the input correspond to changes in the circulating power, as in the experiment.

4.2 Simulation of Experimental System

4.2.1 Optickle

The simulation of the cavity and its dynamics, that is, the system 'plant', is carried out by the numerical simulation package 'Optickle2' [71]. This utilises a library of packages written in Matlab to solve the input and output equations for an electromagnetic wave in an optical configuration and set of wavelengths set by the user [72]. Other Matlab functions are constructed external to this to mimic the non-optical parts of the system.

4.2.2 Triple Carrier Optical Model

For the multiple-optical spring experiments a complete simulation called Triple Carrier Optical Model (TCOM) was set up to simulate the effect of creating optical springs with two carriers in the left-hand cavity and one of these in the right-hand cavity. This model was based on [73] for use in simulating the desired triple carrier setup and its control. The model was then adapted to match the measured experimental calibration parameters for finesse, cavity length, input power and detuning. The parameters for the control servo used for the experiment were also included in this implementation.

4.2.3 TCOM Structure

The experimental simulation **TCOM** is made up of several different functions, the structure of which is shown in Figure 4.6.

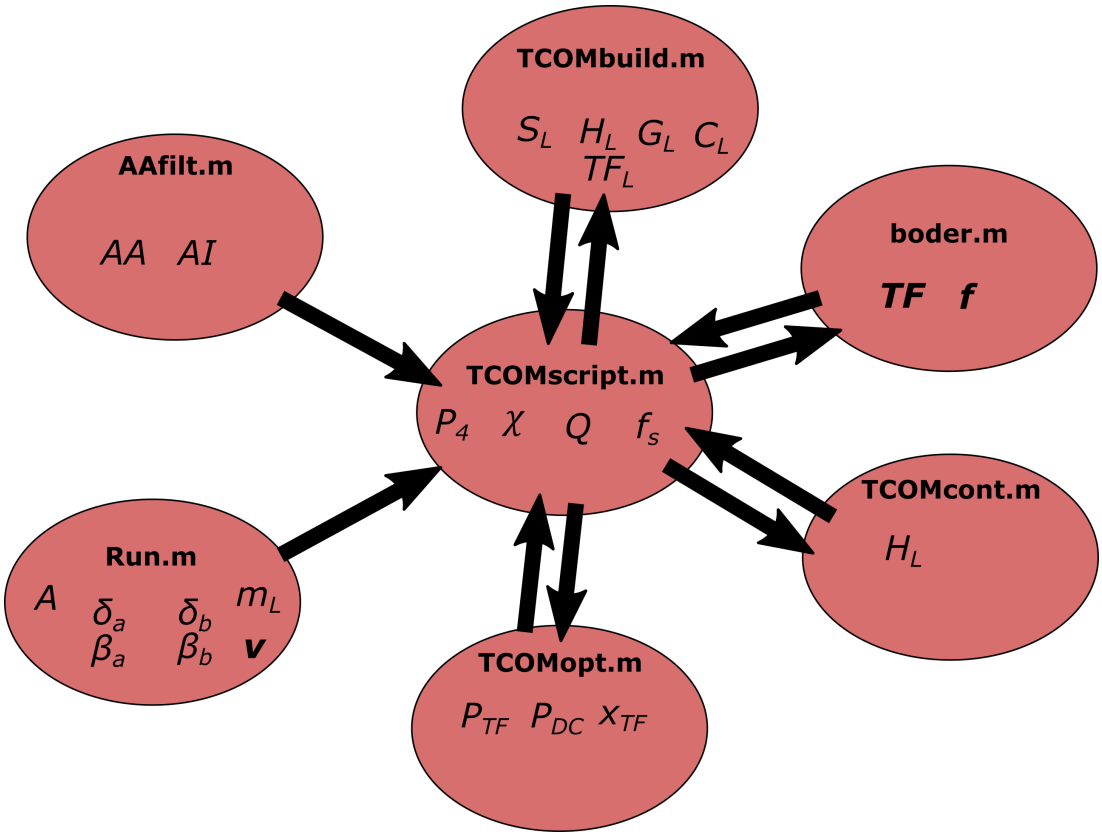

Figure 4.6: Basic Structure of the single cavity model of the experimental system. Bubbles represent MATLAB code functions except **Run.m**, which is a script to run the functions. The functions/scripts are named '.m' and are written in bold. Variables set or calculated in each function are shown under the name label and arrows show the direction information flows between the different functions/scripts.

Run.m sets the initial detunings of the main laser and secondary laser, δ_a and δ_b, and their corresponding modulation depths, β_a and β_b. In addition, it sets the initial magnitude of the control servo, A, the mass of the suspended cavity mirror, m_L, and the frequency array, ν, that the model is calculated for. It also runs **TCOMscript.m**, the numerical simulation main file.

TCOMscript.m sets the values derived from experimental calibration measurements, input power P_4, suspension susceptibility χ, suspension quality factor Q, and suspension fundamental

resonance frequency f_s. **TCOMscript** runs **TCOMopt.m**, the Optickle simulation of the single detuned cavity first.

TCOMopt.m takes in the two input carrier frequencies and wavelength of the lasers and also sets the initial cavity parameters like finesse, free spectral range and mirror reflectivity based on the measurements and calculations detailed in Section 4.1. It uses these to solve the field equations and obtain three quantities for the output of the experiment. The first, P_{TF} is the response of the power in each field component at each point in the system, as each mirror in the system is moved in position, with output as W/m. The second is P_{DC}, the static power in each field component. The third is x_{TF}, which is calculated from the response function P_{TF} with the power response of the fields divided out to create a transfer function that contains only the transfer of motion from one mirror to another due to the optical mechanical coupling in the system.

TCOMcont.m sets up the filter transfer functions of the control system and multiplies by the overall gain A, to get the linear time invariant control system response function, H_L, which is set experimentally in the digital control system used to control the cavity length, CDS.

AAfilt.m adds in analogue filtering transfer functions, applied on the input and output of the digital system to prevent extra noise being added on conversion between analogue and digital signals and vice versa. These were measured using a digital signal analyser.

TCOMbuild.m takes in P_{TF}, H_L, χ, AA and AI. It creates models of the actuation C_L, sensing S_L, control system H_L, and plant G_L; to construct models of the open loop gain and closed loop gain of the full left-hand cavity.

boder.m converts these transfer functions into **TF** and **f**; that is a set of gain arrays and frequency arrays that can be used to plot these simulated transfer functions against experimental data.

See Figure 4.6 for more details.

In Figure 4.7 a test of the simulation is presented. When a single cavity simulation of the left-hand cavity on resonance is carried out using the TCOM model, it is possible to test the circulating

power in the cavity, produced in the model output array, P_{DC}. This can be calculated at a series of different detunings in the position of one of the cavity mirrors. This array effectively represents length detunings of the cavity and can then be converted into corresponding frequency detunings relative to the laser frequency. This means a graph of power circulating in the cavity can be plotted relative to detuning in frequency from the laser resonance frequency, allowing $P_c^{\max}$, to be calculated. As can be seen in the figure, the maximum circulating power is 1698 ± 1 W and γ is 766.8 ± 0.4 Hz which matches the experimental values calculated from measurements; 1700 W circulating power and 767.0 Hz.

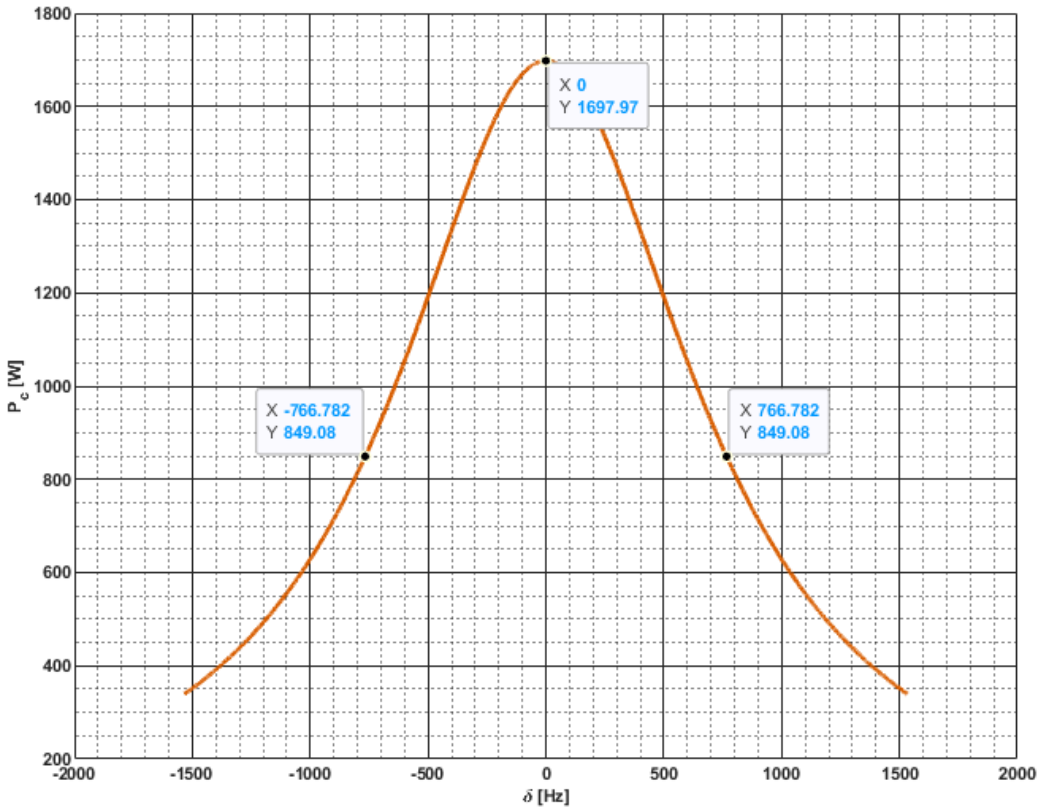

Figure 4.7: The variation in the circulating power in the simulated left-hand cavity as the cavity detuning is varied, in terms of frequency by which the cavity is detuned from the laser resonance.

4.2.4 Analysis of Mechanical Model

In order to determine some of the results expected from the simulation it is possible to analyse a mathematical model of a single mechanical spring, Figure 4.8. The damping terms are neglected

to simplify the maths, as the purpose of this analysis is to work out where the roots of the system transfer function will be and how the spring dynamics transfer from the left-hand cavity to the measurement points used. The two masses M_L and M_C take the place of the cavity mirrors and are free to move except for the spring connecting them, and a feedback force on the left-hand mass, F_{fbL}. As the feedback force from the real control system only acts in the horizontal direction, only measurements of spring dynamics along this axis are possible in the experimental set-up. Thus only forces and motion along the horizontal axis are considered. Thus is it possible to assume. The separation between M_L at $x_{0,\mathrm{L}}$ and M_C at $x_{0,\mathrm{C}}$ is the length of the spring at equilibrium with no feedback force, $L_0 = x_{0,\mathrm{L}} - x_{0,\mathrm{C}}$. As shown in the diagram, the change in length of the spring away from equilibrium due to the feedback force, is the difference in change of position of each mass, $x_{\mathrm{dL}} = x_L - x_C$. Define the motion at the error point, Σ, as

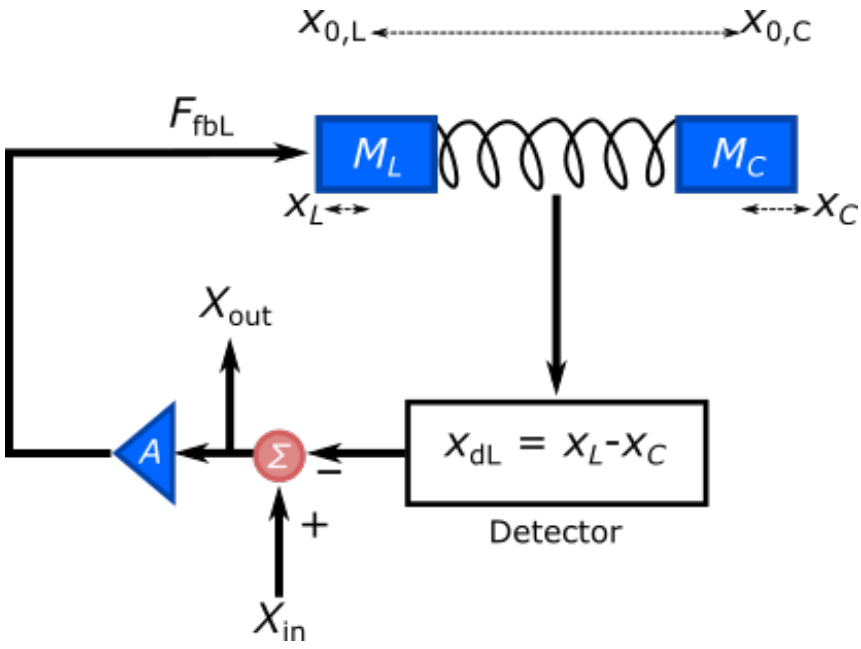

Figure 4.8: This image shows a simple mechanical spring with the same measurement and excitation points, X_{out} and X_{in}, which are used for calibration of the cavity detuning. In the physical experiment these measurements are done inside the digital control system but before the signal is shaped for locking, therefore all of the shaping and gain for this system can be considered to be contained in A, apart from that which constitutes the masses coupled by the spring. A is in fact better defined as a linear response function with dimensions of force per displacement therfore it has units of N/m.

$$-x_{\mathrm{dL}} + X_{\mathrm{in}} = \Sigma \tag{4.22}$$

where X_{out} is measured right after the sum point

$$\Sigma = X_{\text{out}}. \tag{4.23}$$

It is also necessary to look at the forces on each mass. Test masses named M_L, M_C and M_R have masses in kg of m_L, m_C and m_R, respectively. The relative extension with respect to M_L is $x_L - x_C$ and the relative extension with respect to M_C is $x_C - x_L$. The forces on M_L are

$$m_L \ddot{x}_L = F_{\text{fbL}} - k x_{\text{dL}} \tag{4.24}$$

and on M_C,

$$m_C \ddot{x}_C = k x_{\text{dL}} \tag{4.25}$$

giving the equations of motion;

$$\ddot{x}_L = \frac{F_{\text{fbL}}}{m_L} - \frac{k}{m_L} x_{\text{dL}} \tag{4.26}$$

and

$$\ddot{x}_C = \frac{k}{m_C} x_{\text{dL}}. \tag{4.27}$$

The spring constant, k, sets the resonant frequency, ω. It is possible to put the expression for unbalanced force in terms of the complex frequency parameter, s, where Ω is the frequency the mass is driven at:

$$m_L \ddot{x}_L = -m_L \Omega^2 x_{\text{dL}} = m_L s^2 x_{\text{dL}} \tag{4.28}$$

and

$$m_C \ddot{x}_C = -m_C \Omega^2 x_{\text{dL}} = m_C s^2 x_{\text{dL}} \tag{4.29}$$

where the resonant frequencies of the two masses are

$$\omega_L^2 = \frac{k}{m_L} \tag{4.30}$$

and

$$\omega_C^2 = \frac{k}{m_C}. \tag{4.31}$$

Substituting in ω and s,

$$s^2 x_L = \frac{F_{\mathrm{fbL}}}{m_L} - \omega_L^2 x_{\mathrm{dL}} \tag{4.32}$$

and

$$s^2 x_C = \omega_C^2 x_{\mathrm{dL}}. \tag{4.33}$$

The feedback force is

$$F_{\mathrm{fbL}} = A\Sigma = A\left(-x_{\mathrm{dL}} + X_{\mathrm{in}}\right). \tag{4.34}$$

It is possible to combine the equations for x_L and x_C and substitute in the equation for the feedback force, (4.34), to get an expression for the net springs extension, x_{dL}

$$x_{\mathrm{dL}} = \frac{AX_{\mathrm{in}}}{s^2 m_L} \frac{1}{\left(1 + \frac{\omega_L^2}{s^2} + \frac{\omega_C^2}{s^2} + \frac{A}{m_L s^2}\right)}, \tag{4.35}$$

which when combined with the equation for X_{out} gives the equation, (4.36),

$$X_{\mathrm{out}} = X_{\mathrm{in}} - \frac{AX_{\mathrm{in}}}{s^2 m_L} \frac{1}{\left(1 + \frac{\omega_L^2}{s^2} + \frac{\omega_C^2}{s^2} + \frac{A}{s^2 m_L}\right)} \tag{4.36}$$

relating X_{out} and X_{in} in terms of the motion of the masses. After some rearrangement, the transfer function from input to output is

$$\left(\frac{X_{\mathrm{out}}}{X_{\mathrm{in}}}\right)_{\mathrm{fb}} = \frac{s^2 + \omega_L^2 + \omega_C^2}{s^2 + \omega_L^2 + \omega_C^2 + \frac{A}{m_L}} \tag{4.37}$$

Some loop algebra is needed to find the open loop response of the system, which allows the stability of the system to be analysed. To do this, the transfer function of the system when the feedback is switched off must be evaluated. That is, the spring is not being driven. It is assumed

the gain between the output and input in this case is 1. To calculate the open loop gain use

$$\mathrm{OL_{TF}} = \frac{\mathrm{TF_{nofb}}}{\mathrm{TF_{fb}}} - 1. \tag{4.38}$$

If the values for the transfer function in the case that the feedback is on and off are substituted in then after some algebra,

$$\mathrm{OL_{TF}} = \frac{A}{m_L\left(s^2 + \omega_L^2 + \omega_C^2\right)} \tag{4.39}$$

is obtained. This open loop equation tells us that the maximum open loop gain is when $s^2 = -\omega_L^2 - \omega_C^2$. The roots of this equation are a pair of complex poles,

$$s = \pm i\left(\omega_L^2 + \omega_C^2\right)^{\frac{1}{2}} \tag{4.40}$$

It is possible to rearrange the equations for x_{dL}, x_L and x_C to get the transfer function of the absolute motion of either mass, when the feedback is on,

$$\frac{x_L}{X_{\mathrm{in}}} = \frac{A\left(s^2 + \omega_C^2\right)}{m_L s^2\left(s^2 + \omega_L^2 + \omega_C^2 + \frac{A}{m_L}\right)} \tag{4.41}$$

and

$$\frac{x_C}{X_{\mathrm{in}}} = \frac{A\omega_C^2}{m_L s^2\left(s^2 + \omega_L^2 + \omega_C^2 + \frac{A}{m_L}\right)} \tag{4.42}$$

which shows how the dynamics of an individual mirror are altered by the presence of a spring, in this very simple case. This will later be important in the analysis of single spring calibration measurements.

4.2.5 Injecting Signals on CTM

In order to determine some of the results expected from the simulation for the CTM to LTM and RTM measurements, it is necessary to extend this analysis to cover this case also. The parameters are the same as for the calculations applied to LTM error point injection analysis, and we neglect damping to start with. The only difference is the injection and measurement voltage signals in

the real experiment are obtained from the digital control system at the output right before these voltages are applied to the mirror coil drivers. Therefore, instead of thinking about the input and output signals as displacements at the error point of the system, it makes more sense to think of them as forces onto the masses. The input force, F_{in}, is directly onto M_C and the output force, F_{out}, is the force being fed back to M_L. A diagram of this set-up is shown in 4.9. In this case

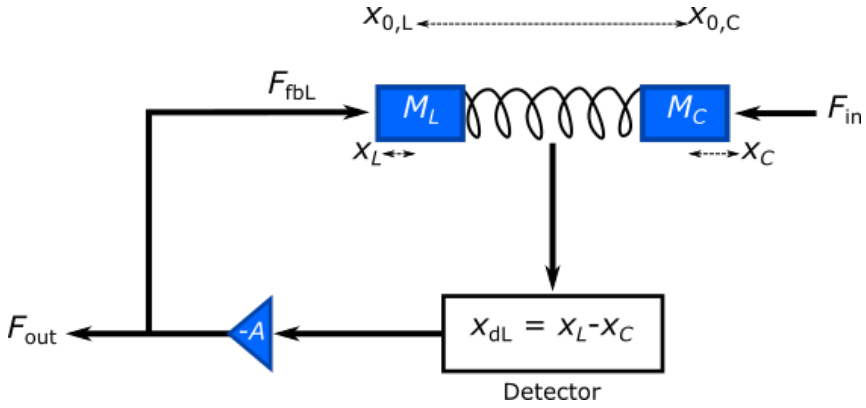

Figure 4.9: This diagram allows the response of the control system to injection on the mass which is not held in place by the control system, to be calculated. As the input excitation is outside the servo loop this time, the minus sign is accounted for in the gain block instead of at the summing point at the input of the servo.

$$-Ax_{\text{dL}} = F_{\text{fbL}} \tag{4.43}$$

and

$$F_{\text{fbL}} = F_{\text{out}}. \tag{4.44}$$

It is also necessary to look at the forces on each mass, assuming again that these are all along the horizontal axis and that any forces in the orthogonal directions are balanced. For M_L

$$m_L\ddot{x}_L = F_{\text{fbL}} - kx_{\text{dL}} \tag{4.45}$$

and for M_C

$$m_C\ddot{x}_C = F_{\text{in}} + kx_{\text{dL}}, \tag{4.46}$$

giving equations of motion,

$$\ddot{x}_L = \frac{F_{\text{fbL}}}{m_L} - \frac{k}{m_L}x_{\text{dL}} \tag{4.47}$$

and

$$\ddot{x}_C = \frac{F_{\text{in}}}{m_C} + \frac{k}{m_C} x_{\text{dL}}, \tag{4.48}$$

which gives

$$s^2 x_L = \frac{F_{\text{fbL}}}{m_L} - \omega_L^2 x_{\text{dL}} \tag{4.49}$$

and

$$s^2 x_C = \frac{F_{\text{in}}}{m_C} + \omega_C^2 x_{\text{dL}}. \tag{4.50}$$

An expression for the net springs extension, x_{dL}, in this new case is,

$$x_{\text{dL}} = \frac{-F_{\text{in}}}{m_C} \frac{1}{\left(s^2 + \omega_L^2 + \omega_C^2 + \frac{A}{m_L}\right)}, \tag{4.51}$$

which is substituted into the expression for F_{fbL}, to get

$$F_{fb1} = -A \frac{-F_{\text{in}}}{m_C} \frac{1}{\left(s^2 + \omega_L^2 + \omega_C^2 + \frac{A}{m_L}\right)}, \tag{4.52}$$

giving the equation,

$$\left(\frac{F_{\text{out}}}{F_{\text{in}}}\right)_{\text{fb}} = \frac{A}{m_C \left(s^2 + \omega_L^2 + \omega_C^2 + \frac{A}{m_L}\right)} \tag{4.53}$$

relating F_{out} and F_{in} in terms of the motion of the masses. In this case, setting the feedback signal to zero, the same expression relating F_{out} and x_{dL} is obtained,

$$F_{\text{out}} = -A x_{\text{dL}}. \tag{4.54}$$

The motion of M_C is also the same as in the case with feedback, but the motion of M_L is no longer driven by F_{fb1},

$$m_L \ddot{x}_L = -k x_{\text{dL}}. \tag{4.55}$$

Going through the algebra, an expression,

$$x_{\text{dL}} = \frac{-F_{\text{in}}}{m_C} \frac{1}{\left(s^2 + \omega_L^2 + \omega_C^2\right)} \tag{4.56}$$

for x_{dL} with no feedback is obtained. Thus we get the expression,

$$\left(\frac{F_{\mathrm{out}}}{F_{\mathrm{in}}}\right)_{\mathrm{nofb}} = \frac{A}{m_C\left(s^2+\omega_L^2+\omega_C^2\right)} \tag{4.57}$$

for the transfer function in this case.

Again using the equation for open loop gain, (4.38), the expression for the open loop gain when injecting on M_C and reading back the force on M_L is the same as in the previous calculation in Section 4.2.4, where we injected on the error point of the servo and measured right after this, Equation (4.39). The transfer function in the absence of feedback, cannot be measured for the actual optical spring, as it always requires some force applied to the LTM in order to keep the system near the operating point where the spring can be observed. Thus for actual analysis the measured transfer function from the CTM feedback signal to the LTM feedback signal will be used, analogous to the mechanical model transfer function, Equation (4.53). The transfer function equation with feedback is,

$$\left(\frac{F_{\mathrm{out}}}{F_{\mathrm{in}}}\right)_{\mathrm{fb}} = \frac{A}{m_C\left(s^2+\omega_L^2+\omega_C^2+\frac{A}{m_L}\right)}, \tag{4.58}$$

allowing analysis of the measured data in this case.

4.2.6 Using Local Readout

In the case where there is an 'out-of-loop' meter for the dynamics of the spring, the following analysis is considered instead. Figure 4.10 extends the analysis to the right-hand cavity readout where F_{fbR} acts as a sensor for the spring altered motion of the CTM. This results in the measured C to R transfer function,

$$\left(\frac{F_{\mathrm{out}}}{F_{\mathrm{in}}}\right)_{\mathrm{fb}} = \frac{\left(s^2+\omega_L^2+\frac{A}{m_L}\right)}{\left(s^2+\omega_L^2+\omega_C^2+\frac{A}{m_L}\right)} \tag{4.59}$$

where it is assumed that the readout spring's control system feedback strength, B, is very high and transfers all the motion of M_C onto M_R. During injection onto M_C the motion of this mass

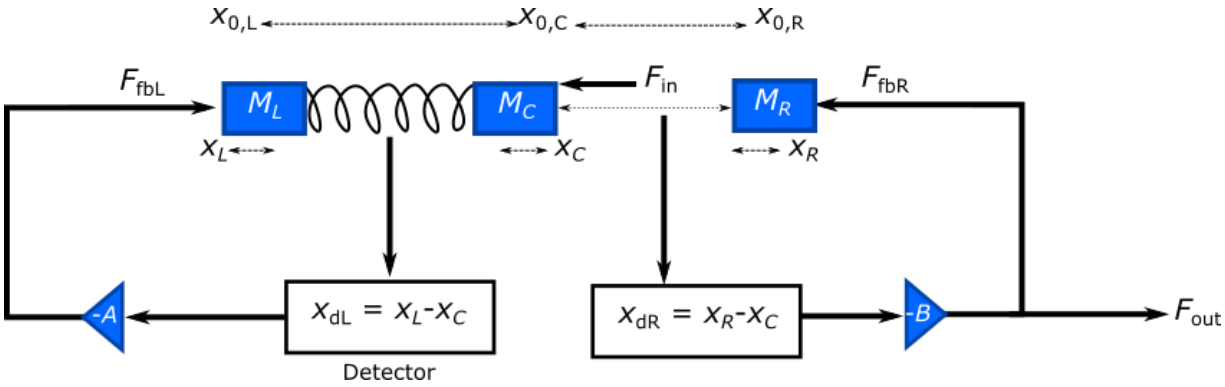

Figure 4.10: This diagram shows the measurement from Figure 4.9 with the right-hand cavity loop also in place to act as a monitor of the CTM motion.

has the transfer function,

$$\frac{x_C}{F_{\text{in}}} = \frac{s^2 + \frac{A}{m_L} + \omega_L^2}{m_C s^2 \left(s^2 + \omega_L^2 + \omega_C^2 + \frac{A}{m_L} \right)}, \tag{4.60}$$

which is the susceptibility of the mass in the cavity that is not held by the strong servo gain, and is thus an ideal quantity to look at to see the direct effect of strong optomechanics on a suspended mass.

4.3 Measuring on the RTM

To verify that the RTM is the correct place to measure a signal we should verify experimentally that dynamics from the CTM can be measured on the RTM. In order to do this, we measure a reference which tells us how the RTM moves in relation to the CTM when the right-hand cavity is locked and the CTM is behaving as an essentially free mass.That is, when there are no dynamics affecting the CTM because both cavities are operated on their respective resonance points. To avoid creating a spring from the second laser in the cavity, it is phase-locked to a frequency far-away from an integer multiple of the free spectral range. The right-hand cavity needs to be kept on resonance to avoid affecting the spring dynamics, except for the unity gain point of the right-hand cavity which will start to affect the transfer function at the top end. Our initial idea was to inject as normal at the error point of the cavity that we are using to create springs, the high finesse left-hand cavity, as in Figure 4.11. However during preliminary modelling we realised that the motion of the LTM will be attenuated a lot by the left-hand cavity response decreasing

at the cavity pole, which is at 767 Hz and so within our intended measurement range, whereas the right-hand cavity pole is at ≈ 19 kHz. Therefore greater coherence is obtained over a wide band if the injection is done on the central test mass as in Figure 4.12.

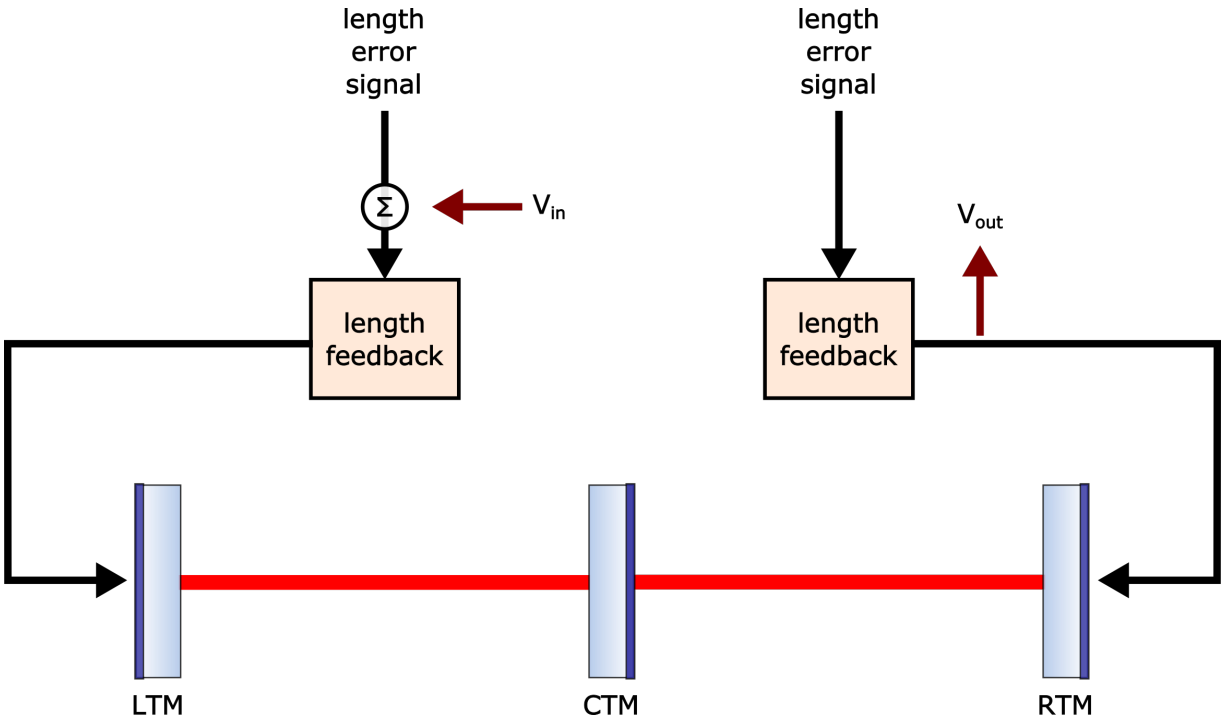

Figure 4.11: Signal injected in left-hand cavity servo error point and read back at feedback to RTM.

4.4 Calibration of Length Detuning

4.4.1 Introduction

Using the calibration from Section 4.1 as a starting point, some method is required of calibrating the relationship between the exact offset applied to the cavity length control system, and the effective cavity detuning this provides in fractions of cavity linewidth. Although this can be inferred from the estimated cavity linewidth calculated in the simulation of the resonant cavity, together with rough measurements of the fringe depth, a more precise method of calibration is required to measure the relationship between offset at the cavity error point (measured in digital voltage counts) and detuning value in Hz relative to the centre of the cavity resonance. This is effectively a measure of the slope of the error signal of the control loop in the linear part which

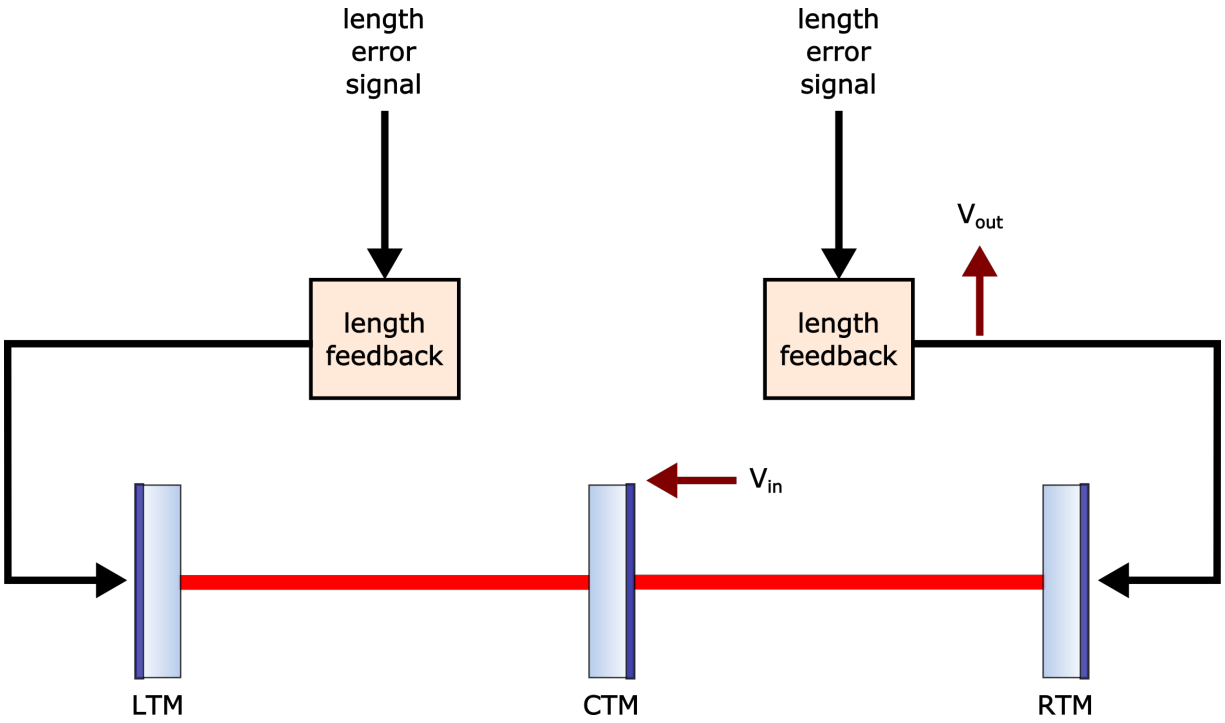

Figure 4.12: Signal injected onto CTM and read back at feedback to RTM.

is situated on and close to the resonance point in frequency.

4.4.2 Measurement

The measurement of the detuning strength is carried out by first measuring the transfer function of motion in the left-hand cavity as the LTM is moved. A simplified version of this is shown in Figure 4.8, where this measurement of X_{out} and X_{in} is carried out for a range of detuning values. For these measurements X_{in} is generated as a white noise injection over the frequency range of interest, that is, from 1 Hz to 3 kHz. Figure 4.13 is a plot of the coherence of a single spring calibration measurement, with the spring created by detuning by 0.29γ from the resonance point. From Figure 4.13 it can be seen that the measurement is only usable between about 80 Hz and 900 Hz due to the low coherence (below roughly 0.6) outside this band. Below 80 Hz the measurement is noisy as the injection is attenuated below this frequency to prevent the injection ringing up low frequency mechanical modes of the suspension systems, which will drive the servo away from the control region and eventually unlock the system. Above about 1 kHz the injection is attenuated as the unity gain point is around this value. Some pre-filtering is also carried out by the software before injection to the experimental system. This is to ensure that no narrow-

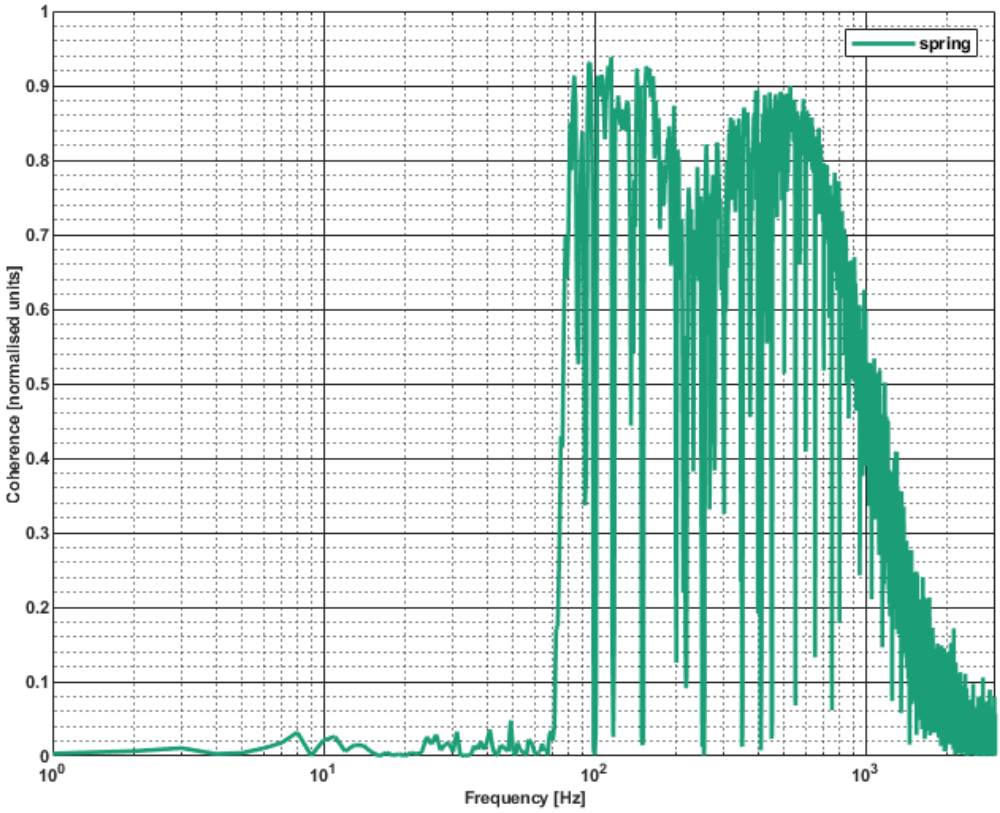

Figure 4.13: Coherence of the input and output channels read to give the transfer function of the system. A transfer function measurement only gives useful information if the coherence is closer to 1 than 0, as this means that the injected noise reaches the output without saturating any part of the electronics, and thus the measurement at this frequency can be used for analysis of the system.

band resonances of the system are driven during the measurement time. Subsequently, the open loop gain can be calculated as per Equation (4.38) for each case. The corresponding open loop gain for the measurement in Figure 4.13, is shown in Figure 4.14. As was mentioned above, the open loop gain of the system has a pair of complex poles. These give rise to a resonance in the absolute magnitude of the measurement, and a phase lead at resonance of 90°. Bode plots of the measurements can thus be compared with those produced for the simulated transfer functions from the TCOM model, with the resonance providing a precise match point, although the aim is to match the measurement and simulation over the whole measurement frequency range. To get

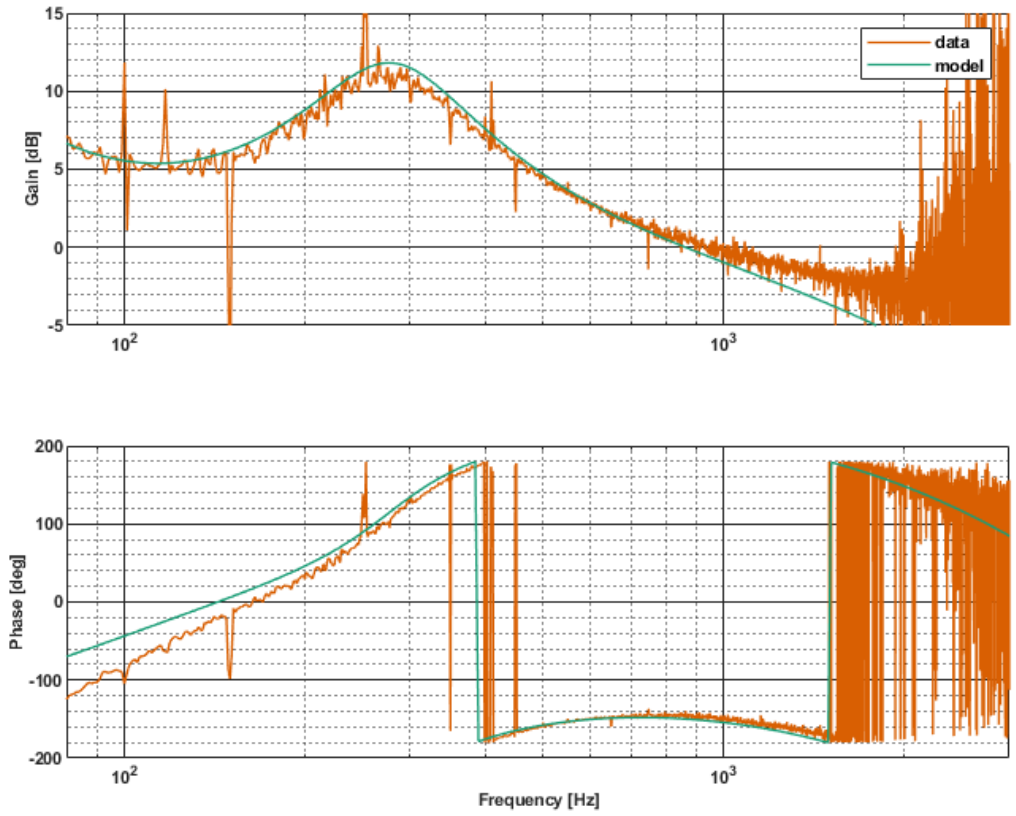

Figure 4.14: Bode Plot of one of the open loop gain measurements of the left-hand cavity used in the calibration, with a detuning of 0.31γ in the left-hand cavity. The phase is wrapped - that is plotted between $-180\,^\circ$ and $+180\,^\circ$.

a precise match, the input detuning δ_a, which is in units of fractions of γ, that is the full width at half-maximum of the cavity resonance, is adjusted by eye till a close match with experiment is obtained. Shown in Figure 4.15, is the collection of all the spring detunings measured in this

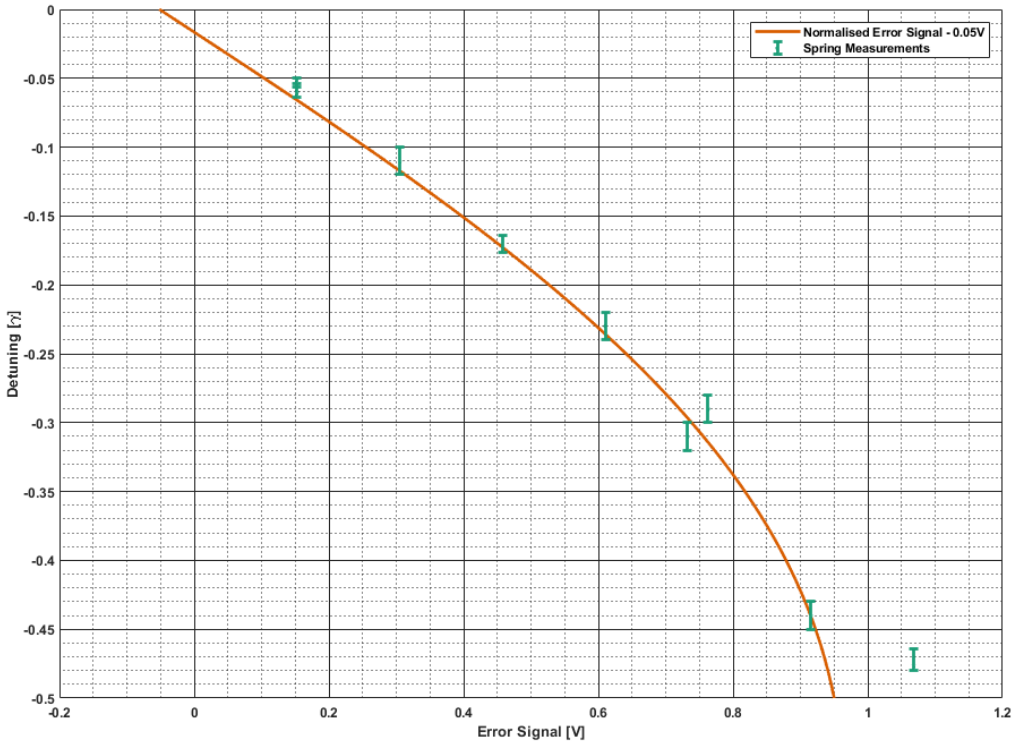

Figure 4.15: This plot shows how the measured detunings, given here in terms of fractions of the cavity γ, varied with the distance out from the centre of the error signal in voltage counts. The fitted curve uses the derivative of the the circulating power, I_c with respect to cavity detuning, normalised by the maximum value of this derivative. This is proportional to I_e, the cavity error signal.

experiment against their corresponding voltage offset from the zero point of the control system. The data was fitted by eye using a curve constructed from the derivative of the circulating power in the cavity, $\frac{\mathrm{d}}{\mathrm{dx}} I_c$, calculated from the cavity parameters and input power obtain in Section 4.1. The $\frac{\mathrm{d}}{\mathrm{dx}} I_c$ should be directly proportional to the cavity error signal, I_e [26, 33]. The curve was normalised by dividing $\frac{\mathrm{d}}{\mathrm{dx}} I_c$ by the maximum of the derivative of I_c, $\left(\frac{\mathrm{d}}{\mathrm{dx}} I_c\right)^{\mathrm{max}}$. The error on the fit at half-maximum is $\pm 0.02\,\gamma$ and ± 0.05 of the maximum error signal amplitude. The effective detuning of subsequent measurements can be determined using this curve.

All the measurements discussed in this chapter were used to inform the simulation used to cross-check left-hand cavity measurements of springs discussed in Chapter 5.

Chapter 5

Inertia and Trapping Results

5.1 Introduction

The aim of the experimental work in this thesis was to discover evidence for the phenomena of negative inertia and optical trapping in the high power cavity set-up in the Glasgow 10 m prototype. Both phenomena require a combination of spring and anti-spring to be created, coupled to a common mirror. A series of transfer functions was measured for a range of spring/anti-spring combinations created in the left-hand cavity, with signals injected onto the actuator for the CTM, the setup shown in Figure 4.12. Further measurements were taken of some spring/anti-spring pairs as gain was incrementally decreased at the lower end of the experimental frequency range. This was done to gauge whether the system would stay locked with reduced gain at low frequencies, from which it could be inferred that the dominant force at these frequencies was optomechanical.

For all the measurements carried out in these two experiments, two methods of readout were utilised: using the signal from the left-hand cavity control system fed back to control the LTM motion as the output of the transfer function and using the signal from the right-hand cavity control system fed back to control the RTM motion as the output of the transfer function. This latter signal was to be used to investigate so-called 'local readout' that minimises the usual measurement noise from measuring inside a high gain control loop.

The theoretical underpinning for negative inertia, is discussed in Chapter 2. The mathematical treatment is discussed in [4, 5].

5.2 Determination of Left-Hand Cavity Dynamics

As mentioned in Chapter 2 previous measurements of high power optical springs in the Glasgow prototype system have been carried out with methods that involved injecting the measurement signal at point 1 (Figure 5.1) in the left-hand cavity length stabilisation loop. Figure 5.1 shows

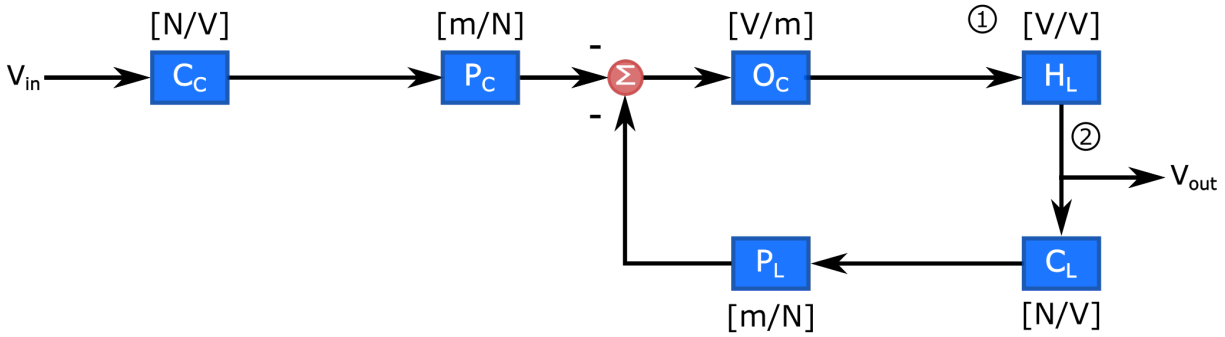

Figure 5.1: Image of CTM to LTM measurements when no springs are present and the electronic feedback loops are closed. Point 1 shows where the output signal would be measured for injections into the error point of the servo. Point 2 shows where the output signal is measured for injections onto the CTM.

Symbol	Response Function	Units
C_C	CTM coil driver	N/V
C_L	LTM coil driver	N/V
H_L	left-hand cavity locking servo	V/V
O_C	signal due to the PDH signal from the cavity motion detected at the servo input	V/m
P_C	CTM suspension	m/N
P_L	LTM suspension	m/N
K_L	total spring in left-hand cavity	N/m

Table 5.1: Response functions for loop calculations of left-hand cavity measurements.

the measurement setup for the CTM injections in the case in which the feedback to the LTM is used as the output signal of the transfer function. The output of C_L is negative, as the sign of

the loop feedback should be negative to suppress any applied injection in the loop. Similarly, the output of C_C is also negative as the servo can not distinguish between motion of either cavity mirror, and instead senses the overall change in cavity length. Therefore, the sign at the output of C_C should match the sign at the output of C_L. The symbols are explained in Table 5.1. Point 1 shows where the output signal would be measured for injections into the error point of the servo. These type of measurements are used for calibrating the cavity detunings detailed in Sub-section 4.4.2. The open loop gain for these measurements can be expressed as:

$$C_L P_L O_C H_L. \tag{5.1}$$

The closed loop gain for these calibration measurements can be expressed as:

$$\frac{C_L P_L O_C H_L}{\left(1 + C_L P_L O_C H_L\right)} \tag{5.2}$$

Point 2 in Figure 5.1 shows where the output signal is measured for injections into the CTM feedback point. The equation for the gain for this CTM to LTM measurement is:

$$\frac{V_{out}}{V_{in}} = \frac{-C_C P_C O_C H_L}{\left(1 + C_L P_C O_C H_L\right)} \tag{5.3}$$

Figure 5.2 shows the same measurement setup but with a spring K_L created in the cavity. Equation (5.4) is the expression for the measurement. K_L represents a spring, the expression for which is given in Equation (2.13). This means it has a restoring force at low frequencies. The feedback from the spring has a negative sign as it acts in the opposite direction to the force coming from the actuators, which act on the backs of both mirrors. If K_L was an anti-spring, the feedback from the spring block would have the opposite sign.

The block P_L is the only one common to both feedback paths. The combination of P_C and K_L can be written as the closed loop response $\frac{P_C}{1+P_C K_L}$, thus the full equation for CTM injection and

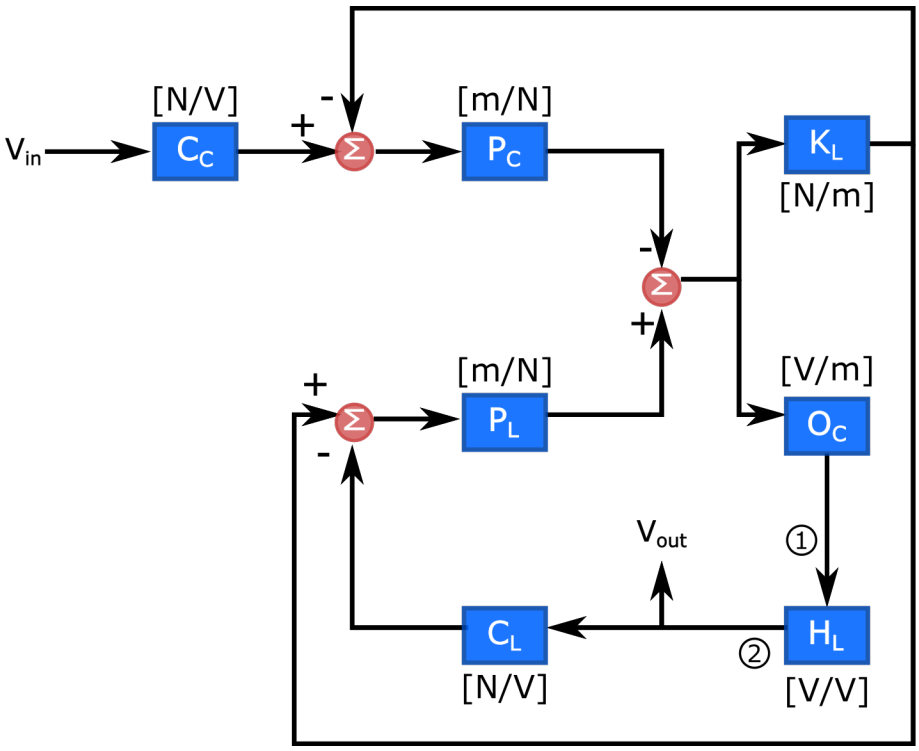

Figure 5.2: Image of CTM to LTM measurement simplified to show the effect of a spring on the loop model. V_{in} is the injection into the CTM coil drivers. Point 1 is where the calibration injections are performed. Point 2 is the left-hand cavity measurement point for CTM injections.

left-hand cavity error point is:

$$\frac{V_{out}}{V_{in}} = \frac{-C_C\left(\frac{P_C}{1+P_CK_L}\right)O_CH_L}{\left(1+C_L\left(\frac{P_C}{1+P_CK_L}\right)O_CH_L\right)}, \tag{5.4}$$

which is the same as the initial expression obtained in Equation (5.3), but replacing P_C with $\frac{P_C}{1+P_CK_L}$.

The negative inertia measurements require an understanding not just of the relative length change of the cavity, as used for sensing in the previous treatment, but of how the individual mirror motion is affected by the spring. This is necessary because of the injection onto the CTM, which requires understanding of how the system operates in the frame of the CTM and not the LTM.

Time domain analysis allows treatment of the system due to the instantaneous forces acting on the system. Such a treatment is shown in Figure 5.3. In this diagram x is the relative length

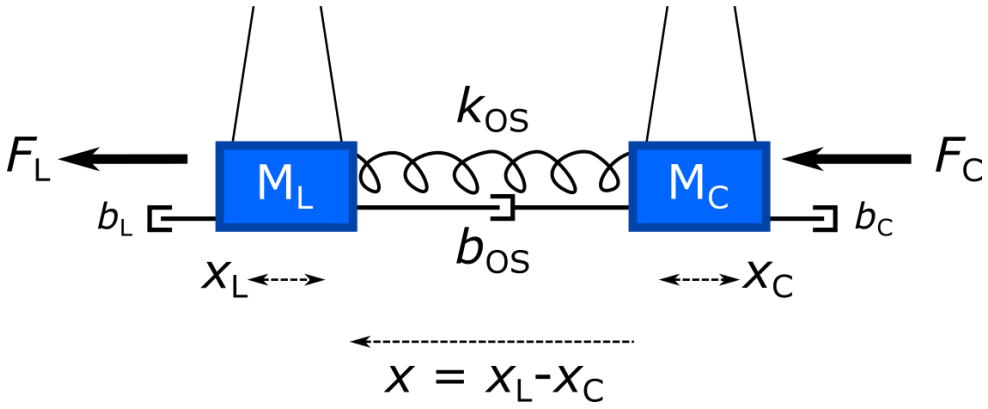

Figure 5.3: Suspended mass M_L represents the LTM and M_C represents the CTM, connected by an optical spring with a complex spring constant with rigidity k_{OS} and damping b_{OS}. Each mass has local inertial damping, b_L and b_C, respectively. The force on M_L is F_L due to the cavity control system, and the force F_C is that due to the injection onto the CTM. x_L is the position of M_L relative to its position at rest. x_C is the position of M_C relative to its position at rest. The total length change of the cavity is denoted x.

change of the cavity, and M_L and M_C are the suspended LTM and CTM respectively. There is an optical spring in the cavity with rigidity $k_{OS} = \mathfrak{R}\left(K_{OS}\right)$, and damping $b_{OS} = \mathfrak{I}\left(\frac{K_{OS}}{\Omega}\right)$. To measure the system a signal is injected onto the CTM, producing a force F_C on the suspended mass M_C. The control system exerts a force F_L on M_L to counteract the length change of the cavity in response to the injection. The direction of positive x is defined as to the left in this example. It is necessary to determine an expression for change in longitudinal position of the two mirrors: x_C for the CTM and x_L for the LTM; as well as the overall cavity length change, x.

The input variables are

$$\begin{bmatrix} \dot{x}_L \\ \dot{x}_C \\ \ddot{x}_L \\ \ddot{x}_C \end{bmatrix} = \begin{bmatrix} 0 & 0 & 1 & 0 \\ 0 & 0 & 0 & 1 \\ \frac{k_{OS}}{M_L} & \frac{-k_{OS}}{M_L} & \frac{-b_{OS}+b_L}{M_L} & \frac{b_{OS}}{M_L} \\ \frac{k_{OS}}{M_C} & \frac{-k_{OS}}{M_C} & \frac{-b_{OS}}{M_C} & \frac{b_{OS}-b_C}{M_C} \end{bmatrix} \begin{bmatrix} x_L \\ x_C \\ \dot{x}_L \\ \dot{x}_C \end{bmatrix} + \begin{bmatrix} 0 & 0 \\ 0 & 0 \\ \frac{-1}{M_L} & 0 \\ 0 & \frac{1}{M_C} \end{bmatrix} \begin{bmatrix} F_L \\ F_C \end{bmatrix} \tag{5.5}$$

$$\begin{bmatrix} x_{\mathrm{L}} \\ x_{\mathrm{C}} \\ x_{\mathrm{L}} - x_{\mathrm{C}} \end{bmatrix} = \begin{bmatrix} 1 & 0 & 0 & 0 \\ 0 & 1 & 0 & 0 \\ 1 & -1 & 0 & 0 \end{bmatrix} \begin{bmatrix} x_{\mathrm{L}} \\ x_{\mathrm{C}} \\ \dot{x}_{\mathrm{L}} \\ \dot{x}_{\mathrm{C}} \end{bmatrix} + \begin{bmatrix} 0 & 0 \\ 0 & 0 \\ 0 & 0 \end{bmatrix} \begin{bmatrix} F_{\mathrm{L}} \\ F_{\mathrm{C}} \end{bmatrix} \tag{5.6}$$

This time domain analysis allows a check that the signs chosen for the applied forces and length detunings match those in the loop diagram shown in Figure 5.2.

5.3 Local Readout with the Right-Hand Cavity

Measuring within the left-hand cavity control loop means the measured signal will have the noise of the whole control loop imposed on it and so it will be more difficult to deduce spring dynamics. If the measurement is instead carried out via an independent transducer of the cavity length, this will result in less correlations between the noise imposed on the measurement signal and that on the injected signal. If the measurement point is able to be stabilised with a higher unity gain than the system being measured then this should ensure no additional noise is added by the meter (in the main range from 80 Hz to 3 kHz) to the measurement of the opto-mechanics under investigation. This independent measurement point is the feedback to the RTM.

To analyse the output measured simultaneously on the RTM, the right-hand cavity loop can be added to the control diagram; see Figure 5.4. $\mathrm{V_{in}}$ is the injection point on the CTM as in Figure 5.2 and $\mathrm{V_{out}}$ is the measurement point in the right-hand cavity. There is a minus sign at the input to the right-hand cavity summing point, as any motion of the CTM sensed by the left-hand servo will appear the opposite way around to the right-hand cavity servo. This is because the right-hand cavity will get longer if the left-hand cavity gets shorter and vice versa. There is a negative sign on the right-hand cavity feedback signal, as the RTM will follow the CTM motion due to the negative feedback. The full equation for the signal in the right-hand cavity as the CTM is moved is:

$$\frac{\mathrm{V_{out}}}{\mathrm{V_{in}}} = \frac{-\mathrm{C_R P_C H_R O_R}\left(\mathrm{C_L H_L P_L O_C} + 1 - \mathrm{P_L K_L}\right)}{\left(1 + \mathrm{C_R P_R H_R O_R}\right)\left(1 + \mathrm{C_L H_L P_L O_C} - \mathrm{K_L}\left(\mathrm{P_C} + \mathrm{P_L}\right)\right)} \tag{5.7}$$

From the equation, it can be seen that it is possible to separate the factors containing the spring from those due to the right-hand cavity control system H_R, the right-hand cavity response O_R, the right-hand cavity actuator C_R, and the RTM pendulum response function P_R. The next step in the analysis is to use this framework to get the outputs from the simulation to match the CTM to LTM measurements, then use this to inform the analysis of the CTM to RTM measurements.

5.4 Experimental Measurements

To determine how to compare the measurement and the simulation (discussed in Chapter 4) a simple example with a single spring measured at point 1 of the left-hand cavity servo (Figure 5.1) was tested against theory and simulation. This measurement was used in calibration of the length detuning of the cavity detailed in Chapter 4. From the Optickle output and a model of the pendulum uncoupled to a spring, a simulation was constructed of the mechanical susceptibility of the pendulum coupled to the spring. This is characterised as the ratio of the modified and unmodified pendulum susceptibilities $\frac{\chi_{spr}}{\chi_{pend}}$, pictured as the green trace in the bode plot in Figure 5.5. $\frac{\chi_{spr}}{\chi_{pend}}$ shows how the spring modifies the pendulum. $\frac{\chi_{spr}}{\chi_{pend}}$ was also calculated from the analytical formula using the optical spring constant given in [1], and plotted as the orange line in Figure 5.5. It can be seen that the analytical and simulation calculations for $\frac{\chi_{spr}}{\chi_{pend}}$ match well, and so the simulation was expected to provide a good match for any spring dynamics calculated analytically. Overlaying these two plots in Figure 5.5 is the purple trace, which shows $\frac{\chi_{spr}}{\chi_{pend}}$ calculated from a single spring measurement of the left-hand cavity, by injecting at point 1 in Figure 5.1 directly into a summing point and measuring at a point right after this. This measurement of $\frac{\chi_{spr}}{\chi_{pend}}$ shows a fairly close match in magnitude, and a close match in phase, to both the simulation and the calculation above 80 Hz, barring some narrow glitches which cause the phase to jitter between +180° and -180°. Figure 5.6 shows the optical spring constants (K_{OS}) for each of the cases shown in Figure 5.5: simulation in green, theory in orange, and measurement in purple. These again show a good prediction by the simulation, matching both theory and measurement, until about 400 Hz where there is a noticeable drop off in phase. This could be either from a mis-match to the measured optomechanical damping of the system or some high frequency noise term.

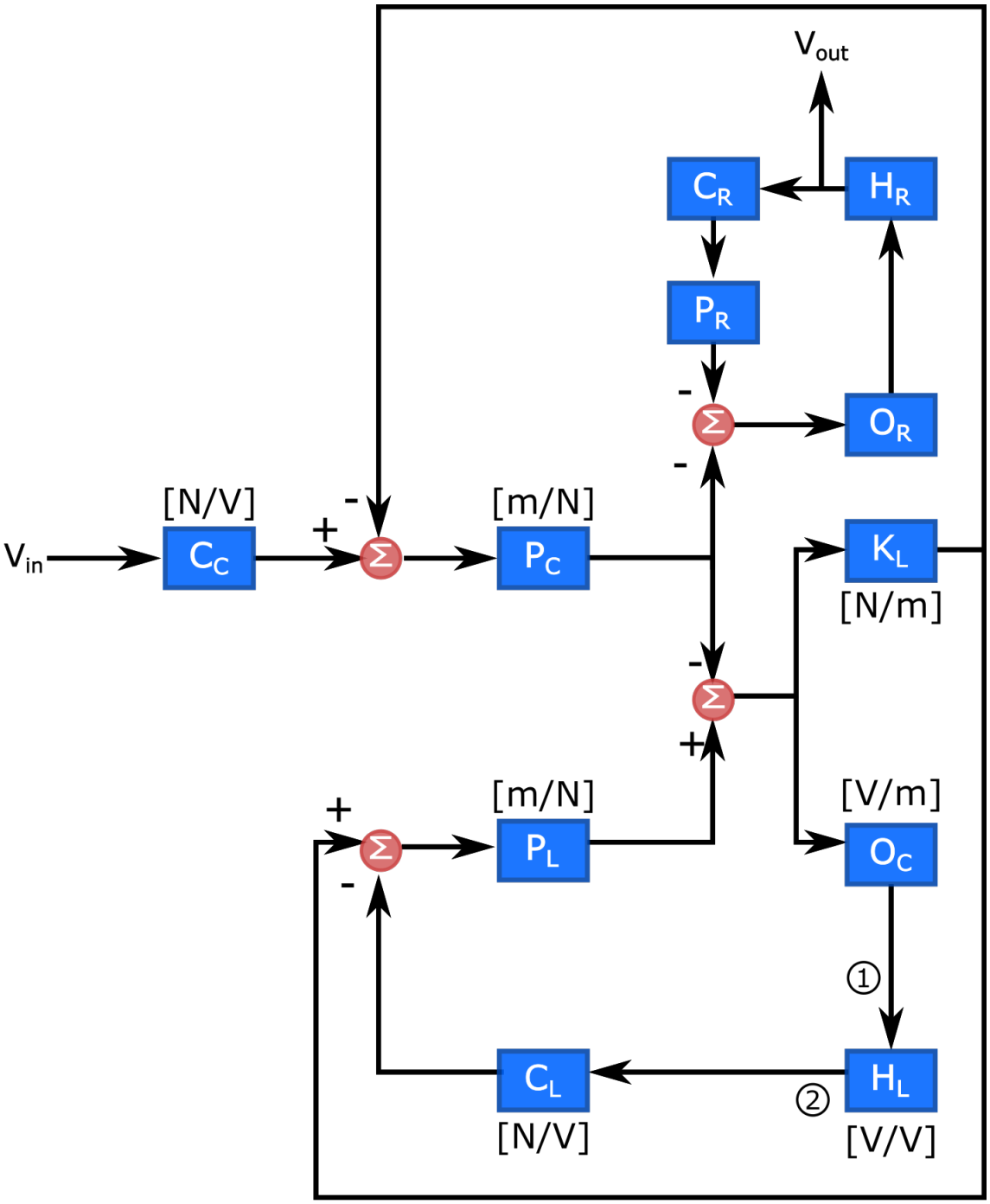

Figure 5.4: Image of CTM to RTM measurement simplified to show how the left-hand cavity loop and a spring can be sensed by the right-hand cavity loop. Point 1 is where the calibration injections are performed in the left-hand cavity. Point 2 is the left-hand cavity measurement point for CTM injections, for which V_{in} is the injection on the CTM, and V_{out} is the measurement output.

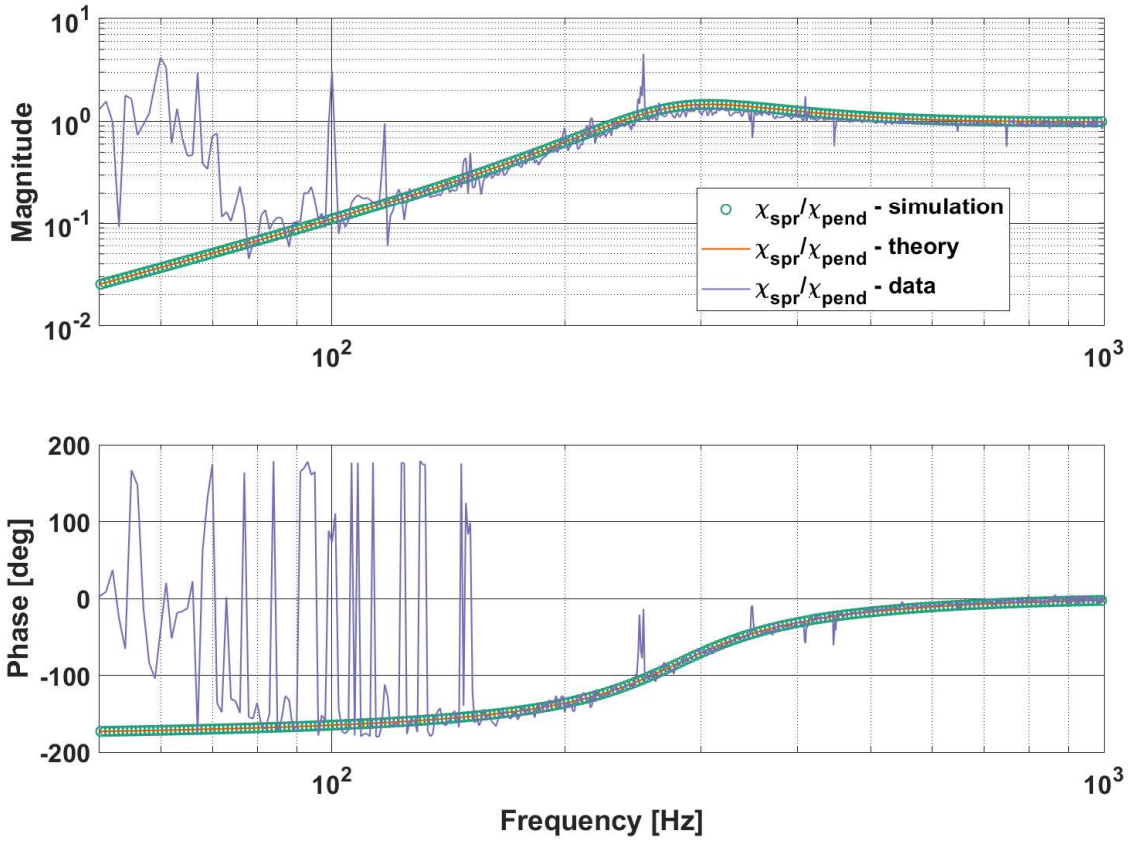

Figure 5.5: Ratio of system with spring χ_{spr} and without spring χ_{pend}, showing values for Optickle simulation in green, theoretical calculation in orange, and data in purple.

5.4.1 Calibration of CTM measurements

As shown above in Section 5.4, the detuning of the system can be described adequately by the simulation and the calculation of the relevant spring strengths. Calibration of the measurement technique is also necessary as this is different from the error point measurement used in the detuning calibration measurements, and uses the CTM actuation path. The transfer function from CTM to the LTM feedback point was measured when no springs were present in the cavity, so the cavity is held at its optical resonance and the result is shown in Figure 5.7. In terms of the theoretical treatment given in Section 5.4, this plotted quantity is equivalent to Equation (5.3),

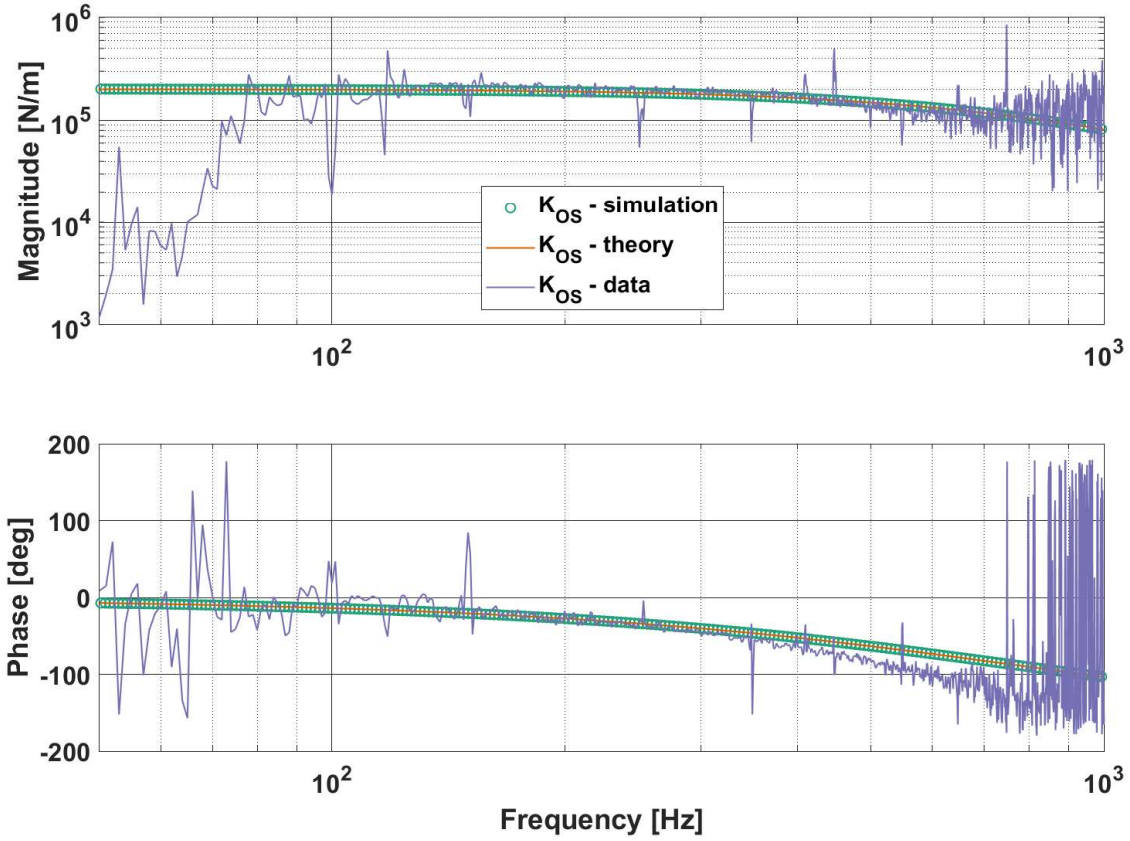

Figure 5.6: Comparison of K_{OS} values: Optickle simulation in green, theoretical calculation in orange, and data in purple.

but modified slightly to match the real system parameters:

$$\frac{V_{out}}{V_{in}} = \frac{-\alpha_1 C_C P_C O_C H_L \alpha_2}{\left(1 + C_L P_C O_C H_L \alpha_2\right)}. \tag{5.8}$$

α_1 in this equation is a number and was found by fitting the magnitude of the calculation to match the data around 80 Hz, and is there to compensate for an attenuator that appears in the actuation path to the LTM, but not the CTM. The overall gain of the left-hand cavity is represented by α_2 and was found similarly by fitting the simulation to the measurement to determine a number used to scale the transfer function. This can be accounted for, as the depth of the lock changes between successive measurement periods, due to the free swinging of the cavity and changes in the noise level from the laser frequency control servo. The second of these calibration numbers α_2, was therefore allowed to change between measurements at different detunings during analysis of CTM injections. The bump around 500 Hz in the magnitude plot shown in Figure 5.7, is due to the shaping of the cavity response which shows up in both the numerator and denominator of the Equation (5.4) as H_L. So this shaping will affect all measurements carried out by this cavity, unless the spring dynamics are larger than the servo at above 400 Hz, which is not predicted for the opto-mechanical systems used in the measurement set.

A fit for the overall servo strength was determined for each measurement using the Optickle simulation discussed in Chapter 4. Simple examples of CTM to LTM measurements and simulations are presented in Figures 5.8, 5.9, 5.10 and 5.11. For each example it can be seen that the simulation matches the measured signal well. These measurements and the subsequent measurements in Figures 5.13, 5.16, 5.19, 5.14, 5.17, 5.20, 5.15, 5.18, and 5.21 are arranged via an alpha-numeric code explained in Table 5.2.

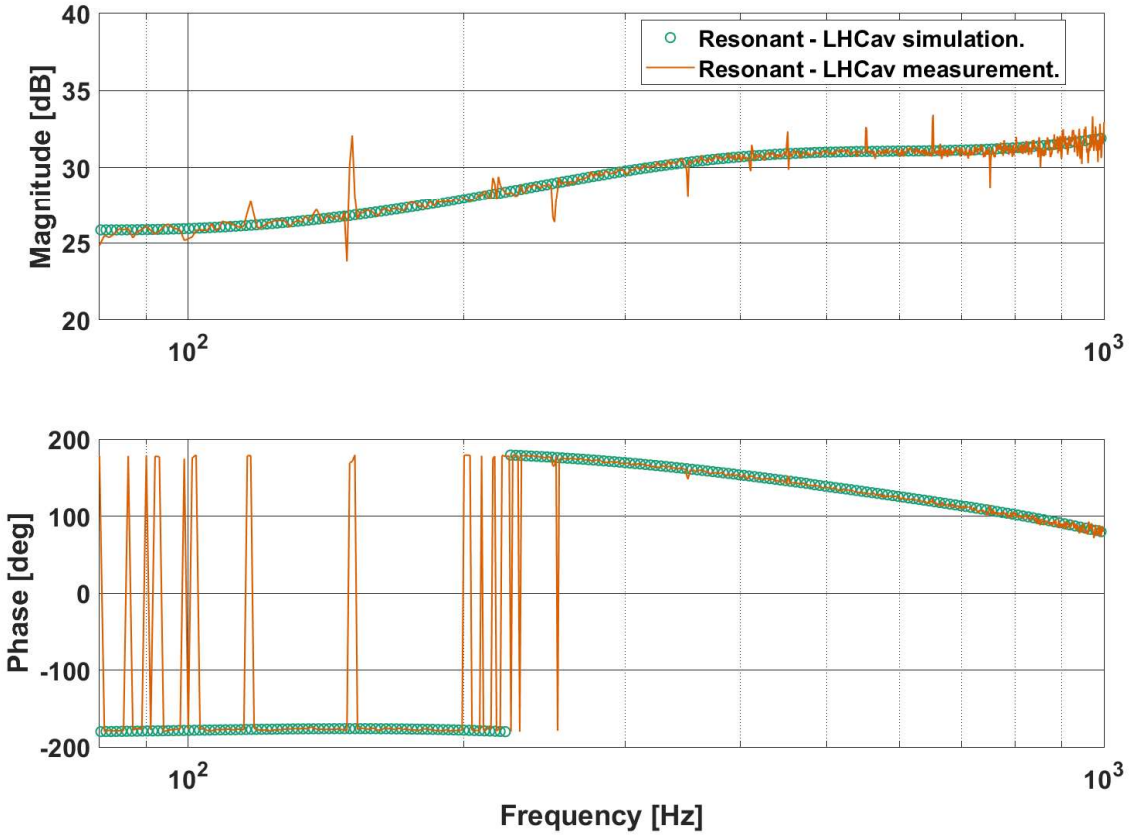

Figure 5.7: Bode plot of the measurement of the force exerted on the LTM from a force injected on the CTM when the cavity is held at its optical resonance as there are no springs or anti-springs induced. Green is the simulation and orange is the measurement.

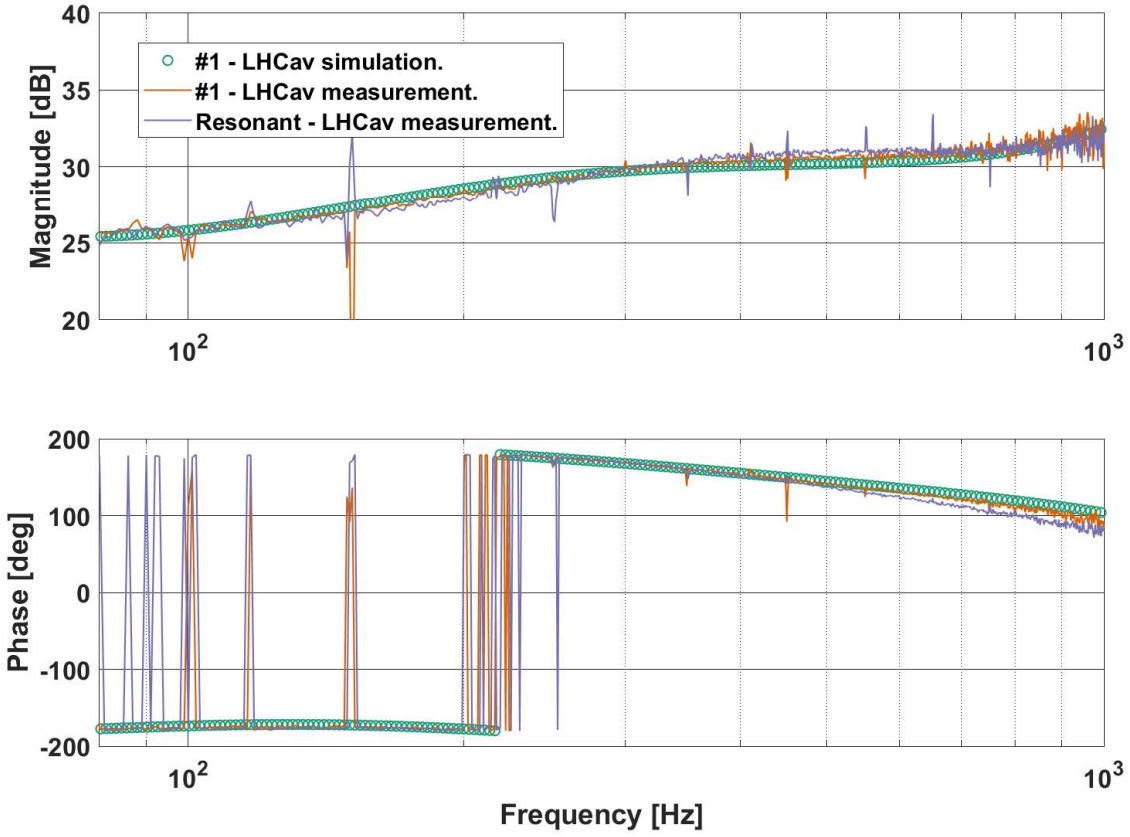

Figure 5.8: Bode plot of the measurement of the force exerted on the LTM from a force injected on the CTM for anti-spring of 1.7γ induced in the left-hand cavity. Orange is the measurement, green is the simulation, and the purple line is the measurement when the left-hand cavity is held at its optical resonance for comparison, from Figure 5.7.

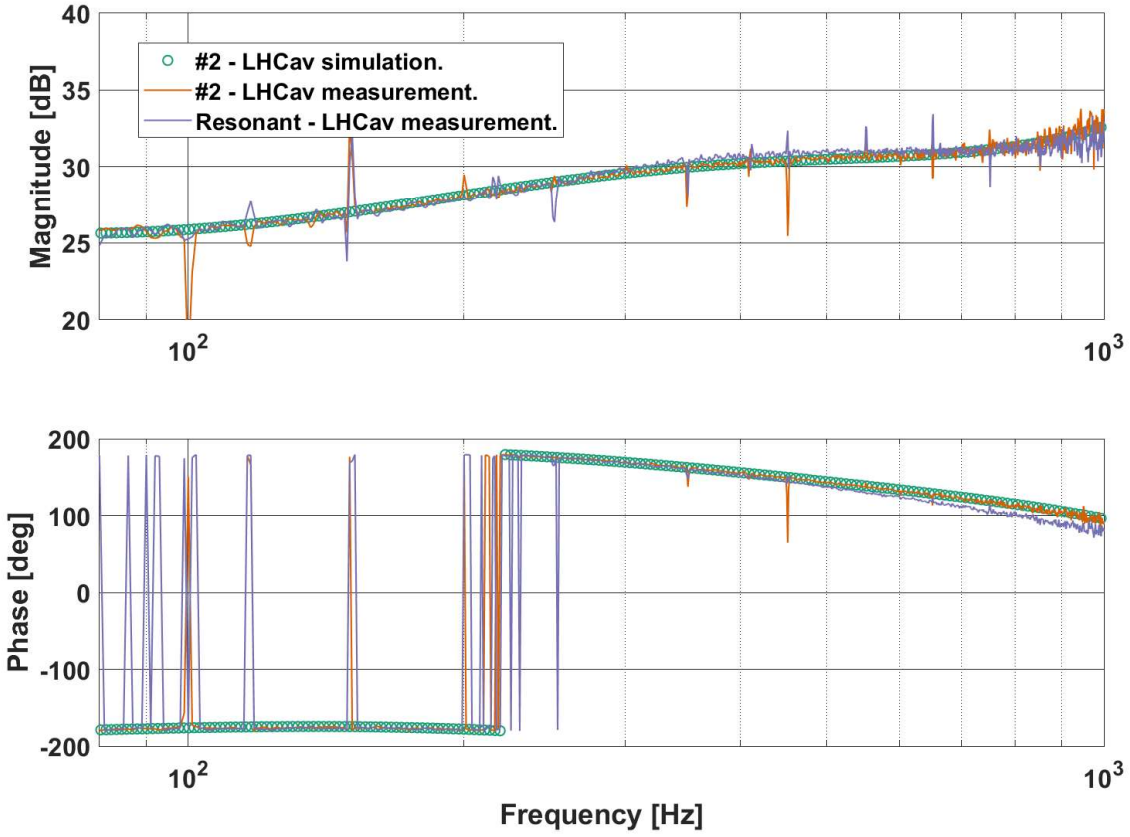

Figure 5.9: Bode plot of the measurement of the force exerted on the LTM from a force injected on the CTM for anti-spring of 2.4γ induced in the left-hand cavity. Orange is the measurement, green is the simulation, and the purple line is the measurement when the left-hand cavity is held at its optical resonance for comparison, from Figure 5.7.

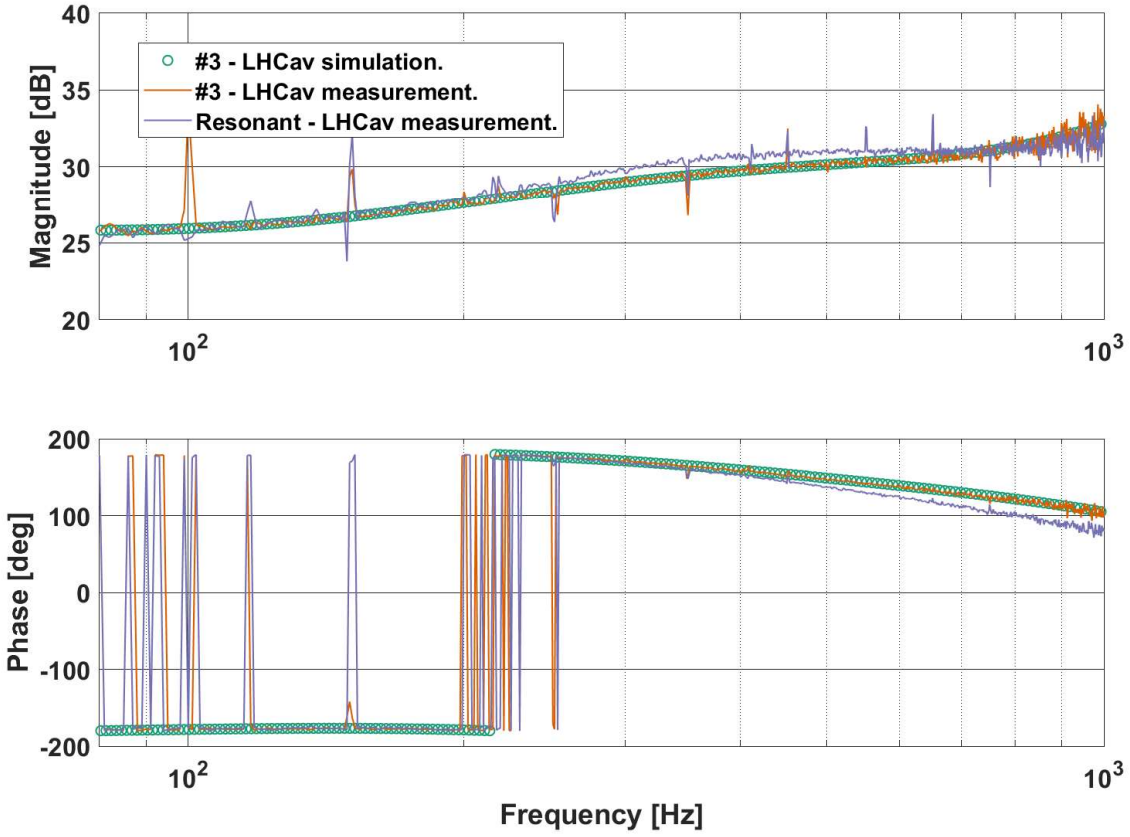

Figure 5.10: Bode plot of the measurement of the force exerted on the LTM from a force injected on the CTM for anti-spring of 3.9γ induced in the left-hand cavity. Orange is the measurement, green is the simulation, and the purple line is the measurement when the left-hand cavity is held at its optical resonance for comparison, from Figure 5.7.

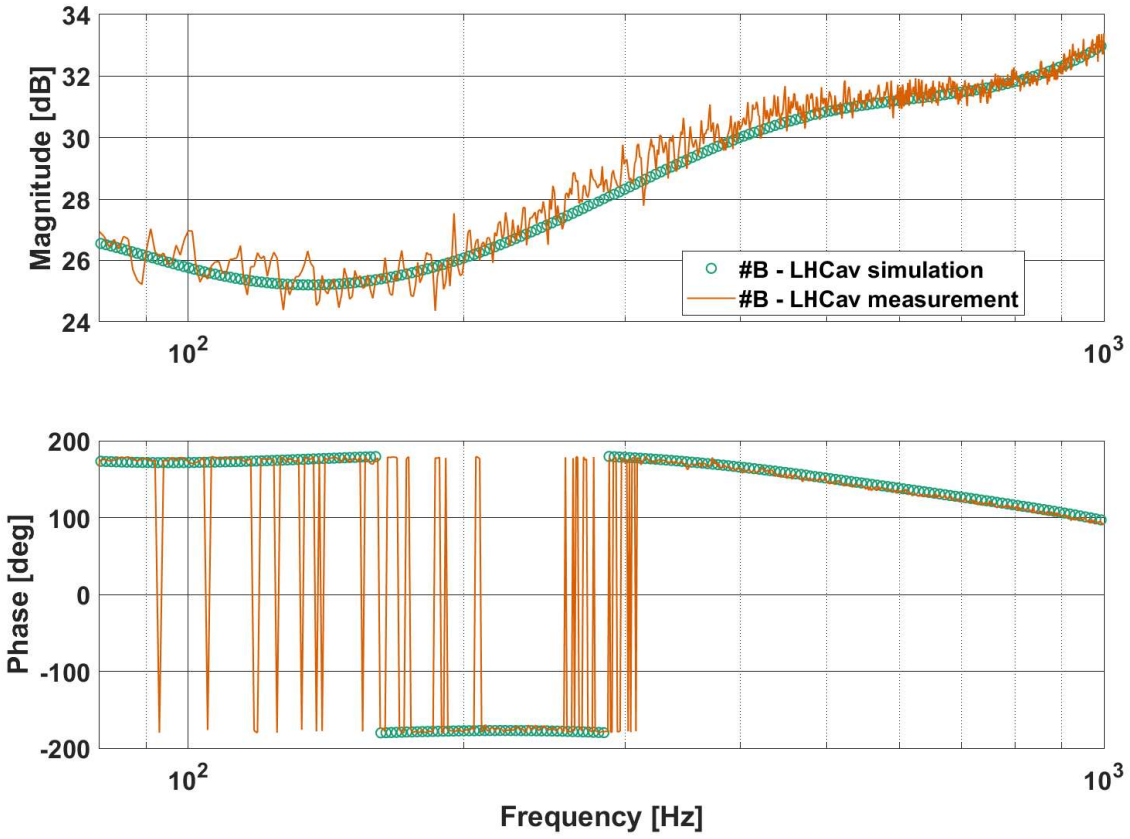

Figure 5.11: Bode plot of the measurement of the force exerted on the LTM from a force injected on the CTM for spring of 0.097γ induced in the left-hand cavity. Orange is the measurement, green is the simulation. The measurement when the left-hand cavity is held at its optical resonance is not shown in Figure 5.11 as this was measured on a different day where a corresponding measurement with no detuning was not taken.

5.4.2 Left-Hand Cavity Measurements of Springs and Anti-Springs

In order to get negative inertia or optical trapping it is required to have a spring and an anti-spring in the left-hand cavity. The measurements for this more complicated system are presented in Figures 5.13, 5.16, 5.19, 5.14, 5.17, 5.20, 5.15, 5.18, and 5.21 as a series of Bode plots similar to Figure 5.7. In each case a spring was created through detuning the left-hand cavity, and an anti-spring was created by detuning the phase-locking loop local oscillator close to the centre of the primary laser resonance to create an anti-spring. Each simulation was fitted to the measurement as before by changing the overall scalar gain applied to the cavity in the simulation.

Figure 5.12 shows the detuning of the springs ($\delta_A, \delta_B, \delta_C$) and anti-springs ($\delta_1, \delta_2, \delta_3$) used in

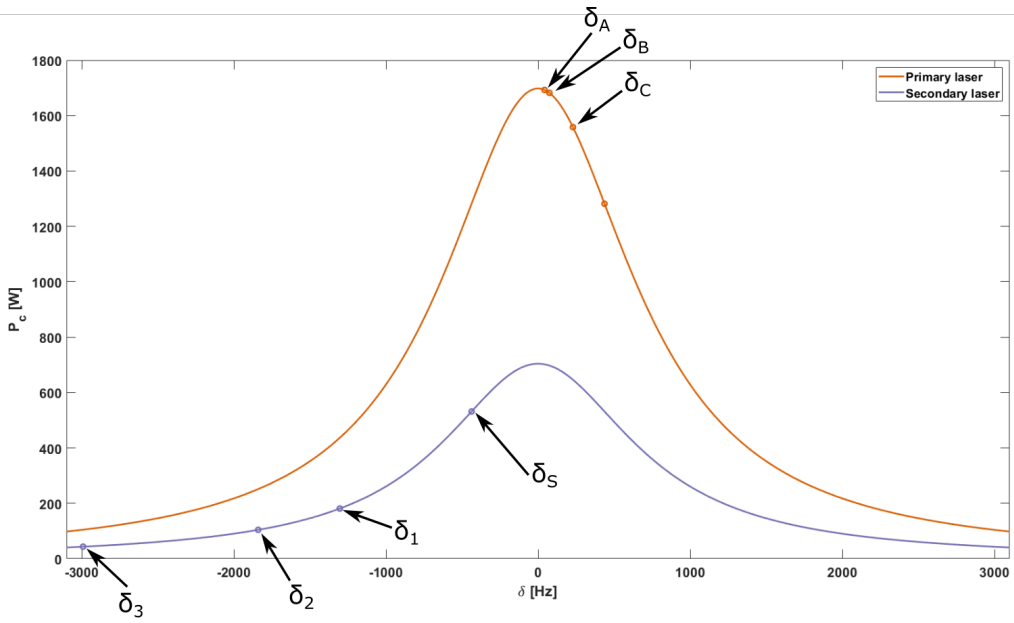

Figure 5.12: Diagram showing the relative detunings applied during the measurement set. 0 Hz on the x-axis is the centre of the primary laser resonance, and the orange curve shows how the circulating power of the primary laser in the cavity changes as the cavity frequency is changed. The purple curve shows how the circulating power of the secondary laser changes as this laser frequency is detuned from the primary laser. $\delta_A, \delta_B, \delta_C$ are the spring detunings used and $\delta_1, \delta_2, \delta_3$ are the anti-spring detunings used, expressed in terms of γ, the half-linewidth of the cavity. δ_S is the point on the resonance curve at which the detuning reaches 0.57γ and the rigidity or anti-rigidity is strongest.

these measurements. $\delta_A = 0.056\gamma$, $\delta_B = 0.097\gamma$, $\delta_C = 0.30\gamma$, $\delta_1 = 1.7\gamma$, $\delta_2 = 2.4\gamma$ and $\delta_3 = 3.9\gamma$. The point $\delta_S = 0.57\gamma$ on each curve is where the most rigid or anti-rigid point resides, and therefore where the damping part of the spring constant is lowest in magnitude (see

Figure 2.2 and [3]). The graphs of CTM to LTM measurements in Figures 5.13, 5.16, 5.19,

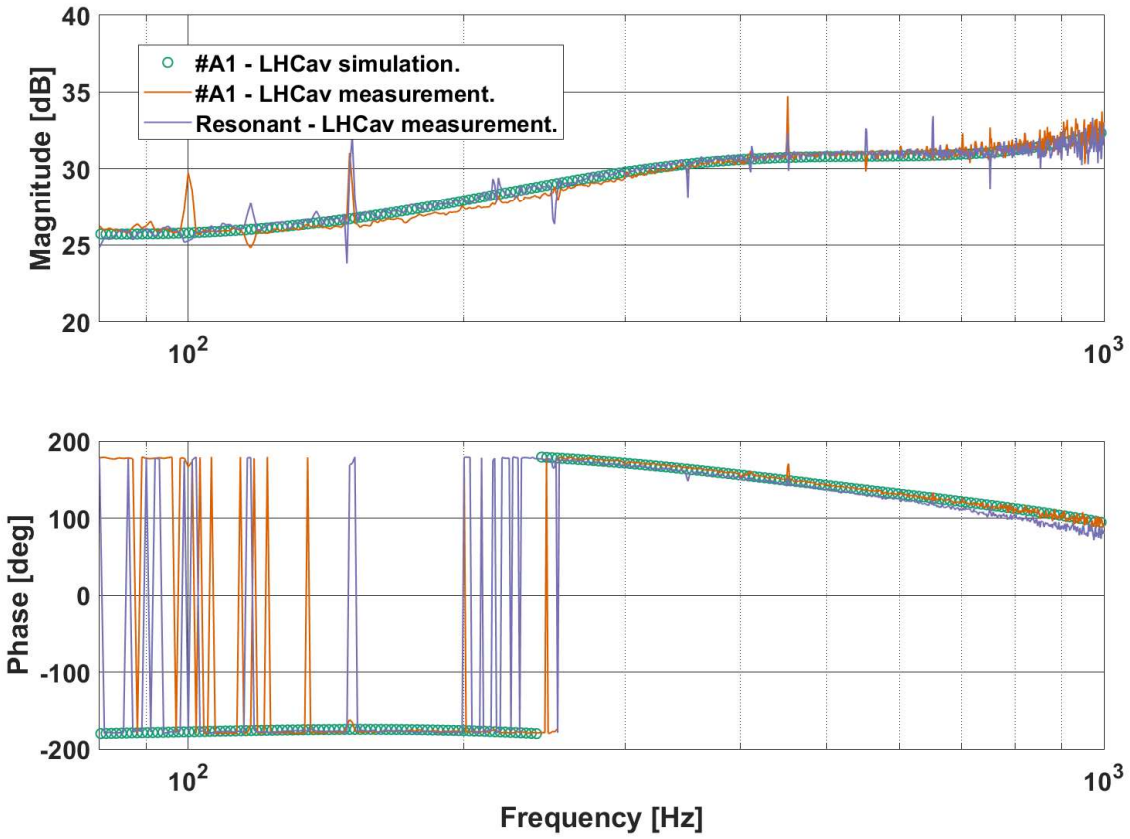

Figure 5.13: Force exerted on the LTM divided by the force injected on the CTM, for a spring of 0.056γ and an anti-spring of 1.7γ. Orange is the measurement, green is the corresponding simulation, and the purple line is the measurement when the left-hand cavity is held at its optical resonance for comparison, from Figure 5.7.

5.14, 5.17, 5.20, 5.15, 5.18, and 5.21 are again organised using the alphanumeric code in Table 5.2. Note that the anti-springs are all in the region over one linewidth where the damping terms and rigidity terms are non-linear, and the lower power makes the optomechanical effect weaker. The spring detunings are all closer to resonance with a higher power carrier and so will have a larger effect on cavity dynamics. The measurements with the strongest spring (Figures 5.19 , 5.20 and 5.21) show a reduction compared to the resonance measurement below 300 Hz. Looking at predictions of the resonant frequencies f_r of these combinations given in Table 5.2, from calculations based on the spring constant equation in [1], Figures 5.19 , 5.20 and 5.21 have resonant frequencies between 200 and 300 Hz. Below this frequency, if the spring is dominant, the restoring force reduces the force needed from the servo to stabilise the cavity length, causing

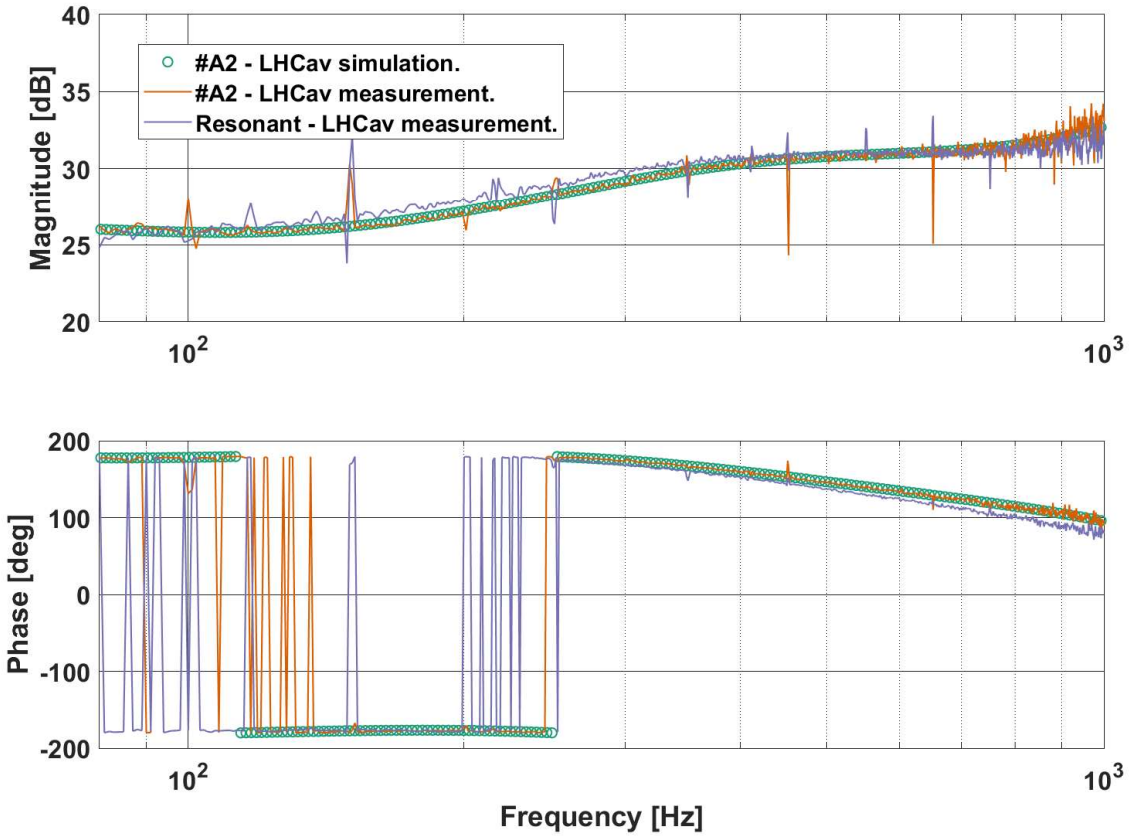

Figure 5.14: Force exerted on the LTM divided by the force injected on the CTM, for a spring of 0.056γ and an anti-spring of 2.4γ. Orange is the measurement, green is the corresponding simulation and the purple line is the measurement when the left-hand cavity is held at its optical resonance for comparison, from Figure 5.7.

Code	Spring δ	Anti-spring δ	f_r	Figure Numbers
A1	0.056γ	1.7γ	25.5 Hz	5.13, 5.23
A2	0.056γ	2.4γ	102 Hz	5.14, 5.24
A3	0.056γ	3.9γ	130 Hz	5.15, 5.25
B1	0.097γ	1.7γ	114 Hz	5.16, 5.26
B2	0.097γ	2.4γ	150 Hz	5.17, 5.27
B3	0.097γ	3.9γ	169 Hz	5.18, 5.28
C1	0.30γ	1.7γ	233 Hz	5.19, 5.29
C2	0.30γ	2.4γ	246 Hz	5.20, 5.30
C3	0.30γ	3.9γ	256 Hz	5.21, 5.31

Table 5.2: Resonant frequencies for spring/anti-spring combinations used in measurements for which the detunings are listed in Section 5.4.1. Resonant frequencies were calculated from the spring constant equation in [1].

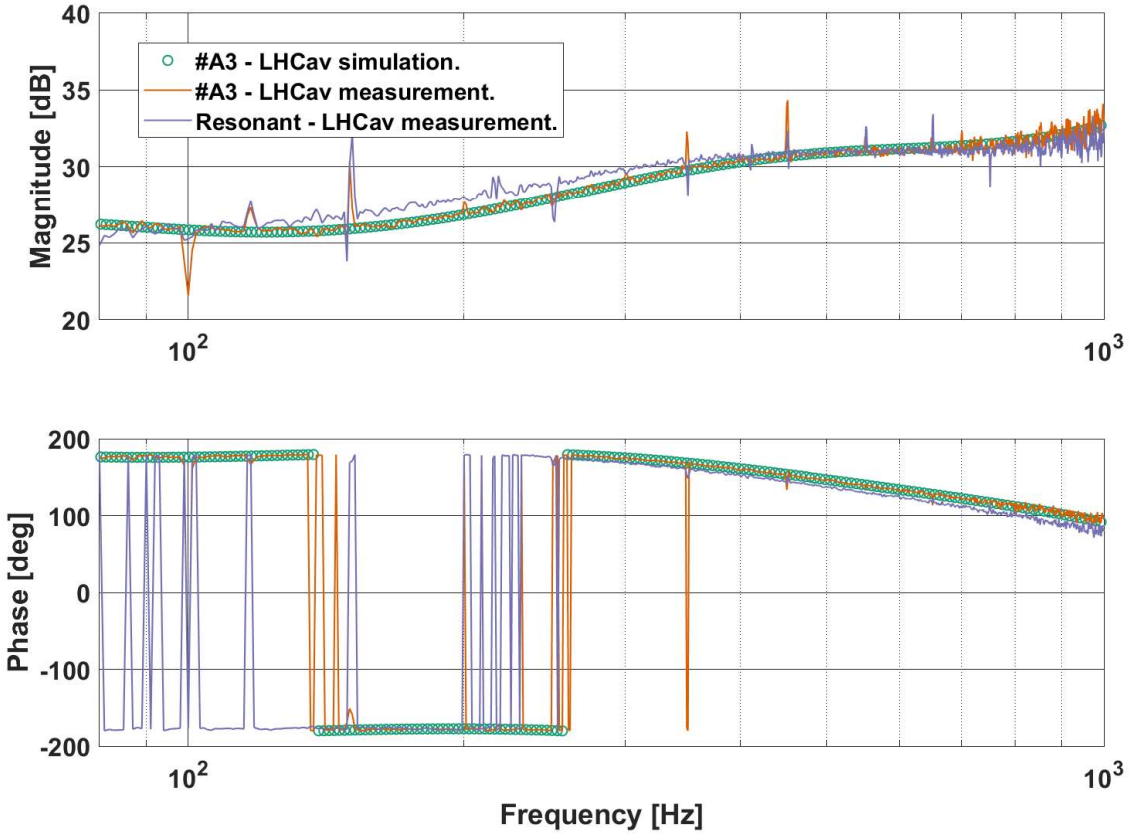

Figure 5.15: Force exerted on the LTM divided by the force injected on the CTM, for a spring of 0.056γ and an anti-spring of 3.9γ. Orange is the measurement, green is the corresponding simulation and the purple line is the measurement when the left-hand cavity is held at its optical resonance for comparison, from Figure 5.7.

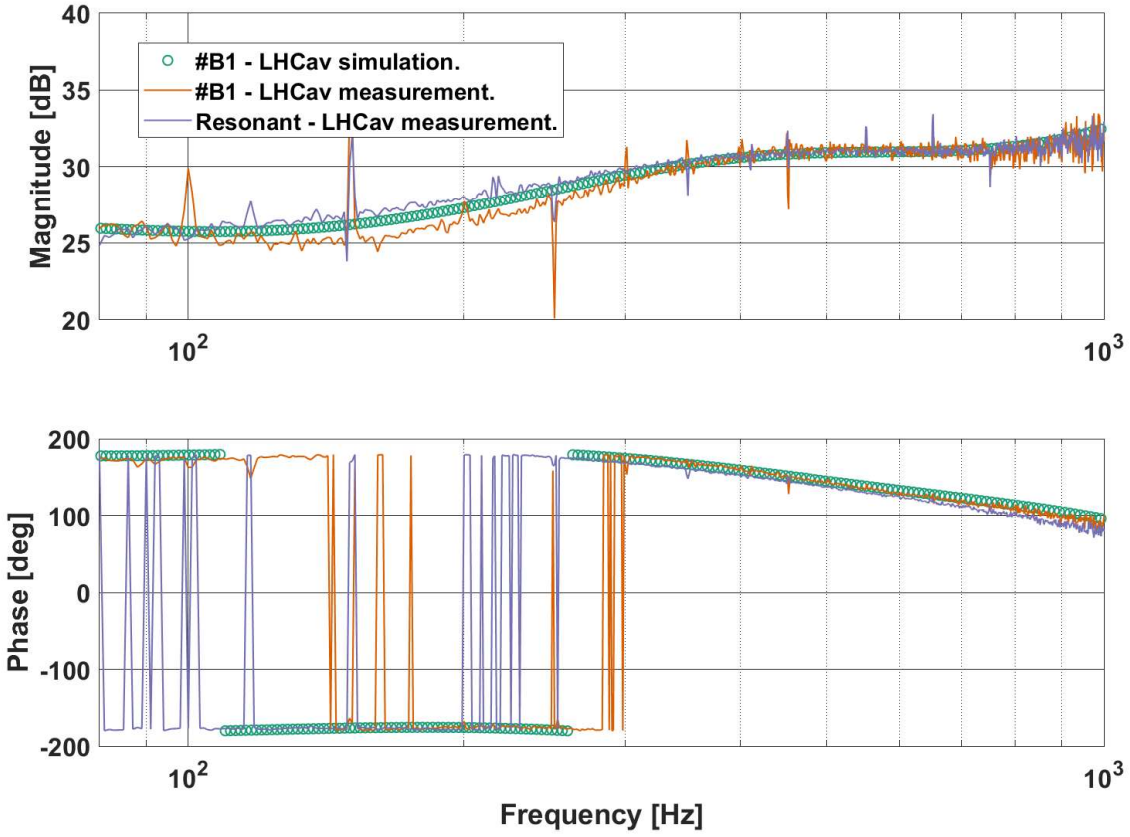

Figure 5.16: Force exerted on the LTM divided by the force injected on the CTM, for a spring of 0.097γ and an anti-spring of 1.7γ. Orange is the measurement, green is the corresponding simulation, and the purple line is the measurement when the left-hand cavity is held at its optical resonance for comparison, from Figure 5.7.

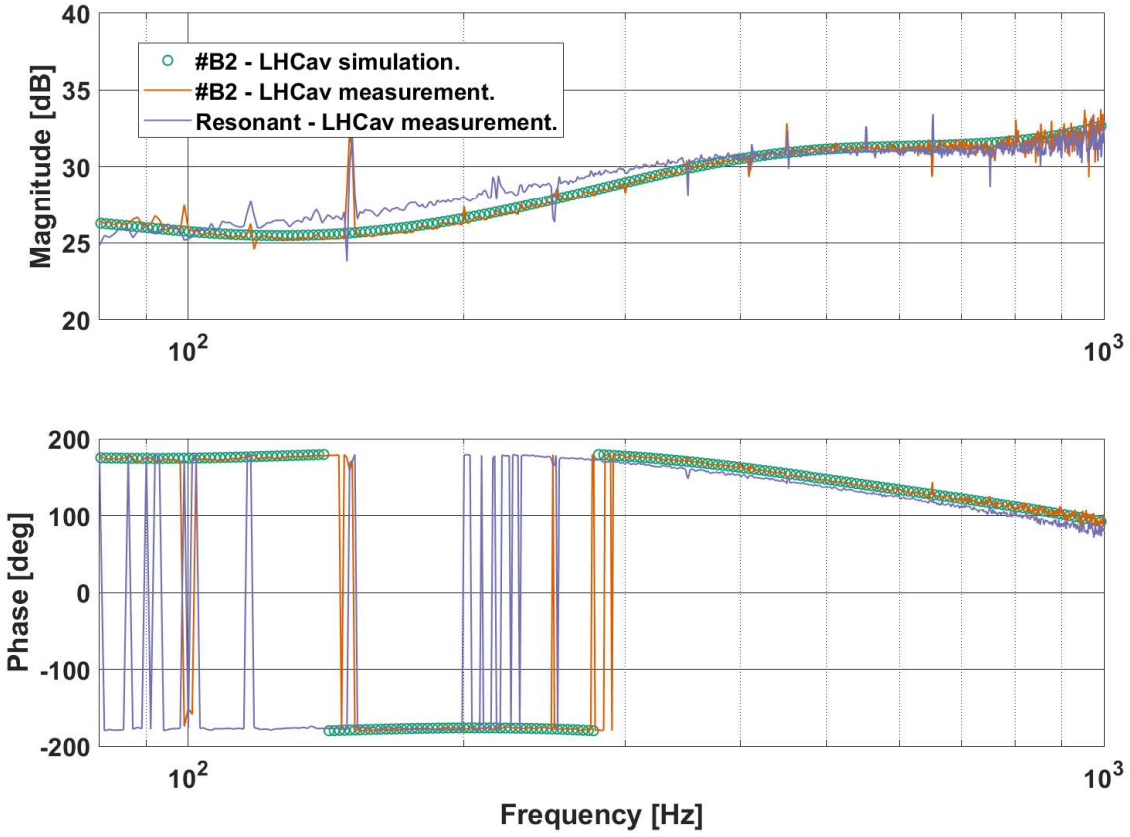

Figure 5.17: Force exerted on the LTM divided by the force injected on the CTM, for a spring of 0.097γ and an anti-spring of 2.4γ. Orange is the measurement, green is the corresponding simulation and the purple line is the measurement when the left-hand cavity is held at its optical resonance for comparison, from Figure 5.7.

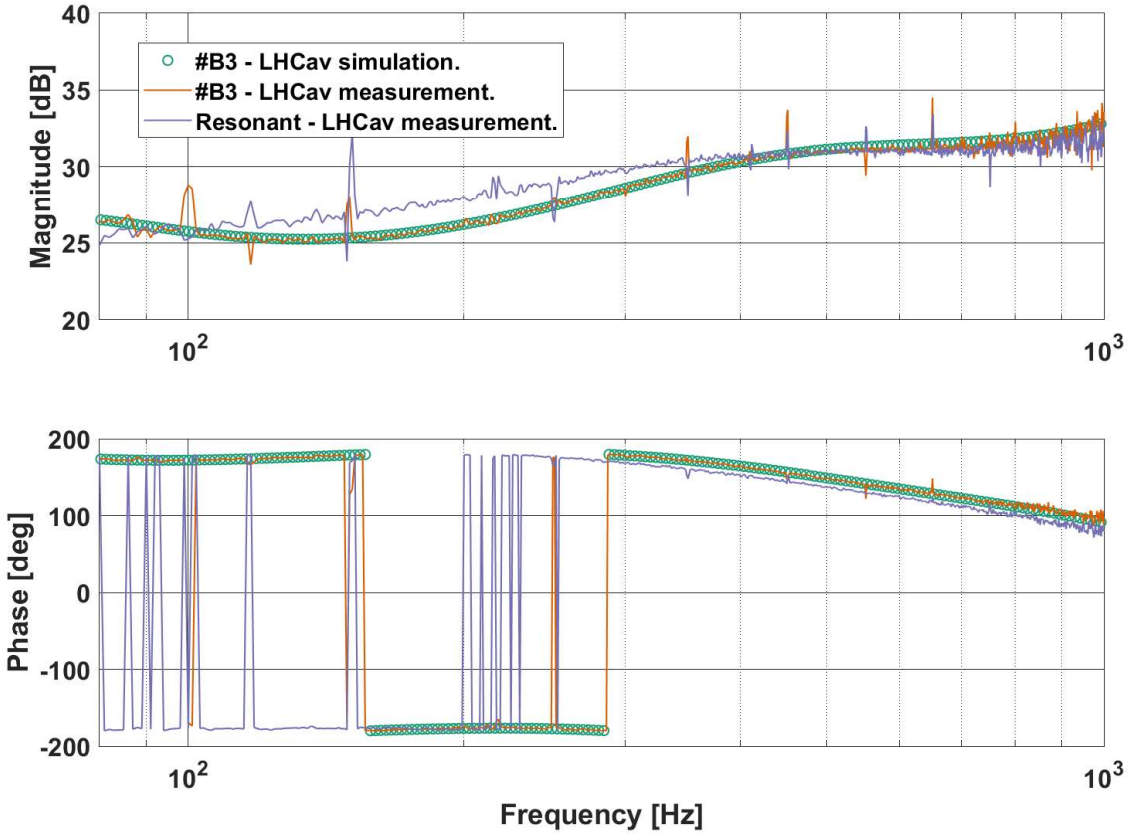

Figure 5.18: Force exerted on the LTM divided by the force injected on the CTM, for a spring of 0.097γ and an anti-spring of 3.9γ. Orange is the measurement, green is the corresponding simulation and the purple line is the measurement when the left-hand cavity is held at its optical resonance for comparison, from Figure 5.7.

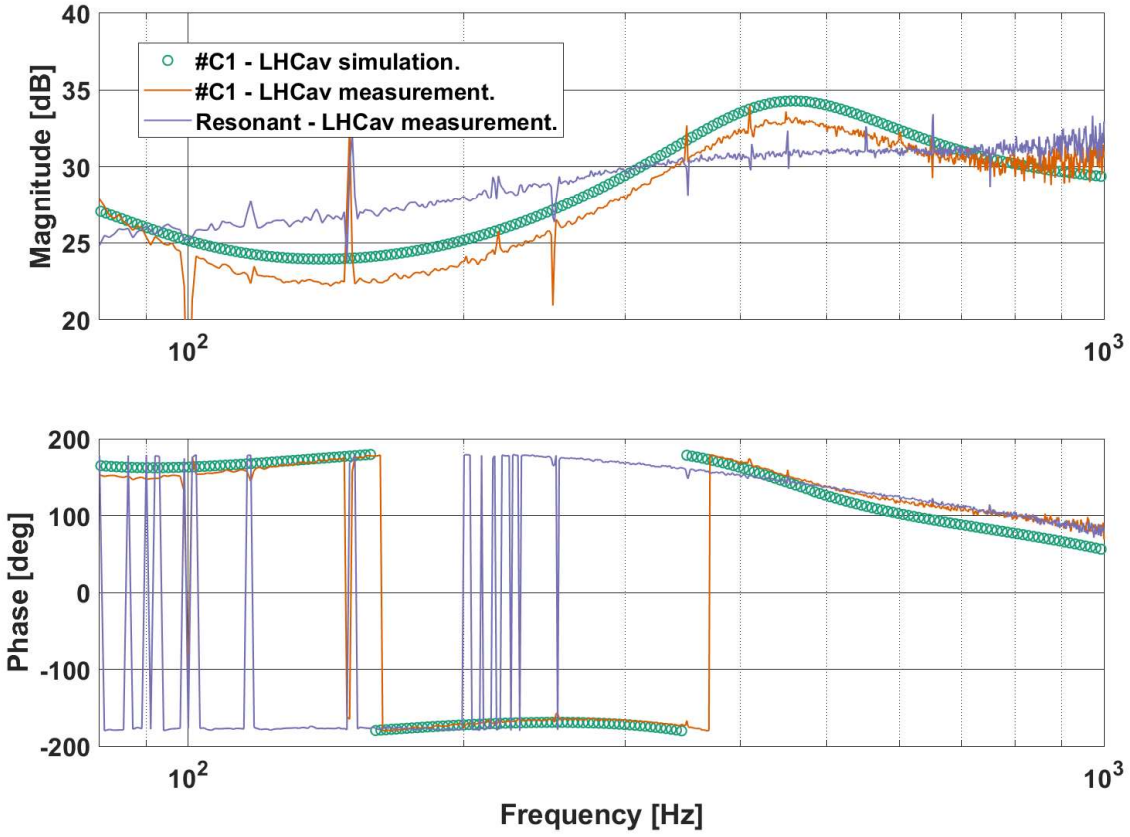

Figure 5.19: Force exerted on the LTM divided by the force injected on the CTM, for a spring of 0.30γ and an anti-spring of 1.7γ. Orange is the measurement, green is the corresponding simulation, and the purple line is the measurement when the left-hand cavity is held at its optical resonance for comparison, from Figure 5.7.

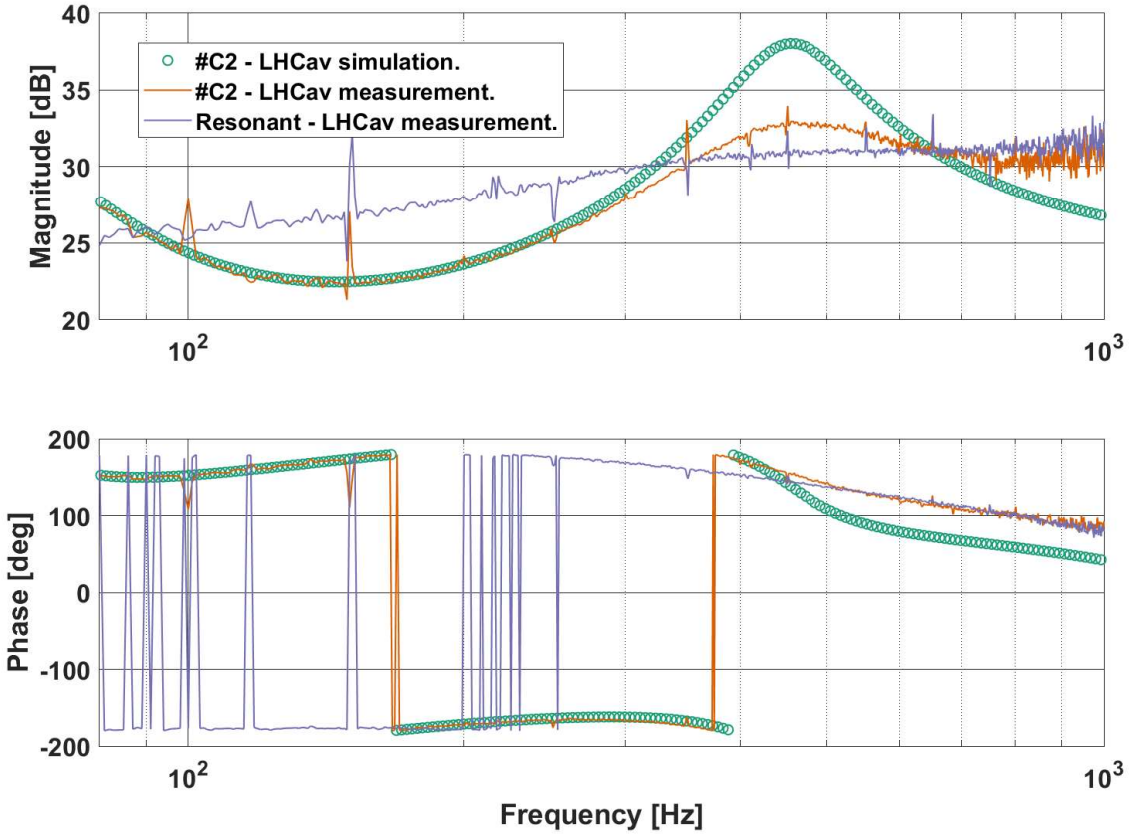

Figure 5.20: Force exerted on the LTM divided by the force injected on the CTM, for a spring of 0.30γ and an anti-spring of 2.4γ. Orange is the measurement, green is the corresponding simulation and the purple line is the measurement when the left-hand cavity is held at its optical resonance for comparison, from Figure 5.7.

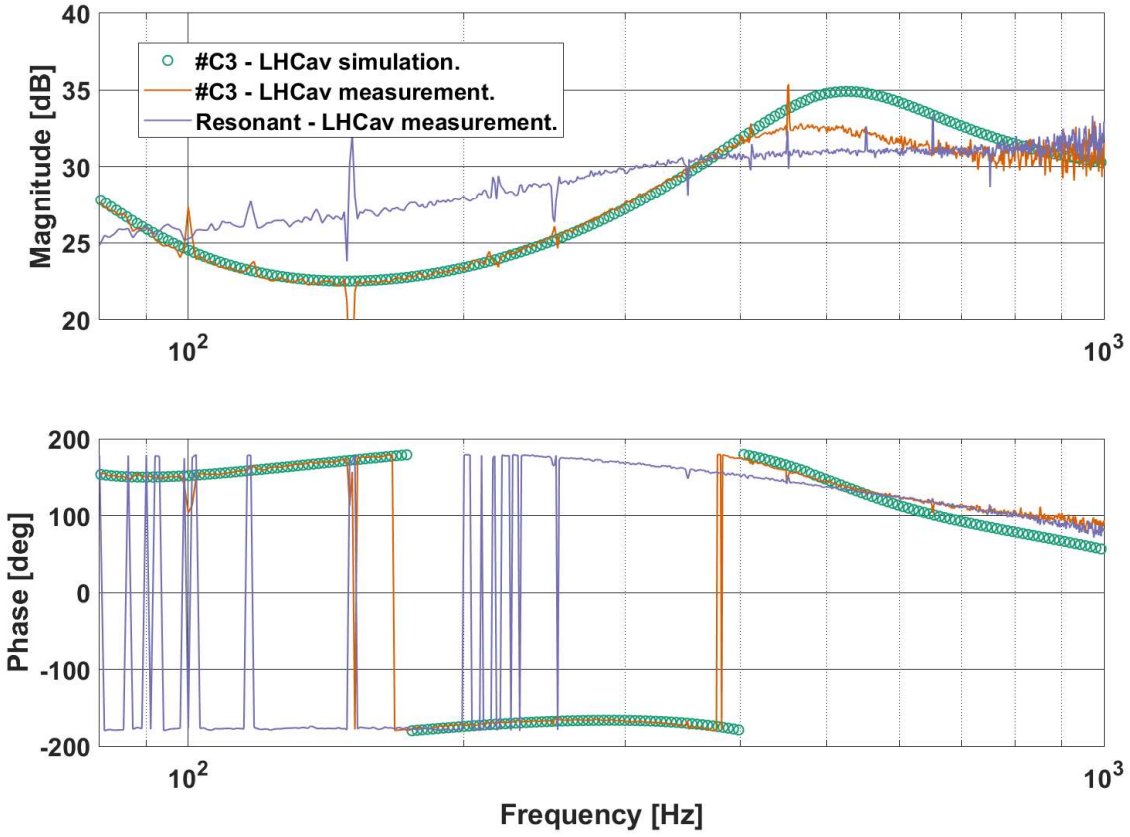

Figure 5.21: Force exerted on the LTM divided by the force injected on the CTM, for a spring of 0.30γ and an anti-spring of 3.9γ. Orange is the measurement, green is the corresponding simulation and the purple line is the measurement when the left-hand cavity is held at its optical resonance for comparison, from Figure 5.7.

a peak in the magnitude of the measurement at around 450 Hz as the spring brings the systems closer to instability. At higher frequencies, the magnitude falls off near 1 kHz as both the spring response and cavity response decrease. At the lowest end of the measurement range, the magnitude of these three measurements curves up towards lower frequencies around 100 Hz as the integration in the servo is overwhelming the spring suppression effect.

The other measurements (Figures 5.13, 5.16, 5.14, 5.17, 5.15, 5.18) show a reduction in relation to the resonance measurement at frequencies below 300 Hz, but not a corresponding peak between 400 and 500 Hz. This is thought to be because the springs used are weaker and so do not overwhelm the damping provided by the anti-spring and servo to the same extent.

Looking at the simulated curves in green, it can be seen that while the match is very good for Figures 5.14, 5.17, 5.15 and 5.18, for the most highly detuned springs (Figures 5.19, 5.20, 5.21), the prediction is not the right shape above 400 Hz. For the anti-springs closest to resonance (Figures 5.13, 5.16, 5.19), the simulated curve does not match the measurement below 400 Hz. This suggests that there is some fault in the way the simulation predicts damping and rigidity for springs and anti-springs. Since the spring is well calibrated in this simulation, it can be assumed the fault is in the combination of anti-springs with springs or in the way the anti-spring is set-up in the simulation.

5.4.3 Looking for Negative Inertia and Trapping Using the Right-Hand Cavity

In the CTM to LTM measurements discussed it is difficult to determine the presence of negative inertia. The cavity servo overwhelms the smaller detuning measurements shown in Figures 5.13, 5.16, 5.14, 5.17, 5.15 and 5.18 at frequencies around 500 Hz. Also, in Figures 5.19, 5.20 and 5.21 the cavity servo shapes the measurement below 100 Hz, confirming the decision made to

use the 'local readout' technique mentioned in Sub-section 5.3. As the right-hand cavity servo has a flatter servo profile in the measurement region and a higher unity gain point, due to the lack of any spring effects in the cavity itself, it can be used as a good monitor for the left-hand cavity. This can be seen from Figure 5.22, which is the measurement taken on the servo output to the RTM when no springs are in the left-hand cavity (so it is held at the optical resonance) and a signal is injected on the CTM. The orange line is the measurement and the purple line is a moving average to show the overall shape. The simulation can be used to model the full system including the right-hand cavity but due to the limitations of the model of the left-hand cavity the mis-match (discussed above in Section 5.4.2) between simulated and measured springs will be carried forward to these right-hand cavity simulated measurements. Therefore it was decided to verify the final results from right-hand cavity measurements by using a theory-based argument to determine the presence of trapping and negative inertia.

The corresponding right-hand cavity plots for each spring/anti-spring case shown in Figures 5.13, 5.16, 5.19, 5.14, 5.17, 5.20, 5.15, 5.18, and 5.21 are laid out in Figures 5.23, 5.26, 5.29, 5.24, 5.27, 5.30, 5.25, 5.28, and 5.31. As in the left-hand cavity plots, orange is the measurement with optomechanics present in the left-hand cavity and purple is the measurement without optomechanics present in the left-hand cavity, that is the measurement with the left-hand cavity held at the optical resonance. These images again use the alpha-numeric code from Section 5.4.1 to denote the spring/anti-spring combinations used. The RTM measurements were simultaneously recorded with the corresponding LTM measurements.

In Figures 5.29, 5.24, 5.27, 5.30, 5.28 and 5.31, there seems to be excess motion observed in the detuned cases above about 400 Hz. As this is making the mass move more in relation to the force injected on the CTM, it can be considered to be reducing the inertia of the mass and thus providing negative inertia. In Figure 5.29, for example, the gain in the spring (orange) case between 400 and 700 Hz is larger relative to the gain of the resonant (purple) case. Around 500 Hz, near the maximum increase, the gain increases by a factor of 1.14 ± 0.25 dB from the purple to the orange case. Referring back to the equation for right-hand cavity measurements (5.7), if

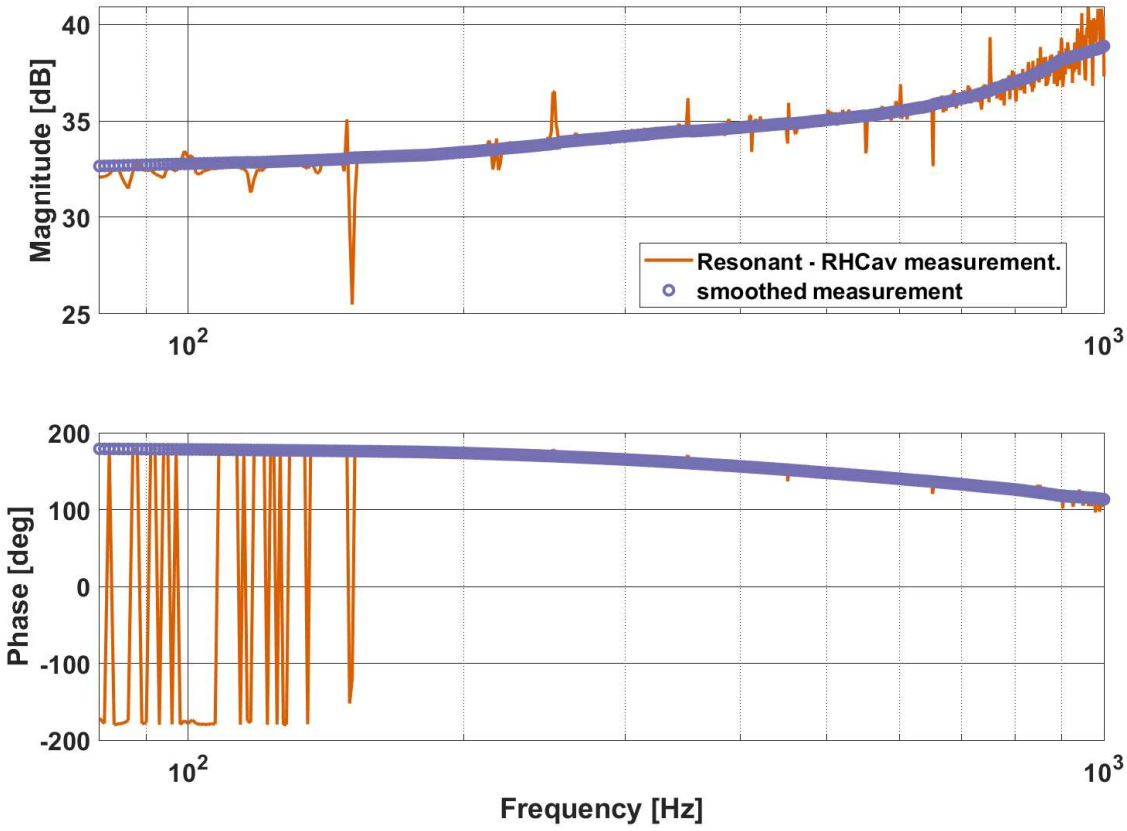

Figure 5.22: Bode plot of the measurement of the force exerted on the RTM from a force injected on the CTM, when the left-hand cavity is held at its optical resonance as there are no springs or anti-springs induced in the left-hand cavity. Orange is the measurement and the purple circles are a moving average of the measurement.

divided by the case with no spring detuning, the equation for the right-hand cavity measurement becomes

$$\frac{\mathrm{V_{out}}}{\mathrm{V_{in\ relative}}} = \frac{\left(\mathrm{C_L H_L P_L O_C} + 1 - \mathrm{P_L K_L}\right)}{\left(1 + \mathrm{C_L H_L P_L O_C} - \mathrm{K_L}\left(\mathrm{P_C} + \mathrm{P_L}\right)\right)}, \tag{5.9}$$

which represents the relative magnitude of the spring case (orange) compared to the resonant case (purple). The spring will affect the part of Equation 5.9 with the form $P_L K_L$ or similarly, $P_C K_L$. This part of the transfer function represents the open loop gain of the pendulum response in m/N multiplied by the spring response in N/m. As noted in [1], the open loop gain of an optical spring acting on a suspended mirror of mass, m, can be given as

$$\frac{-K_t}{m\Omega^2}. \tag{5.10}$$

If this is substituted into Equation (5.9), then

$$\frac{\mathrm{V_{out}}}{\mathrm{V_{in\ relative}}} = \frac{A\left(\Omega\right) + \frac{K_t}{m\Omega^2}}{A\left(\Omega\right) + \frac{2K_t}{m\Omega^2}} \tag{5.11}$$

is obtained, where

$$A\left(\Omega\right) = 1 + \mathrm{C_L H_L P_L O_C} \tag{5.12}$$

and K_t is the total optical spring constant in the cavity. From [5], the condition for negative inertia is $K_t = -m_{\mathrm{opt}}\Omega^2$. If the magnitude of Equation (5.11) is more than 1, it would imply that

$$K_t > 2K_t, \tag{5.13}$$

which means that the sign of K_t is negative. This partially fulfils the condition for negative inertia discussed in [4, 5], implying that there is negative inertia in Figure 5.29. The servo coupled through the spring could be causing some of this negative inertia effect as the region with possible negative inertia happens below the unity gain point of the left-hand cavity servo. As a result, and considering the fact that the K_t term appears on the numerator and denominator of Equation (5.11), it cannot be determined whether the negative inertia effect dominates the dynamics within any part of the measurement bandwidth.

In order to improve upon this in future experiments it would be of benefit to design cavities with a far larger difference in unity gain points, so that there was a large region observable by the right-hand cavity where the CTM was not noticeably changed by the left-hand cavity servo, and this inertia effect could be seen clearly.

In Figures 5.29, 5.30, and 5.31, there is suppression of CTM motion below 400 Hz, that is, the magnitude of the orange (spring) trace is below the purple (resonance) trace. This means that the mass is trapped by the coupled system of the optomechanics and servo in the left-hand cavity.

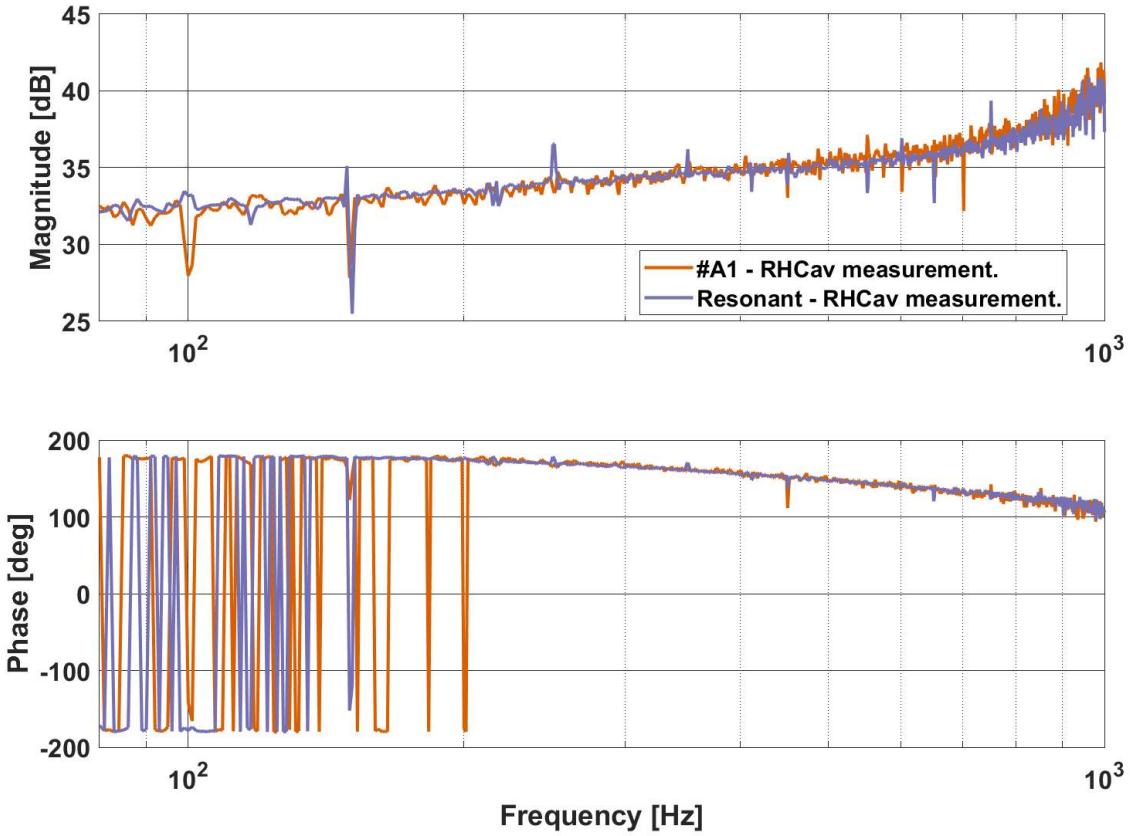

Figure 5.23: Bode plot of force exerted on the RTM from a force injected on the CTM, when a spring of 0.056γ and an anti-spring of 1.7γ is used in the left-hand cavity. Orange is the measurement and the purple line is the measurement when the left-hand cavity is held at its optical resonance for comparison, from Figure 5.22.

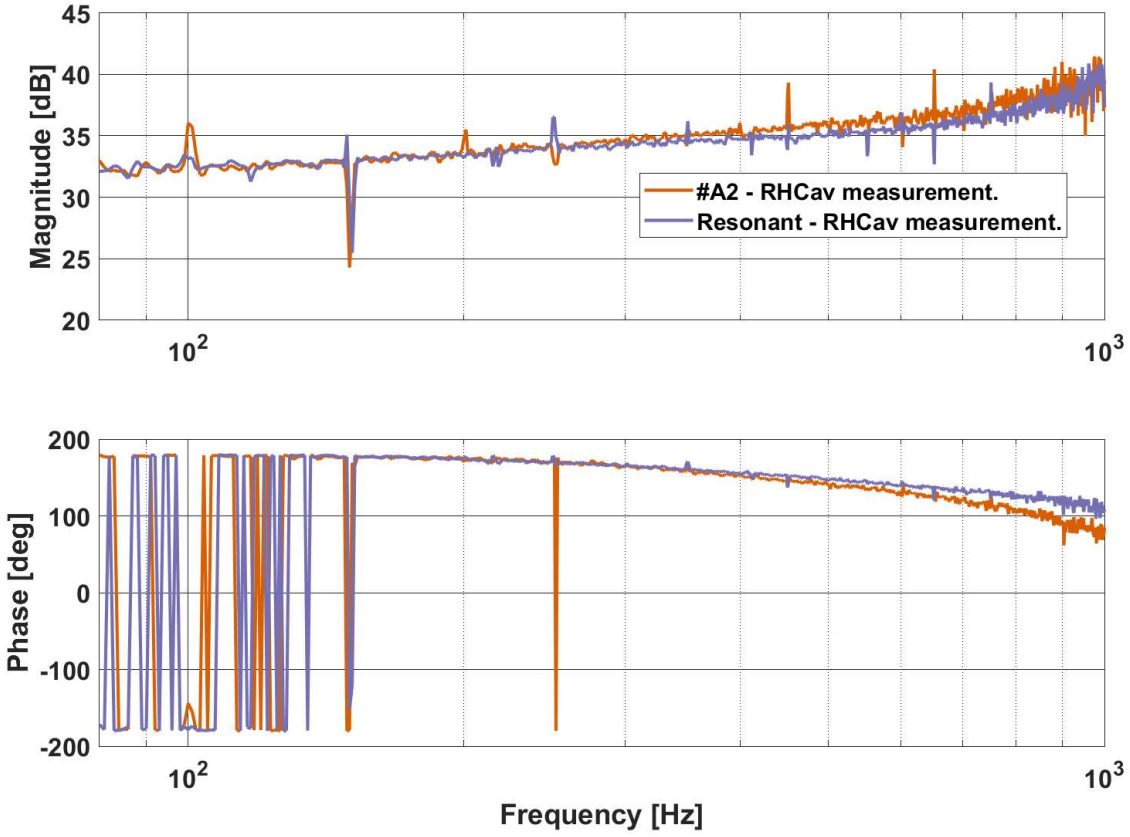

Figure 5.24: Bode plot of force exerted on the RTM from a force injected on the CTM, when a spring of 0.056γ and an anti-spring of 2.4γ is used in the left-hand cavity. Orange is the measurement and the purple line is the measurement when the left-hand cavity is held at its optical resonance for comparison, from Figure 5.22.

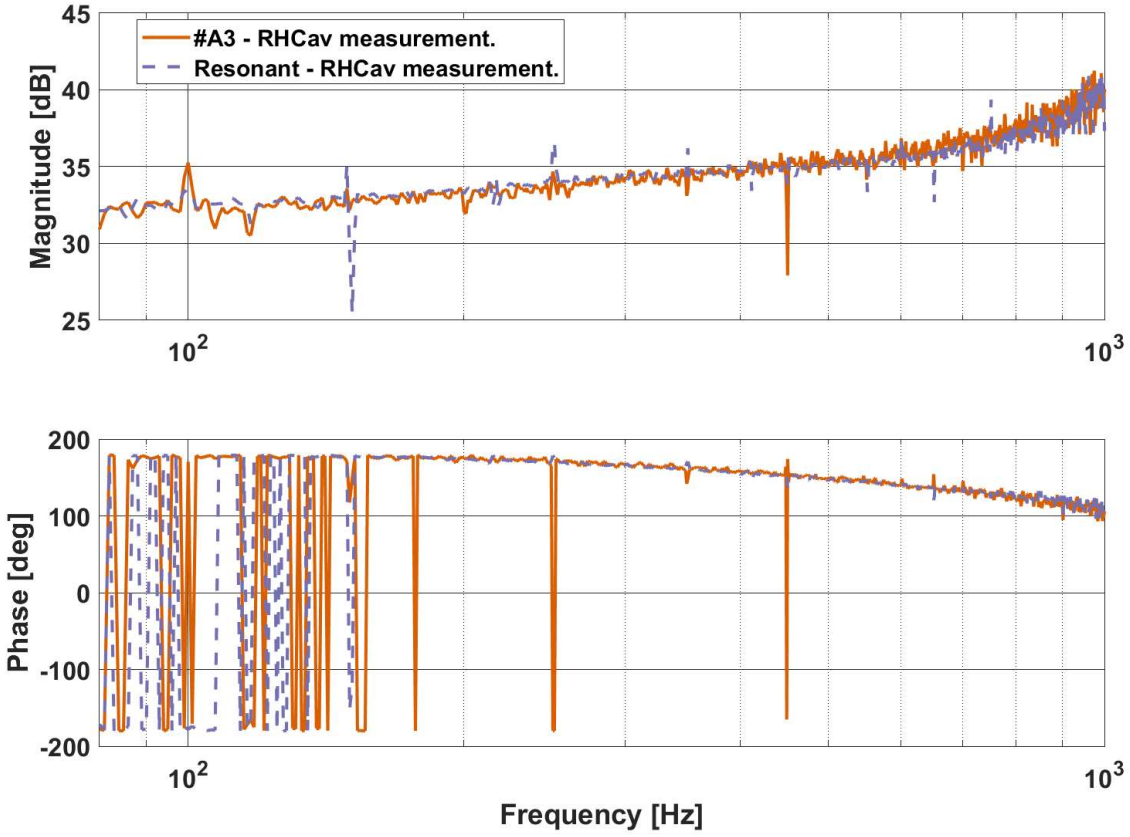

Figure 5.25: Bode plot of force exerted on the RTM from a force injected on the CTM, when a spring of 0.056γ and an anti-spring of 3.9γ is used in the left-hand cavity. Orange is the measurement and the purple line is the measurement when the left-hand cavity is held at its optical resonance for comparison, from Figure 5.22.

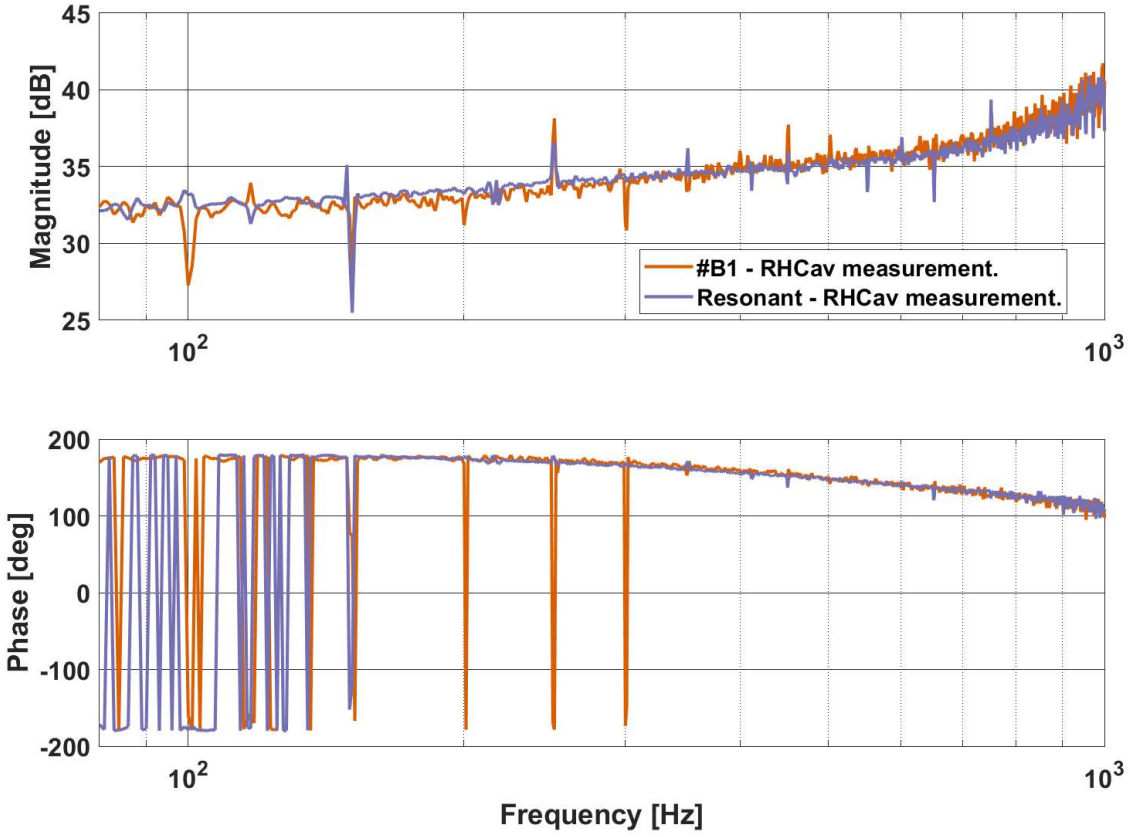

Figure 5.26: Bode plot of force exerted on the RTM from a force injected on the CTM, when a spring of 0.097γ and an anti-spring of 1.7γ is used in the left-hand cavity. Orange is the measurement and the purple line is the measurement when the left-hand cavity is held at its optical resonance for comparison, from Figure 5.22.

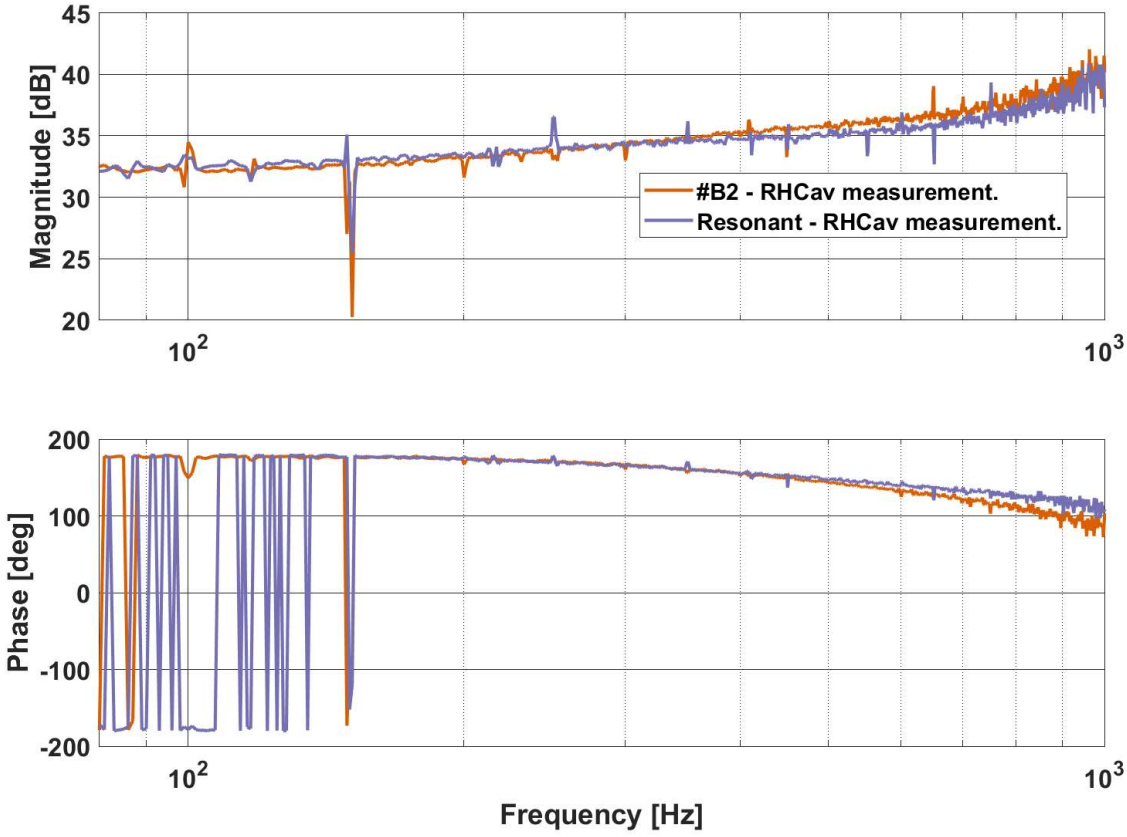

Figure 5.27: Bode plot of force exerted on the RTM from a force injected on the CTM, when a spring of 0.097γ and an anti-spring of 2.4γ is used in the left-hand cavity. Orange is the measurement and the purple line is the measurement when the left-hand cavity is held at its optical resonance for comparison, from Figure 5.22.

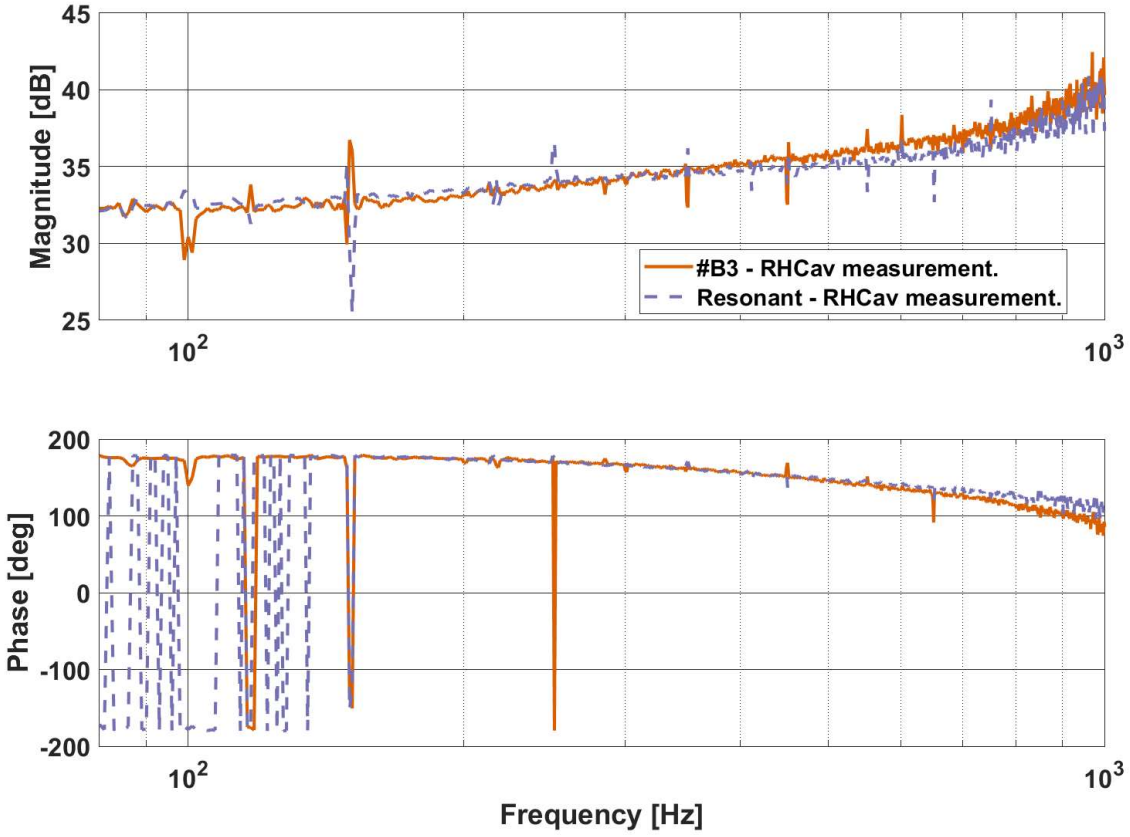

Figure 5.28: Bode plot of force exerted on the RTM from a force injected on the CTM, when a spring of 0.097γ and an anti-spring of 3.9γ is used in the left-hand cavity. Orange is the measurement and the purple line is the measurement when the left-hand cavity is held at its optical resonance for comparison, from Figure 5.22.

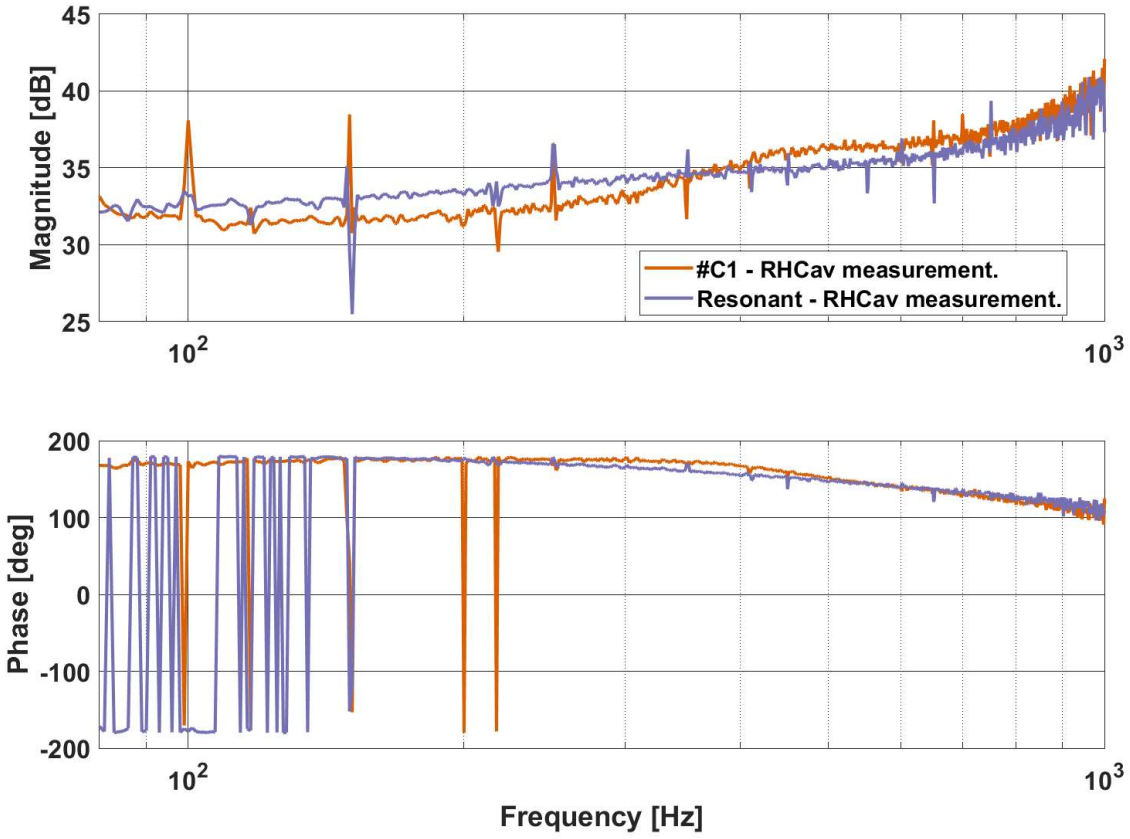

Figure 5.29: Bode plot of force exerted on the RTM from a force injected on the CTM, when a spring of a spring of 0.30γ and an anti-spring of 1.7γ is used in the left-hand cavity. Orange is the measurement and the purple line is the measurement when the left-hand cavity is held at its optical resonance for comparison, from Figure 5.22. At 500 Hz the measurement with springs present in the left-hand cavity is 1.14 ± 0.25 dB in magnitude above the measurement with the left-hand cavity held on resonance, showing evidence of negative inertia.

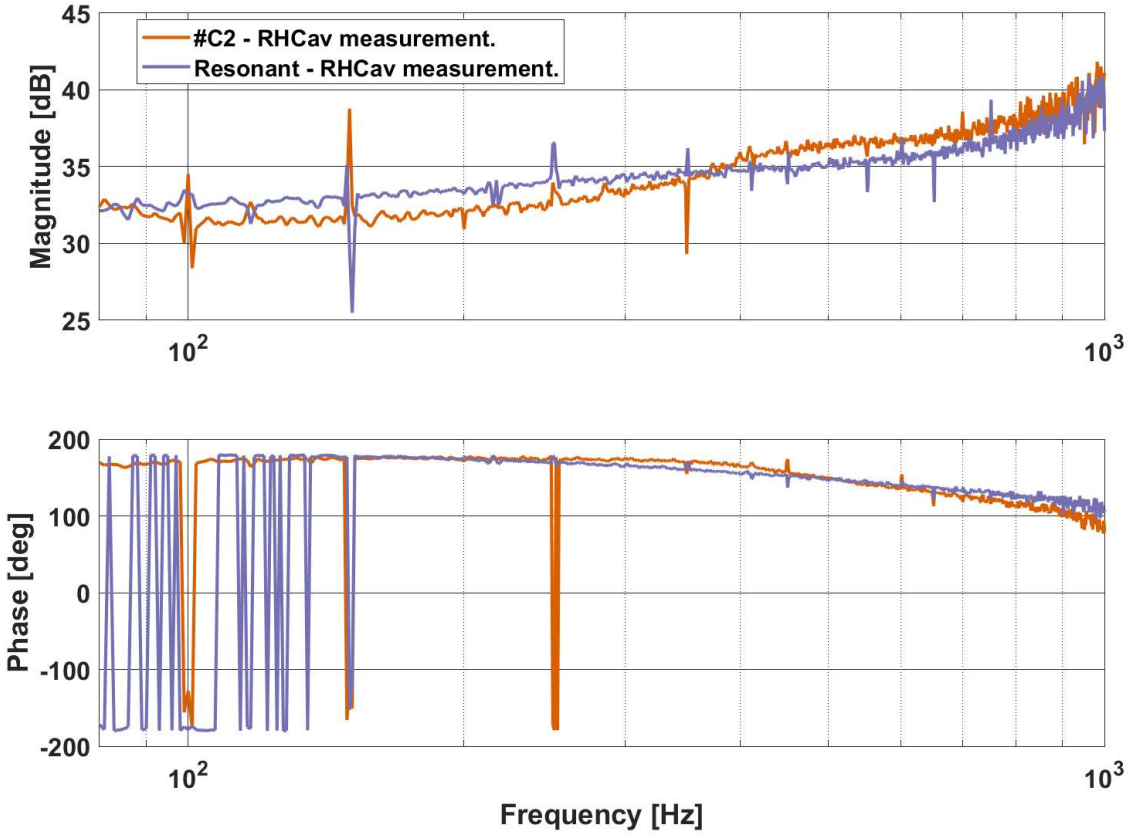

Figure 5.30: Bode plot of force exerted on the RTM from a force injected on the CTM, when a spring of 0.30γ and an anti-spring of 2.4γ is used in the left-hand cavity. Orange is the measurement and the purple line is the measurement when the left-hand cavity is held at its optical resonance for comparison, from Figure 5.22.

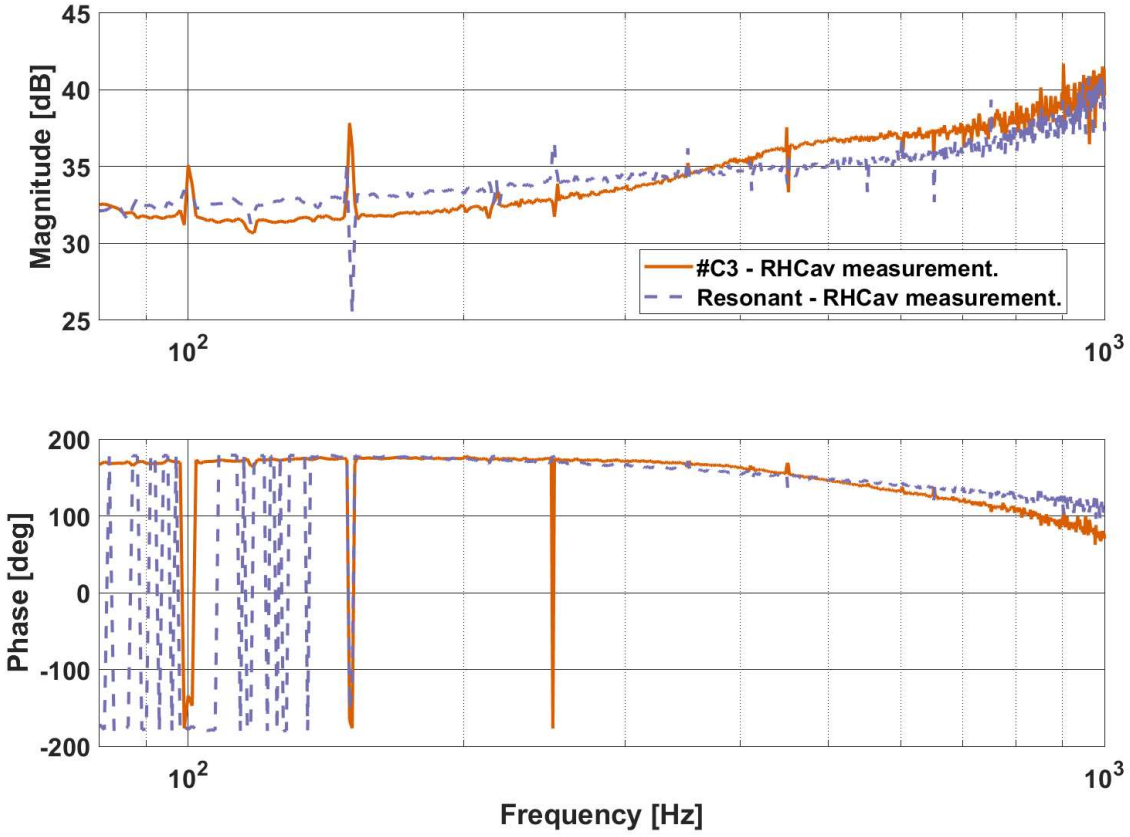

Figure 5.31: Bode plot of force exerted on the RTM from a force injected on the CTM, when a spring of 0.30γ and an anti-spring of 3.9γ is used in the left-hand cavity. Orange is the measurement and the purple line is the measurement when the left-hand cavity is held at its optical resonance for comparison, from Figure 5.22.

Chapter 6

Conclusion

Alteration of the existing two-cavity optical spring experiment at Glasgow was carried out to include the addition of a second carrier laser. The second resonant cavity in the system was altered in finesse to allow it to be used as a sensing cavity for the modification of the high finesse cavity mechanics by optical springs. The frequency control of the primary laser was altered to use a small 10 cm cavity as a frequency reference, and the second laser's frequency was controlled by a phase-locked loop with reference to the primary laser frequency.

Both cavities were set up to use the primary laser as a frequency reference, and the high finesse cavity was calibrated by using it to create a range of optical springs whose response matched simulations of the system carried out in Optickle. Double spring anti-spring systems were created using the high finesse cavity and the second laser, and these were found to have a close match with simulation for some detunings, despite deviating at higher detunings.

It was found possible to use the system to create optical traps with some of these combinations, with the spring providing the restoring force between 100 Hz and 300 Hz and the electronics, the restoring force at higher and lower frequencies. Limitations due to the high noise at low frequency prevented the optical spring being used to keep the system stable below 100 Hz. Specifically, the seismic isolation design used in the frequency noise control caused noise peaks in the range between 10 and 80 Hz where there would have been interesting spring dynamics accessible

by the experiment. The environmental noise of the air conditioning system also provided large noise peaks in this range. By far the biggest limiting source for trapping measurements was the high level of integration needed up to 100 Hz which masked some of the trapping effects that the experiment was trying to measure. Future work would redesign the control system and experiment so less gain was needed at low frequency as attempts to lessen the low frequency servo gain and measure spring/anti-spring systems did not work due to high low frequency noise causing the lock to drift.

The phenomenon of negative inertia was investigated through a sequence of different spring anti-spring detunings. Evidence of negative inertia was found in the region between 500 Hz and 700 Hz; where one measurement showed a gain increase of 1.14 ± 0.25 dB relative to the same measurement with no springs present. However, for a complete analysis of this phenomenon more sensitive experimental searches for this effect are required. Further work would involve trying different combinations of power in each carrier for each detuning example, as this would allow greater optimisation of both the negative inertia and trapping effect, which was not carried out in the present system due to time constraints.

Another limitation on the negative inertia measurements specifically, was the fact that the bandwidth of the high finesse cavity fell within the measurement range in which springs were created, unlike the examples considered in [4, 5], where the rigidity, inertia and damping of the optical system can be treated as a linear sum allowing for complete or partial cancellation of the inertia. To improve this it would be necessary to use a system with two different linewidths for each laser frequency, meaning the damping of each could be precisely tuned, as discussed in the examples given in [4, 5]. Further work would also involve trying different combinations of power in each carrier for each detuning example, as this would allow greater optimisation of the negative inertia effect, which was not carried out in the present system due to time constraints.

Appendix A

Equations Relevant to Optical Spring Experiments

A.1 Define Cavity Properties

Define the reflectivity and transmissivity of a mirror in terms of the power coefficients, R and T. These are the squares of the corresponding coeffients, r and t; for light amplitude in reflection from, and transmission through, a mirror. This is shown in

$$R = r^2 \tag{A.1}$$

and

$$T = t^2. \tag{A.2}$$

If there is no additional loss associated with the mirror then

$$R + T = 1 \tag{A.3}$$

is true. This will be assumed for the rest of this appendix.

A Fabry-Perot resonant cavity is shown in figure A.1. It has input mirror, M1, and an end mirror, M2, which are a length, L, apart. a_0 is the initial laser field before the cavity, a_r is the total field

reflected from the cavity, and a_t is the total field transmitted by the cavity. M1 has an amplitude transmission coefficient of t_1 and a reflection coefficient of r_1. M2 has amplitude transmission and reflection coefficients of t_2 and r_2, respectively. To take account for the phase change when a wave reflects from a mirror, every reflection off the back (outside) surfaces of both mirrors introduces a factor of -1 in amplitude.

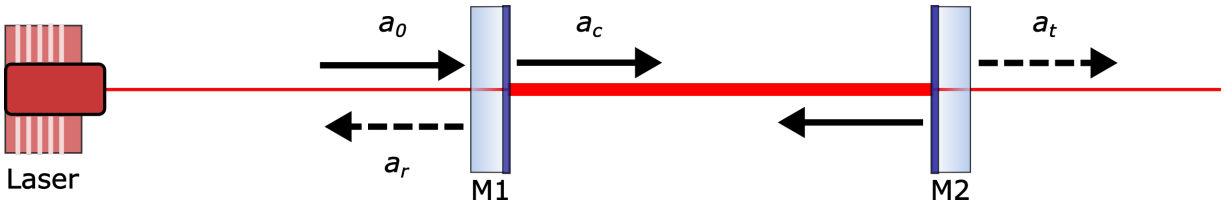

Figure A.1: Fabry-Perot Cavity pumped by laser from behind input mirror M1. Input beam shown as thin red line. Light builds up between M1 and the end mirror, M2; shown in diagram by thicker red line.

A.2 Phase Change of Cavity

The phase in radians of a resonant cavity relative to the resonance frequency of the pumping laser is defined as δ

$$\delta = \frac{2\pi\nu L}{c}. \tag{A.4}$$

Where ν is the pumping laser frequency and L is the resonant cavity length.

A.3 Transmission Through a Cavity

It is possible to write the transmitted field through a Fabry-Perot cavity, a_t as a sum of terms, where each term in the series has completed one additional round trip of the cavity. Each round trip contributes a factor of $r_2 r_1 \exp(-2i\delta)$. In (A.5) this is written to show the common factor of $t_1 t_2 \exp(-i\delta)$ the field picks up from its transmission through M1 and M2.

$$\begin{aligned} a_t &= a_0 \left[t_1 t_2 \exp(-i\delta) + t_1 r_2 r_1 t_2 \exp(-3i\delta) + \cdots + t_1 \left(r_2 r_1\right)^n t_2 \exp(-(2n+1)\, i\delta) \right] \\ &= a_0 t_1 t_2 \exp(-i\delta) \sum_{l=0}^{\infty} \left[\left(r_2 r_1\right)^l \exp(-2li\delta) \right] \end{aligned} \tag{A.5}$$

The sum in (A.5) contains the binomial expansion [74] for $\left(1 - r_2 r_1 \exp\left(-2i\delta\right)\right)^{-1}$. Substituting this gives equation

$$a_t = \frac{a_0 t_1 t_2 \exp\left(-i\delta\right)}{1 - r_2 r_1 \exp\left(-2i\delta\right)}. \tag{A.6}$$

To obtain the power transmitted through the cavity, multiply the transmitted field by its complex conjugate,

$$I_t = a_t a_t^*. \tag{A.7}$$

This gives equation (A.8) after simplification:

$$\begin{aligned} I_t &= \left(\frac{a_0^2 t_2^2 t_1^2 \left(\exp\left(-i\delta\right) - r_1 r_2 \exp\left(i\delta\right)\right)\left(\exp\left(i\delta\right) - r_1 r_2 \exp\left(-i\delta\right)\right)}{\left(1 + R_1 R_2 - 2 r_1 r_2 \cos\left(2\delta\right)\right)^2} \right) \\ &= \frac{I_0 T_1 T_2}{1 + R_1 R_2 - 2 r_1 r_2 \cos\left(2\delta\right)}. \end{aligned} \tag{A.8}$$

Using $\cos 2x = 1 - 2\sin^2 x$ [75], the denominator of the expression can be rearranged to get

$$\begin{aligned} I_t &= \frac{I_0 T_1 T_2}{1 + R_1 R_2 - 2 r_1 r_2 \left(1 - 2\sin^2\left(\delta\right)\right)} \\ &= \frac{I_0 T_1 T_2}{1 + R_1 R_2 - 2 r_1 r_2 + 4 r_1 r_2 \sin^2\left(\delta\right)} \\ &= \frac{I_0 T_1 T_2}{\left(1 - r_1 r_2\right)^2 + 4 r_1 r_2 \sin^2\left(\delta\right)}. \end{aligned} \tag{A.9}$$

The maximum amplitude, $I_t^{\max}$, will be when the sine term is zero, $\delta = p\pi$, where p is an integer. In (A.10) the mirror transmissions have been expressed in terms of their corresponding amplitude reflectivity coefficients:

$$I_t^{\max} = \frac{I_0 \left(1 - r_1^2\right)\left(1 - r_2^2\right)}{\left(1 - r_1 r_2\right)^2}. \tag{A.10}$$

As there is a maximum every π in phase, this implies that there is a maximum in transmitted power every $\Delta\delta = \frac{2\pi\Delta\nu L}{c}$. Therefore (A.11) shows the frequency separation of each maxima in transmitted power

$$\Delta\nu = \frac{c}{2L}. \tag{A.11}$$

This is commonly called the Free Spectral Range, **FSR**, of the resonant cavity.

A.4 Half-Width at Half-Maximum

Define γ as the half-width frequency at half-maximum power; that is the frequency of the transmitted power at half-maximum relative to the resonant frequency. To determine this take the general expression for $I_t^{\max}$ from (A.10) and use it to evaluate $I_t^{\max}/2$,

$$\frac{I_t^{\max}}{2} = I_t(\gamma). \tag{A.12}$$

On resonance $\delta = p\pi$, therefore at half-maximum, $\delta = p\pi + \frac{2\pi\gamma L}{c}$. If it is assumed that γ is very small compared to the frequency spacing of resonances, $\Delta\nu$, then

$$\sin^2(\delta) \approx \delta^2 = \left(\frac{2\pi\gamma L}{c}\right)^2. \tag{A.13}$$

So (A.14) is obtained:

$$\frac{I_t^{\max}}{2} = \frac{I_0\left(1-r_1^2\right)\left(1-r_2^2\right)}{\left(1-r_1r_2\right)^2 + 4r_1r_2\left(\frac{2\pi\gamma L}{c}\right)^2}, \tag{A.14}$$

which can be simplified to

$$\frac{1}{2\left(1-r_1r_2\right)^2} = \frac{1}{\left(1-r_1r_2\right)^2 + 16r_1r_2\left(\frac{\pi\gamma L}{c}\right)^2}, \tag{A.15}$$

giving an expression for γ,

$$\gamma = \frac{c}{4\pi L}\frac{1-r_1r_2}{\sqrt{r_1r_2}}. \tag{A.16}$$

A.5 Finesse

Define a quantity that relates free spectral range to full-width at half-maximum. This quantity is called Finesse, $\mathcal{F}$. This is the ratio of mode spacing frequency to the full-width of the resonance

at half-maximum power,

$$\mathcal{F} = \frac{\frac{c}{2L}}{\frac{c\left(1-r_1r_2\right)}{2\pi L\sqrt{r_1r_2}}} = \frac{\pi\sqrt{r_1r_2}}{\left(1-r_1r_2\right)}. \tag{A.17}$$

A.6 Circulating Power

To get the power circulating in the cavity, divide I_t by T_2. This gives

$$I_c = \frac{I_0T_1}{\left(1-r_1r_2\right)^2 + 4r_1r_2\sin^2(\delta)}. \tag{A.18}$$

This also has a peak at $\delta = p\pi$ of $I_c^{\max}$,

$$I_c^{\max} = \frac{I_0T_1}{\left(1-r_1r_2\right)^2}. \tag{A.19}$$

As the transmission of the mirrors is $\ll 1$, it is possible to make the approximation,

$$r_{1,2} \approx 1 - \frac{T_{1,2}}{2}, \tag{A.20}$$

which allows the simplification of the term $\left(1-r_1r_2\right)^2$ to get

$$\left(1-r_1r_2\right)^2 = \left(1-\left(1-\frac{\left(T_1+T_2\right)}{2}+\frac{T_1T_2}{4}\right)\right)^2 \approx \frac{\left(T_1+T_2\right)^2}{4}. \tag{A.21}$$

This can be substituted back into the expression for $I_c^{\max}$ to get,

$$I_c^{\max} = \frac{4I_0T_1}{\left(T_1+T_2\right)^2}. \tag{A.22}$$

Then the enhancement of power on resonance is simply;

$$I^{\mathrm{e}} = \frac{4T_1}{\left(T_1 + T_2\right)^2}. \tag{A.23}$$

A.7 Cavity Equations for Identical Mirrors

If the two mirrors have the same reflectivity then $I_c^{\max}$ becomes;

$$\begin{aligned} I_c^{\max} &= \frac{4I_0T}{4T^2} \\ &= \frac{I_0}{T}. \end{aligned} \tag{A.24}$$

Then $\mathcal{F}$ becomes

$$\begin{aligned} \mathcal{F} &= \frac{\pi\sqrt{r^2}}{\left(1 - r^2\right)} \\ &= \frac{\pi r}{T} \end{aligned} \tag{A.25}$$

and $I_c^{\max}$ relates to $\mathcal{F}$ as,

$$I_c^{\max} = \frac{I_0\mathcal{F}}{\pi r} \approx \frac{I_0\mathcal{F}}{\pi}. \tag{A.26}$$

A.8 Reflection from Cavity

The total reflected field, a_r, is the sum of the field leaking through the mirror from the cavity and the directly reflected field. The directly reflected field is $-a_0r_1$. The field coupling back through M1 was obtained by dividing the transmitted field, a_t, by t_2, to get the field just inside M2. This field reflects off M2 and propagates towards M1. The amplitude of the field is therefore multiplied by factors of r_2 and $\exp(-i\delta)$. As the field travels through M1, it will be multiplied

by an extra factor t_1. The total reflected field, a_r is therefore

$$\begin{aligned} a_r &= -a_0 r_1 + a_t r_2 \exp(-i\delta)\, t_1 t_2 \\ &= -a_0 r_1 + \frac{a_0 r_2 t_1^2 \exp(-2i\delta)}{1 - r_2 r_1 \exp(-2i\delta)}. \end{aligned} \tag{A.27}$$

Thus when the cavity is on resonance, a_r is

$$\begin{aligned} a_r &= -a_0 r_1 + \frac{a_0 r_2 t_1^2}{1 - r_2 r_1} \\ &= \frac{-a_0 r_1 \left(1 - r_2 r_1\right) + a_0 r_2 t_1^2}{1 - r_2 r_1} \\ &= \frac{-a_0}{1 - r_2 r_1} \left(r_1 - r_2 r_1^2 - r_2 t_1^2\right). \end{aligned} \tag{A.28}$$

In the case that $r_1^2 + t_1^2 = 1$, the expression for a_r on resonance can be simplified to

$$a_r = \frac{-a_0 \left(r_1 - r_2\right)}{1 - r_2 r_1}. \tag{A.29}$$

A.9 Visibility

The visibility of a cavity is defined to be

$$\begin{aligned} V &= \frac{I_r^{\max} - I_r^{\min}}{I_r^{\max}} \\ &= 1 - \frac{I_r^{\min}}{I_r^{\max}}, \end{aligned} \tag{A.30}$$

and an image of reflected power varying with frequency is shown in Figure A.2. If M1 has a high reflectivity then when the cavity is not on the resonance point, $I_r = I_r^{\max} = a_0^2$. The reflected power on resonance is $I_r^{\min}$,

$$I_r^{\min} = \frac{a_0^2 \left(r_1 - r_2\right)^2}{\left(1 - r_2 r_1\right)^2}. \tag{A.31}$$

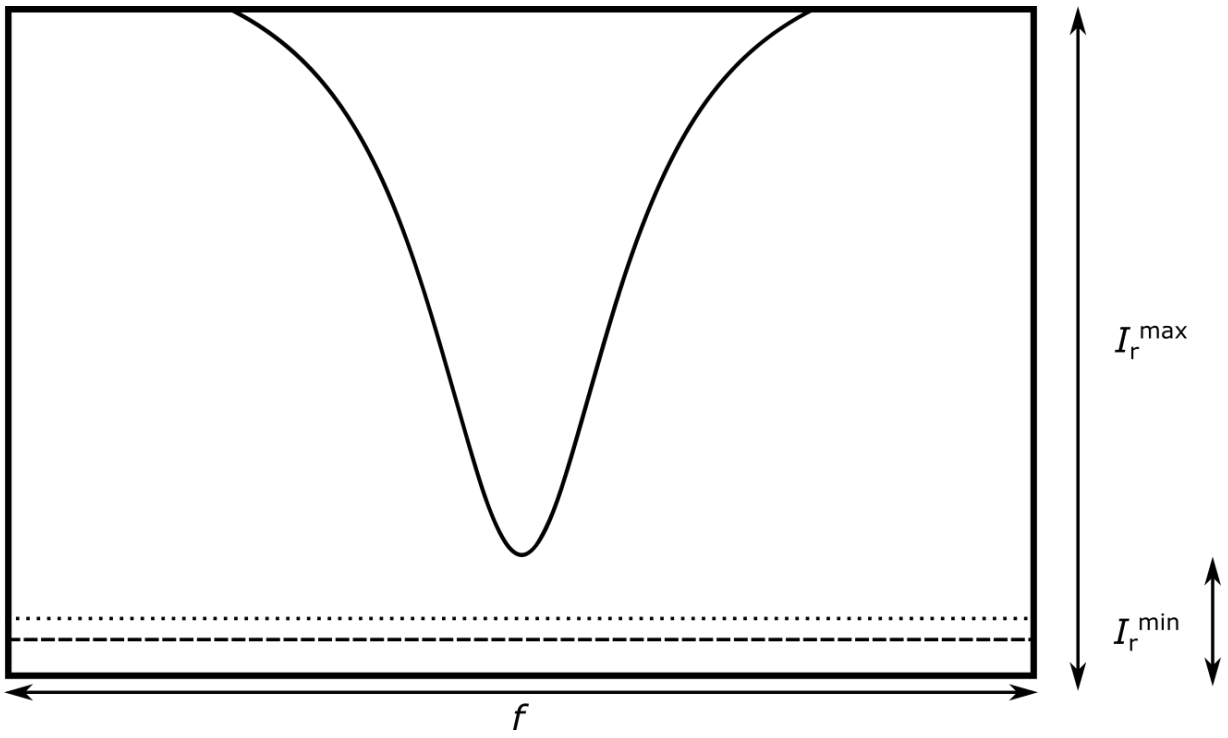

Figure A.2: Reflected power from a Fabry-Perot cavity while changing the frequency f of the laser around resonance, that is the point at which the light intensity reaches a minimum, $I_r^{\min}$. Away from resonance the reflected light is $I_r^{\max}$.

Again for highly reflective mirrors; $r_1 \approx 1 - \frac{T_1}{2}$ and $r_2 \approx 1 - \frac{T_2}{2}$. Substituting these into Equation (A.32), one obtains:

$$\begin{aligned} I_r^{\min} &= \frac{a_0^2 \left(\frac{T_2 - T_1}{2}\right)^2}{\left(1 - \left(1 + \frac{T_1 T_2}{4} - \frac{(T_1 + T_2)}{2}\right)\right)^2} \\ &= \frac{a_0^2 \left(T_2 - T_1\right)^2}{\left(T_1 + T_2\right)^2}. \end{aligned} \tag{A.32}$$

Therefore the visibility has the form

$$\begin{aligned} V &= 1 - \frac{\left(T_2 - T_1\right)^2}{\left(T_1 + T_2\right)^2} \\ V &= \frac{4 T_1 T_2}{\left(T_1 + T_2\right)^2}. \end{aligned} \tag{A.33}$$

A.10 Phase Modulation of the Input Field

As discussed later in the appendix, for resonant cavities it is common to modulate the phase of the input field in order to stabilise the frequency of the input field. This means that the effect of this modulation on the cavity visibility must be considered. Let β be the phase modulation depth applied to the ingoing field before the cavity and Ω be the modulation frequency, then the input field, a_{in}, to the cavity becomes,

$$a_{\text{in}} = a_0 \exp\left(i\omega t + i\beta \sin\left(\Omega t\right)\right). \tag{A.34}$$

Expanding using Bessel functions it is possible to make the approximation (A.35) [33]. This ignores terms with Bessel function coefficients of higher orders, $J_{2,3,\ldots,\infty}$ as these will not be needed in the analysis that follows.

$$\begin{aligned} a_{\text{in}} &\approx a_0 \left[\underbrace{J_0\left(\beta\right)}_{\text{carrier}} + \underbrace{2iJ_1\left(\beta\right)\sin\left(\Omega t\right)}_{\text{sidebands}} \right] \exp\left(i\omega t\right) \\ &= a_0 \left[\underbrace{J_0\left(\beta\right)\exp\left(i\omega t\right)}_{\text{carrier}} + \underbrace{J_1\left(\beta\right)\exp\left(i\left(\omega+\Omega\right)t\right)}_{\text{upper sideband}} - \underbrace{J_1\left(\beta\right)\exp\left(i\left(\omega-\Omega\right)t\right)}_{\text{lower sideband}} \right] \end{aligned} \tag{A.35}$$

For a cavity with high Finesse the sidebands are completely reflected by the cavity when the carrier is on resonance, and so the reflected field has the form a_r^{mod},

$$a_r^{\text{mod}} = \left(\left[J_0\left(\beta\right) + 2iJ_1\left(\beta\right)\sin\left(\Omega t\right) + \text{higher order terms}\right]\exp\left(i\omega t\right)\right)\left(a_r\right). \tag{A.36}$$

Introducing

$$d = \left[J_0\left(\beta\right)\right]\frac{-a_0\left(r_1 - r_2\right)}{1 - r_2 r_1}, \tag{A.37}$$

and

$$q = 2J_1\left(\beta\right)a_0, \tag{A.38}$$

assuming the magnitude of a_r for the sidebands is a_0 as these are far away in frequency from the cavity resonance. This simplifies a_r^{mod} to be:

$$a_r^{\mathrm{mod}} = (d + iq\sin(\Omega t))\exp(i\omega t)\,. \tag{A.39}$$

The expression for I_r^{min} is therefore

$$\begin{aligned} I_{\mathrm{min}} &= d^2 + q^2\sin^2(\Omega t) \\ &= d^2 + q^2\frac{1-\cos(2\Omega t)}{2}. \end{aligned} \tag{A.40}$$

The photodiode DC readout sees the average I_{min}, and so the term at 2Ω disappears and the measured power becomes,

$$\begin{aligned} I_{\mathrm{min}} &= d^2 + \frac{q^2}{2} \\ &= J_0^2(\beta)\frac{a_0^2\left(r_1 - r_2\right)^2}{\left(1 - r_2 r_1\right)^2} + 2J_1^2(\beta)\,a_0^2 \\ &= J_0^2(\beta)\frac{a_0^2\left(T_2 - T_1\right)^2}{\left(T_1 + T_2\right)^2} + 2J_1^2(\beta)\,a_0^2. \end{aligned} \tag{A.41}$$

The sidebands will not contribute to the maximum reflected power as this is measured at the carrier frequency. Thus I_{max} is a_0^2, and the observed visibility is

$$\begin{aligned} V &= 1 - \frac{I_{\mathrm{min}}}{I_{\mathrm{max}}} \\ &= \left[1 - J_0^2(\beta)\frac{\left(T_2 - T_1\right)^2}{\left(T_1 + T_2\right)^2} - 2J_1^2(\beta)\right]. \end{aligned} \tag{A.42}$$

If the modulation is small enough that $J_{2,\ldots,\infty}(\beta) \approx 0$, then the expression for V can be simplified to

$$V = J_0^2(\beta) - J_0^2(\beta)\frac{\left(T_2 - T_1\right)^2}{\left(T_1 + T_2\right)^2}, \tag{A.43}$$

since $J_0^2(\beta) + 2J_1^2(\beta) \approx 1$ as shown in [34]. This simplifies to

$$V = J_0^2(\beta)\frac{4T_2T_1}{\left(T_1+T_2\right)^2}. \tag{A.44}$$

This equation does not change if any of the higher order terms are included in the analysis, as the sum of the square of all the Bessel coefficients equals one for any β value.

A.11 Determine T_1 and T_2 from Cavity Measurements

If $\mathcal{F}$ and V have been measured, they can be used to determine T_1 and T_2. Substitute $r_1 \approx 1 - \frac{T_1}{2}$ and $r_2 \approx 1 - \frac{T_2}{2}$ into (A.17) to get

$$\mathcal{F} \approx \frac{\pi\sqrt{1-\frac{T_1}{2}-\frac{T_2}{2}}}{\frac{T_1}{2}+\frac{T_2}{2}}. \tag{A.45}$$

Then since $1 \gg T_{1,2}$, it is possible to simplify the $\mathcal{F}$ to

$$\mathcal{F} \approx \frac{2\pi}{T_1+T_2}. \tag{A.46}$$

Make V only dependent on one unknown by substituting $T_2 = xT_1$,

$$V = \frac{4T_1^2xJ_0^2(\beta)}{(1+x)^2T_1^2}. \tag{A.47}$$

If this equation is rearranged in x, then (A.48) is obtained

$$x^2 + x\left(2 - \frac{4J_0^2(\beta)}{V}\right) + 1 = 0. \tag{A.48}$$

Using the quadratic formula, x can be determined.

$$x = \frac{-2+\frac{4J_0^2(\beta)}{V} \pm \sqrt{4+\frac{16J_0^4(\beta)}{V^2}-\frac{16J_0^2(\beta)}{V}-4}}{2}. \tag{A.49}$$

The solution for x is

$$x = -1 + \frac{2J_0^2(\beta)}{V} \pm \left(\frac{2J_0(\beta)}{V} \sqrt{J_0^2(\beta) - V} \right). \tag{A.50}$$

Then this value is put into the expression for $\mathcal{F}$ and

$$\begin{aligned} \mathcal{F} &= \frac{2\pi}{T_1(1+x)} \\ &= \frac{\pi V}{T_1 J_0(\beta) \left(J_0(\beta) \pm \sqrt{J_0^2(\beta) - V} \right)} \end{aligned} \tag{A.51}$$

is obtained. Then rearrange to find T_1,

$$T_1 = \frac{\pi V}{\mathcal{F} J_0(\beta) \left(J_0(\beta) \pm \sqrt{J_0^2(\beta) - V} \right)}. \tag{A.52}$$

Then,

$$\begin{aligned} T_2 = &\frac{\pi V}{\mathcal{F} J_0(\beta) \left(J_0(\beta) \pm \sqrt{J_0^2(\beta) - V} \right)} \\ &\times \left[-1 + \frac{2J_0^2(\beta)}{V} \pm \left(\frac{2J_0(\beta)}{V} \sqrt{J_0^2(\beta) - V} \right) \right]. \end{aligned} \tag{A.53}$$

A.12 Correction for widening

This is the equation used to correct the measurement shown in Figure 5.11,

$$\frac{|A_t| + \eta}{A_m} \frac{C_{out}}{C_{in}} \tag{A.54}$$

for the 'widening' locking technique discussed in Section 3.3.5, which was only used for this measurement out of those transfer functions presented in Chapter 5. Here, A_t is the transmitted power photodiode readout, which should be proportional to the transmitted power from the cavity, η is the offset used in the widening process, typically on the order of 1 count, which is used to

ensure that the normalised error signal contains no zeros, A_{m} is the maximum transmitted power, used to normalise the widening denominator between 1 and 0 and $\frac{C_{\mathrm{out}}}{C_{\mathrm{in}}}$ is the widened error signal.

Bibliography

[1] Antonio Perreca, James Lough, David Kelley, and Stefan W. Ballmer. Multidimensional optical trapping of a mirror. *Phys. Rev. D*, 89:122002, Jun 2014.

[2] Markus Aspelmeyer, Tobias J. Kippenberg, and Florian Marquardt. Cavity optomechanics. *Rev. Mod. Phys.*, 86:1391–1452, Dec 2014.

[3] N. A. Gordon. *Characterisation and control of coupled optical springs for future gravitational wave detectors.* PhD thesis, University of Glasgow, 2015.

[4] N. V. Voronchev, S. L. Danilishin, and F. Ya. Khalili. Negative optical inertia in optomechanical systems. *Optics and Spectroscopy*, 112(3):377–385, 2012.

[5] Farid Khalili, Stefan Danilishin, Helge Müller-Ebhardt, Haixing Miao, Yanbei Chen, and Chunnong Zhao. Negative optical inertia for enhancing the sensitivity of future gravitational-wave detectors. *Phys. Rev. D*, 83:062003, Mar 2011.

[6] Henning Rehbein, Helge Müller-Ebhardt, Kentaro Somiya, Stefan L. Danilishin, Roman Schnabel, Karsten Danzmann, and Yanbei Chen. Double optical spring enhancement for gravitational-wave detectors. *Phys. Rev. D*, 78:062003, Sep 2008.

[7] Yanbei Chen. Macroscopic quantum mechanics: theory and experimental concepts of optomechanics. *Journal of Physics B: Atomic, Molecular and Optical Physics*, 46(10):104001, may 2013.

[8] B. P. Abbott et al. Observation of Gravitational Waves from a Binary Black Hole Merger. *Phys. Rev. Lett.*, 116:061102, Feb 2016.

[9] The LIGO Scientific Collaboration, J Aasi, et al. Advanced LIGO. *Classical and Quantum Gravity*, 32(7):074001, 2015.

[10] B. P. Abbott, R. Abbott, T. D. Abbott, S. Abraham, F. Acernese, K. Ackley, C. Adams, et al. GWTC-1: A Gravitational-Wave Transient Catalog of Compact Binary Mergers Observed by LIGO and Virgo during the First and Second Observing Runs. *Phys. Rev. X*, 9:031040, Sep 2019.

[11] The LIGO Scientific Collaboration, the Virgo Collaboration, R. Abbott, T. D. Abbott, F. Acernese, K. Ackley, C. Adams, N. Adhikari, R. X. Adhikari, et al. GWTC-2.1: Deep Extended Catalog of Compact Binary Coalescences Observed by LIGO and Virgo During the First Half of the Third Observing Run. *arXiv e-prints*, August 2021.

[12] The LIGO Scientific Collaboration, the Virgo Collaboration, the KAGRA Collaboration, R. Abbott, T. D. Abbott, F. Acernese, K. Ackley, C. Adams, N. Adhikari, R. X. Adhikari, et al. GWTC-3: Compact Binary Coalescences Observed by LIGO and Virgo During the Second Part of the Third Observing Run. *arXiv e-prints*, November 2021.

[13] B. P. Abbott, R. Abbott, T. D. Abbott, F. Acernese, K. Ackley, C. Adams, T. Adams, et al. GW170817: Observation of Gravitational Waves from a Binary Neutron Star Inspiral. *Phys. Rev. Lett.*, 119:161101, Oct 2017.

[14] A. Einstein. Näherungsweise Integration der Feldgleichungen der Gravitation. *Sitzungsber. K. Preuss. Akad. Wiss.*, 1:688, 1916.

[15] A. Einstein. Über Gravitationswellen. *Sitzungsber. K. Preuss. Akad. Wiss.*, 1:154, 1918.

[16] B. S. Sathyaprakash and Bernard F. Schutz. Physics, Astrophysics and Cosmology with Gravitational Waves. *Living Reviews in Relativity*, 12(1):2, Mar 2009.

[17] Luc Blanchet. Gravitational Radiation from Post-Newtonian Sources and Inspiralling Compact Binaries. *Living Reviews in Relativity*, 9(1):4, Jun 2006.

[18] L.D. Landau and E.M. Lifshitz. Chapter 5 - constant electromagnetic fields. In L.D. Landau and E.M. Lifshitz, editors, *The Classical Theory of Fields (Fourth Edition)*, volume 2 of

Course of Theoretical Physics, pages 89–108. Pergamon, Amsterdam, fourth edition edition, 1975.

[19] L.D. Landau and E.M. Lifshitz. Chapter 13 - gravitational waves. In L.D. Landau and E.M. Lifshitz, editors, *The Classical Theory of Fields (Fourth Edition)*, volume 2 of *Course of Theoretical Physics*, pages 345–357. Pergamon, Amsterdam, fourth edition edition, 1975.

[20] L.D. Landau and E.M. Lifshitz. Chapter 12 - the field of gravitating bodies. In L.D. Landau and E.M. Lifshitz, editors, *The Classical Theory of Fields (Fourth Edition)*, volume 2 of *Course of Theoretical Physics*, pages 295–344. Pergamon, Amsterdam, fourth edition edition, 1975.

[21] Matthew Pitkin, Stuart Reid, Sheila Rowan, and Jim Hough. Gravitational Wave Detection by Interferometry (Ground and Space). *Living Reviews in Relativity*, 14(1):5, Jul 2011.

[22] B. P. Abbott et al. GW150914: The Advanced LIGO Detectors in the Era of First Discoveries. *Phys. Rev. Lett.*, 116:131103, Mar 2016.

[23] A. A. Michelson and E. W. Morley. On the relative motion of the Earth and the luminiferous ether. *American Journal of Science*, 34:333–345, Nov 1887.

[24] Tobin T Fricke, Nicolás D Smith-Lefebvre, Richard Abbott, Rana Adhikari, Katherine L Dooley, Matthew Evans, Peter Fritschel, Valery V Frolov, Keita Kawabe, Jeffrey S Kissel, Bram J J Slagmolen, and Sam J Waldman. DC readout experiment in Enhanced LIGO. *Classical and Quantum Gravity*, 29(6):065005, feb 2012.

[25] Sheila Dwyer, Daniel Sigg, Stefan W. Ballmer, Lisa Barsotti, Nergis Mavalvala, and Matthew Evans. Gravitational wave detector with cosmological reach. *Phys. Rev. D*, 91:082001, Apr 2015.

[26] Charlotte Bond, Daniel Brown, Andreas Freise, and Kenneth A. Strain. Interferometer techniques for gravitational-wave detection. *Living Reviews in Relativity*, 19(1):3, Feb 2017.

[27] Carlton M. Caves. Quantum-Mechanical Radiation-Pressure Fluctuations in an Interferometer. *Phys. Rev. Lett.*, 45:75–79, Jul 1980.

[28] F Matichard, B Lantz, R Mittleman, K Mason, J Kissel, B Abbott, S Biscans, J McIver, R Abbott, S Abbott, E Allwine, S Barnum, J Birch, C Celerier, D Clark, D Coyne, D DeBra, R DeRosa, M Evans, S Foley, P Fritschel, J A Giaime, C Gray, G Grabeel, J Hanson, C Hardham, M Hillard, W Hua, C Kucharczyk, M Landry, A Le Roux, V Lhuillier, D Macleod, M Macinnis, R Mitchell, B O'Reilly, D Ottaway, H Paris, A Pele, M Puma, H Radkins, C Ramet, M Robinson, L Ruet, P Sarin, D Shoemaker, A Stein, J Thomas, M Vargas, K Venkateswara, J Warner, and S Wen. Seismic isolation of Advanced LIGO: Review of strategy, instrumentation and performance. *Classical and Quantum Gravity*, 32(18):185003, aug 2015.

[29] G. Harry, T. Bodiya, and R. DeSalvo, editors. *Optical Coatings and Thermal Noise in Precision Measurement*. Cambridge University Press, 2012.

[30] A. Buikema, C. Cahillane, G. L. Mansell, C. D. Blair, R. Abbott, C. Adams, R. X. Adhikari, et al. Sensitivity and performance of the Advanced LIGO detectors in the third observing run. *Phys. Rev. D*, 102:062003, Sep 2020.

[31] Stefan L. Danilishin and Farid Ya. Khalili. Quantum Measurement Theory in Gravitational-Wave Detectors. *Living Reviews in Relativity*, 15(1):5, Apr 2012.

[32] R. W. P. Drever, J. L. Hall, F. V. Kowalski, J. Hough, G. M. Ford, A. J. Munley, and H. Ward. Laser phase and frequency stabilization using an optical resonator. *Applied Physics B*, 31(2):97–105, Jun 1983.

[33] Eric D. Black. An introduction to Pound–Drever–Hall laser frequency stabilization. *American Journal of Physics*, 69(1):79–87, 2001.

[34] Eric Black. Notes on the Pound-Drever-Hall technique. Technical Document T980045-00-D, LIGO, 1998.

[35] M. Tse, Haocun Yu, N. Kijbunchoo, A. Fernandez-Galiana, P. Dupej, L. Barsotti, C. D. Blair, et al. Quantum-Enhanced Advanced LIGO Detectors in the Era of Gravitational-Wave Astronomy. *Phys. Rev. Lett.*, 123:231107, Dec 2019.

[36] John Miller, Lisa Barsotti, Salvatore Vitale, Peter Fritschel, Matthew Evans, and Daniel Sigg. Prospects for doubling the range of Advanced LIGO. *Phys. Rev. D*, 91:062005, Mar 2015.

[37] S Di Pace. Status of Advanced Virgo and upgrades before next observing runs. *Physica Scripta*, 96(12):124054, nov 2021.

[38] ET steering committee et al. Einstein Telescope: Science Case, Design Study and Feasibility Report. Online: https://apps.et-gw.eu/tds/ql/?c=15662, 2020. Accessed: 09.03.2022.

[39] ET steering committee. ET design report update 2020. Online: https://apps.et-gw.eu/tds/ql/?c=15418, 2020. Accessed: 09.03.2022.

[40] David Reitze, Rana X Adhikari, Stefan Ballmer, Barry Barish, Lisa Barsotti, GariLynn Billingsley, Duncan A. Brown, Yanbei Chen, Dennis Coyne, Robert Eisenstein, Matthew Evans, Peter Fritschel, Evan D. Hall, Albert Lazzarini, Geoffrey Lovelace, Jocelyn Read, B. S. Sathyaprakash, David Shoemaker, Joshua Smith, Calum Torrie, Salvatore Vitale, Rainer Weiss, Christopher Wipf, and Michael Zucker. Cosmic Explorer: The U.S. Contribution to Gravitational-Wave Astronomy beyond LIGO. *Bulletin of the AAS*, 51(7), 9 2019. https://baas.aas.org/pub/2020n7i035.

[41] V.B. Braginsky, M.L. Gorodetsky, and F.Ya. Khalili. Optical bars in gravitational wave antennas. *Physics Letters A*, 232(5):340–348, 1997.

[42] H. Rehbein, H. Müller-Ebhardt, K. Somiya, S. L. Danilishin, R. Schnabel, K. Danzmann, and Y. Chen. Double optical spring enhancement for gravitational-wave detectors. *Phys. Rev. D*, 78(6):062003, September 2008.

[43] Stefan L. Danilishin, Farid Ya. Khalili, and Haixing Miao. Advanced quantum techniques for future gravitational-wave detectors. *Living Reviews in Relativity*, 22(1):2, April 2019.

[44] Moritz Mehmet and Henning Vahlbruch. The Squeezed Light Source for the Advanced Virgo Detector in the Observation Run O3. *Galaxies*, 8(4), 2020.

[45] Craig Cahillane and Georgia Mansell. Review of the Advanced LIGO Gravitational Wave Observatories Leading to Observing Run Four. *Galaxies*, 10(1), 2022.

[46] Sheon S. Y. Chua. *Quantum enhancement of a 4 km laser interferometer gravitational-wave detector*. Springer International Publishing Switzerlaand, Switzerland, 1st edition, 2015. Doctoral Thesis accepted by The Australian National University, Canberra, Australia.

[47] H. Goldstein, C. P. Poole, and J. Sakko. *Classical Mechanics*. Pearson under license to Dorley-Kindersley, Noida, U.F., India, 3rd edition, 2011.

[48] M. M. Sternheim and J. W. Kane. *General Physics*. Wiley, New York, NY, USA, 2nd edition, 1991.

[49] Lev Kantorovich. *Mathematics for Natural Scientists Fundamentals and Basics*. Springer, New York, NY, USA, 2016. Available at https://doi-org.ezproxy.lib.gla.ac.uk/10.1007/978-1-4939-2785-2.

[50] J. D. Jackson. *Classical Electrodynamics*. Wiley, Hoboken, NJ, USA, 1998.

[51] B. Goodwine. *Engineering Differential Equations Theory and Applications*. Springer, New York, NY, USA, 2011. Available at https://doi-org.ezproxy.lib.gla.ac.uk/10.1007/978-1-4419-7919-3.

[52] Thomas Corbitt, Christopher Wipf, Timothy Bodiya, David Ottaway, Daniel Sigg, Nicolas Smith, Stanley Whitcomb, and Nergis Mavalvala. Optical Dilution and Feedback Cooling of a Gram-Scale Oscillator to 6.9 mK. *Phys. Rev. Lett.*, 99:160801, Oct 2007.

[53] Brian J. Meers. Recycling in laser-interferometric gravitational-wave detectors. *Phys. Rev. D*, 38:2317–2326, Oct 1988.

[54] J. Macarthur. *Towards surpassing the standard quantum limit using optical springs*. PhD thesis, University of Glasgow, 2014.

[55] N A Gordon, B W Barr, A Bell, C Graef, S Hild, S H Huttner, S S Leavey, J Macarthur, B Sorazu, J Wright, and K A Strain. Experimental demonstration of coupled optical springs. *Classical and Quantum Gravity*, 34(3):035020, jan 2017.

[56] T. Corbitt, Y. Chen, E. Innerhofer, H. Müller-Ebhardt, D. Ottaway, H. Rehbein, D. Sigg, S. Whitcomb, C. Wipf, and N. Mavalvala. An All-Optical Trap for a Gram-Scale Mirror. *Physical Review Letters*, 98(15):150802, April 2007.

[57] David Kelley, James Lough, Fabian Mangaña Sandoval, Antonio Perreca, and Stefan W. Ballmer. Observation of photothermal feedback in a stable dual-carrier optical spring. *Phys. Rev. D*, 92:062003, Sep 2015.

[58] F. Träger. *Springer Handbook of Lasers and Optics*. Springer Handbook. Springer, New York, NY, 1 edition, 2007. online: https://link-springer-com.ezproxy.lib.gla.ac.uk/referencework/10.1007

[59] R. Paschotta. article on Faraday isolators in the RP Photonics Encyclopedia. https://www.rp-photonics.com/faraday_isolators.html. accessed on 2022-03-23.

[60] R. Paschotta. article on Faraday rotators in the RP Photonics Encyclopedia. https://www.rp-photonics.com/faraday_rotators.html. accessed on 2022-03-23.

[61] R. Paschotta. article on 'electro-optic modulators' in the RP Photonics Encyclopedia. https://www.rp-photonics.com/electro_optic_modulators.html. accessed on 2022-03-28.

[62] J. R. Taylor. *Interferometric Experiments Towards Advanced Gravitational Wave Detectors*. PhD thesis, University of Glasgow, 2008.

[63] S Goßler, A Bertolini, M Born, Y Chen, K Dahl, D Gering, C Gräf, G Heinzel, S Hild, F Kawazoe, O Kranz, G Kühn, H Lück, K Mossavi, R Schnabel, K Somiya, K A Strain, J R Taylor, A Wanner, T Westphal, B Willke, and K Danzmann. The AEI 10 m prototype interferometer. *Classical and Quantum Gravity*, 27(8):084023, apr 2010.

[64] Marco Arrigoni, Oliver Haupt, and Volker Leonhardt. Ultra Low-Noise and Narrow Linewidth. Online: https://edge.coherent.com/lasers/laser/mephisto-mephisto-s. Accessed: 06.01.2018.

[65] Datasheet Mephisto/Mephisto S. Online: https://edge.coherent.com/lasers/laser/mephisto-mephisto-s. Accessed: 13.07.2020.

[66] J. Stevens. medm Tutorial. Online at https://epics.anl.gov/docs/APS2014/03-MEDM-Tutorial.pdf, 2014. Accessed: 06.08.2020.

[67] J. Heefner. BSC Suspension Test Stand Electronics and Controls Quick Start Guide. Technical Report LIGO-T080321-00-C, LIGO, 2008.

[68] Li Tan and Jean Jiang. Chapter 2 - Signal Sampling and Quantization. In Li Tan and Jean Jiang, editors, *Digital Signal Processing (Second Edition)*, pages 15–56. Academic Press, Boston, second edition edition, 2013.

[69] W. T. Eadie, D. Dryard, F. E. James, M. Roos, and B. Sadoulet. *STATISTICAL METHODS IN EXPERIMENTAL PHYSICS*. North-Holland Publishing Company Ltd, London, 1st edition, 1971.

[70] N. Gordon and B. Barr. Ringdown_01_b & fitcurvedemo_b. internal file, 2013. MATLAB code.

[71] M. Evans. Optickle2. Copyright (C) 2014 Matthew Evans.

[72] M. Evans. Optickle2. online repository, July 2015. Available online: https://github.com/Optickle/Optickle/tree/Optickle2.

[73] N. Gordon. dual_carrier_optickle_model. personal communication, 2014. Code files received from author: 2015.

[74] Eric W. Weisstein. Negative Binomial Series. From MathWorld–A Wolfram Web Resource. http://mathworld.wolfram.com/NegativeBinomialSeries.html. Accessed: 17.02.2020.

[75] Eric W. Weisstein. Trigonometric Addition Formulas. From MathWorld–A Wolfram Web Resource. http://mathworld.wolfram.com/TrigonometricAdditionFormulas.html. Accessed: 25.02.2020.